Constructing Mean Electron Distributions from Hard X-Ray Spectra of Solar Flares

Eamon Scullion B.Sc.

Thesis
submitted to the
University of Glasgow
for the degree of
MSc

UNIVERSITY
of
GLASGOW

Astronomy & Astrophysics Group
Department of Physics & Astronomy
University of Glasgow
Scotland
December 2006

Abstract

The *Ramaty High Energy Solar Spectroscopic Imager* (RHESSI) mission provides information on high resolution X-ray spectra emitted by collisional bremsstrahlung of thermal and non-thermal electrons with ions in solar flares. One of the aims of the mission is to infer information about the acceleration and transport mechanisms of hard X-ray emitting electrons and γ-ray emitting ions in solar flares. I investigate events observed during distinct attenuator states of the satellite, which have unique characteristics in their photon and mean electron distributions. Such characteristics include evidence of low energy cutoff features and other such physically real bump and dip features. In the framework of a collisionally thin bremsstrahlung model and an adjustable thermal function I forward fit these to the background-removed count flux data, using least squares minimization via OSPEX (*Object Spectroscopy Executive*). Along with Chi-Square Tests, I present random and non-systematic residuals to show goodness of fit.

Conversion from count rate to count flux and then to photon flux spectra is a traditional approach to modelling hard X-ray spectra, but is significantly unreliable due to its dependence on parametric electron distribution approximations. Model independent hard X-ray spectra can be non-trivially calculated using the *Detector Response Matrix* (DRM) and are computed using a sequence of algorithms solving a linear system of equations, which present an inversion problem characterized by numerical instability due to the non-diagonal nature of the DRM. The extent of such instability is unique for different DRM configurations, hence different under each attenuator state. We then address the solution of this inversion problem by using a regularization algorithm with the aim of inferring accurate and useful electron distribution spectra. Adjustment of this procedure to convert directly between counts and electrons, which is a one step rather than two step process, presents more robust and detailed information about features of electron dynamics during flares. Significant features such as low and high energy cutoffs tell us much about electron acceleration properties and energy losses in the flare evolution. Comparing regularized solutions in each event through different approaches will allow for confirmation of the existence or non-existence of such features. This innovative regularization technique is capable of portraying a truer interpretation of both hard X-ray and mean electron spectra.

Acknowledgements

Dante once said, "*Long and hard is the way...*", and he would have been perfectly right if he had been referring to the mental struggle that it takes to write a physics masters thesis. There are a number of people who I wish to pay special thanks for their sustained guidance, friendship and support through my one year masters degree at the University of Glasgow.

To begin with, a special thanks should be given to my first supervisor Prof. John C. Brown whose guidance and help throughout the writing up stage was unmeasurable. His ability to uncover the key issues in any problem made him a valuable asset to have. Furthermore, I want to extend my thanks to my second supervisor Dr. Eduard P. Kontar who guided and effectively tutored me through every stage of this research. His continued patience was unwavering, despite all of my simple questions, and more importantly his overall passion for research in this field was immediately obvious and provided me with ambition to learn more. His future students will be lucky to have him, not just as a supervisor, but for his unparalleled attributes as a mentor and a teacher. I want to acknowledge the continued patience and help given to me by my colleagues Robert McKay and Cris Sabiu who rescued me from the many pit falls which I encountered within LaTeX software and the Unix system. Their tolerance and dedication to their specific fields of interest was truly inspirational and subsequently provided me with much motivation.

In my time at Glasgow I had a great many opportunities and experiences and met many wonderful people from many different backgrounds and nationalities all over the world. However, I am sure it would not have been half as enjoyable had it not been for my good friend (and part-time colleague) Paul Holt. There are few people in the world that one can genuinely call a close friend. Many people meet and form friendships which can, more often than not, be a momentary thing. In that case, I cannot simply refer to Paul as just a friend, because no matter where we go and who we meet I know that Paul will forever be someone

I can really trust, depend on and respect. At numerous times in the course of this last year I wanted to give up and then Paul would come into my office and I would think ... it could be worse ... lol (only joking) ... cheers man.

Finally, I want to pay thanks to two people who have had, most certainly, the biggest influence upon this thesis and are the most important features in my life. Without them I would not have had the strength to complete this thesis or the determination to resolve the many problems encountered. Their continued and unconditional love, support (in all aspects) and guidance is phenomenal and there are simply not enough words to describe how much they mean to me, or how indebted I am to them. To anyone who is as lucky as I am to have them in their life will instantly know that the people I am referring to are my parents Daniel and Felicitas Scullion. To you both, and to my sisters Siobhan, Fiona and Danielle, I dedicate every last word here-in. All my love forever, thank you.

Declaration

The work in this thesis is based on research carried out at the Astronomy & Astrophysics Group within the Department of Physics & Astronomy of the University of Glasgow, Scotland. No part of this thesis has been submitted elsewhere for any other degree or qualification and it is all my own work unless referenced to the contrary in the text.

Contents

List of Figures

List of Tables

Chapter 1

Introduction

"Solar Flares are complex ..."

Sweet,1969

1.1 Solar Flares : Overview

A solar flare is an enormous explosion in the solar atmosphere and the most powerful of all manifestations of solar activity. This dramatic process involves sudden bursts of particle acceleration, plasma heating, and bulk mass motion. The solar atmosphere extends outward from the photosphere, through the chromosphere and then to its outer atmosphere, the corona. The first observation of a solar flare, extending across a sunspot on the solar disk in white light, was made by Richard C.Carrington on September 1 1859.

Flare energy can be as large as 10^{32} erg, which is approximately 100 times more energy than what could be obtained through burning all coal and oil reserves on Earth (Boris V.Somov, 1992).

Figure 1.1 simply illustrates the basic structures that are formed with respect to the radiation emission regions in flares. Flare structure includes the loop-top (above the flare loop arcade) and foot-point (on the solar surface) sources where hard X-ray sources are indicated. Particle acceleration is thought to originate in the loop-top and particle propagation is directed along magnetic field lines in magnetic flux tubes, which form the legs of the flare arcade. The loop-top sources lie within the solar corona and the foot-points of the flare are

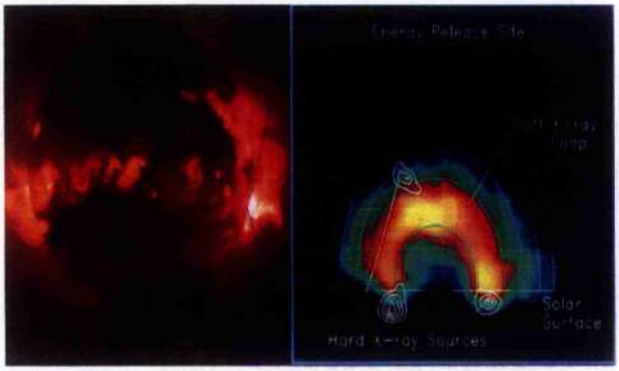

Figure 1.1: The image shows an X-ray photo from the Yohkoh satellite of a flare (*Left*) clearly seen on the right hand limb of the sun just below the equator. A simple cartoon highlighting the sources X-ray emission of the flare is also presented, *center*.

generally located in the solar chromosphere. The temperatures of these plasma sources are very different and hard X-ray emission due to the accelerated electrons in both regions is strongly dependent upon the relative plasma particle densities.

1.1.1 Flare Temperatures and Energy release

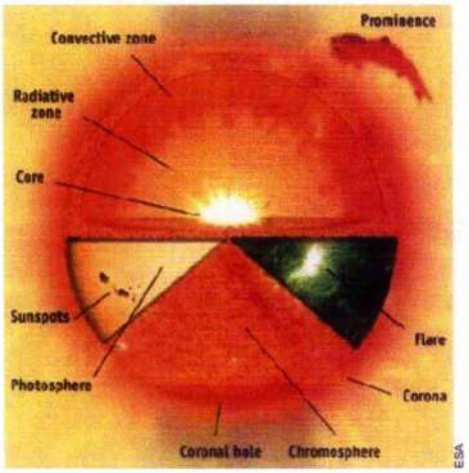

Figure 1.2: The illustration shows the different layers of the Sun which are observed.

Figure 1.2 shows the photosphere as the bright solar surface where energy leaves the Sun as visible light. Due to its temperature of ~5800 Kelvin, the photosphere shines with light of visible wavelengths and has a yellowish colour. Above the photosphere is the chromosphere. The upper chromosphere is hotter ($\approx 10^4 - 10^5$)K than the photosphere and the lower chro-

mosphere. The chromosphere is much more dense than the corona with an average particle density in the range $10^{12} - 10^{14}$ cm^{-3} compared with particle densities of $10^{9} - 10^{11}$ cm^{-3} in the corona. Due to its very high temperature, the corona emits mostly X-rays, visible only to high-energy spacecraft instruments. Flare foot-points are observed in the chromosphere, in chromospheric lines, with the Hα line of hydrogen being most common. Consequently, the name 'chromospheric flare' became widespread in early observations before the discovery of the flare X-ray component. Figure 1.3 shows a classic Hα image of the great sea horse flare.

Figure 1.3: This is an example of a two ribbon flare. The ribbons have separated and elongated. This image was taken on August 7^{th} 1972, with the Big Bear Solar Observatory.

Super hot temperatures of up to 40MK, are consistent with coronal source flares which support the emission of hard X-rays (Emslie et al. 2003), while temperatures in the range of 2×10^{7} Kelvin are associated with soft X-rays. By hard X-ray emission we mean high energy X-ray emission, as opposed to soft X-ray emission which refers to low energy X-ray emission. Hard X-rays (HXR) are associated with photons within the 10-100keV energy range, while soft X-rays (SXR) have energies ranging from 1-10keV. Consequently, hard X-rays are more likely to be associated with accelerated particles (non-thermal electrons) in flares due to their high kinetic energy. Similarly, soft X-rays are more likely to be associated with thermal electrons (low kinetic energy), of low mean free paths, emitting bremsstrahlung radiation.

Bremsstrahlung Emission :

Bremsstrahlung means *braking radiation*. Elastic deflection of a relatively light electron (compared with a massive proton, ion or atom) causes electron deceleration and some energy loss as bremsstrahlung photon emission at X-ray wavelengths.

Figure 1.4: Illustration of an electron interaction with a nucleus (proton), resulting in electron deceleration and X-ray photon emission.

The bremsstrahlung emission process illustrated in figure 1.4 has a characteristic interaction cross-section. This cross-section describes the effective area around a targeted proton, ion or atom where incident electrons give up some of their energy through bremsstrahlung radiation. This area is otherwise known as the bremsstrahlung cross-section (Koch and Motz, 1953) and will be considered further in chapter 2. By energy conservation, emitted photons cannot have more energy than the kinetic energy of the electron whose deceleration produced it.

1.1.2 Flare Structure and Evolution

The widely accepted view is that the processes by which flares occur are dependent upon the configuration of magnetic connections in the solar corona. The term *coronal flare* is used for flares occurring on coronal magnetic loop tops.

We can describe the energy release process and progression of accelerated particles from the loop-top to the foot-points of the magnetic flux tube in three stages:

(1) Preheating Phase -

The violent release of highly energetic particles follows a period of preheating in the coronal plasma in the flare region. This is visible in soft X-ray emission and EUV along with brightening in Hα for a period.

(2) Impulsive Phase -

The explosion of highly energetic electrons radiating hard X-ray photons, considered to originate in the loop-top sources, coincides with fast electron propagation and is a direct response to the trigger for a flare event. Carmichael-Sturrock-Hirayama-Kopp-Pneuman (CSHKP) reconnection models represent one standard flare scenario (Carmichael,1964; Sturroch,1966; Hirayama,1974; Kopp & Pneuman, 1976) which occurs when opposing closed magnetic field lines intersect (X-point) and change configuration (McKenzie, 2002). As a consequence, fast plasma flows, combined with local magnetic field restructuring, is observable in a sequence of short powerful hard X-ray bursts followed by intense brightening in Hα. A larger, magnetic loop, or plasmoid, moves upwards, while downward moving material forms an arcade of coronal loops.

All the while, in the loop-top source superheated gas expands promptly resulting in a gradual temperature decrease. Hard X-rays are radiated from the most energetic particles which have become accelerated to high energies. Collisional bremsstrahlung radiation results from long range interaction between relatively light electrons with heavy ions in the plasma, resulting in elastic deflection of the electrons as they propagate. Accelerated particles propagate from the loop-top and are injected into the denser ambient chromosphere. Though considering the energy loss time for electrons allows us to present two important non-thermal models: thick target (large energy loss) and thin target (small energy loss), as proposed by Brown, 1971. The dense chromosphere allows more efficient hard X-ray production due to Coulomb collisions between the particles (collisional bremsstrahlung emission),

which ultimately emit most of their energy as hard X-rays. The cold background in the chromosphere foot-points means electron-electron interactions result in kinetic energy exchange and plasma heating (Brown, 1971; Hudson, 1972; Lin & Hudson, 1976). Hirayama's cartoon model presented in figure 1.5 illustrates this process describing electron propagation through the magnetic flux tube towards the foot points from a cross-section and side view perespective (Hirayama, 1974).

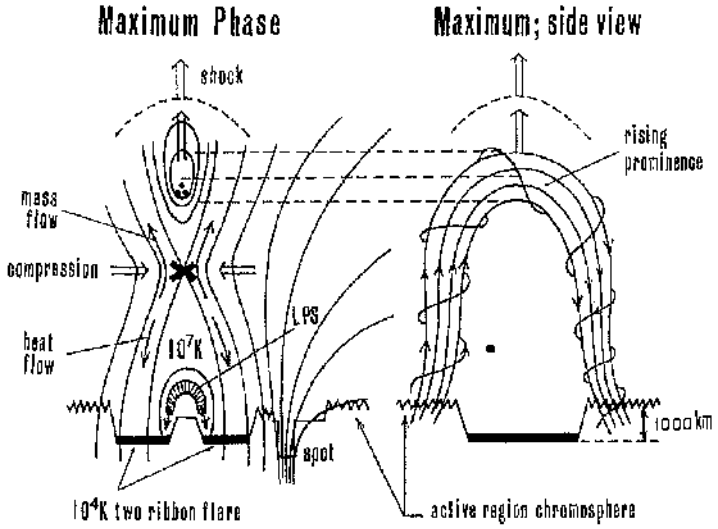

Figure 1.5: Illustration of Hirayama's interpretation of the flare progression in 1974. It is understood that where there is compression at the X-point, we get magnetic reconnection.

The magnitude of the total energy output, during the flare impulsive phase, is of the same order as the energy of the non-thermal electrons (Lin and Hudson, 1971; 1976; Brown, 1971; 1973).

(3) Gradual/Main Phase -

The cooler plasma, in the chromosphere, is heated and evaporates to fill the magnetic flux tube emitting thermal bremsstrahlung (Brown, 1973). This results in soft X-ray flare loops as is illustrated in figure 1.6 (Priest and Forbes, 2002).

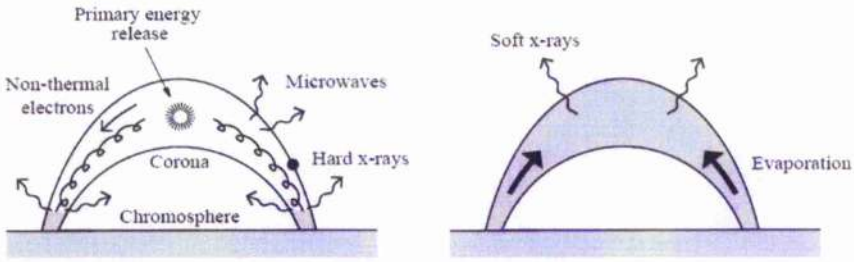

Figure 1.6: Production of Hard and Soft X-rays in flares

The Tripolar Flare Model illustrates reconnection between closed and open field lines in the corona and an emerging small scale soft X-ray loop (Shimojo & Shibata, 2000). The flare reaches its largest area with much of the remaining energy emitted as thermal soft X-rays. A standard and, widely accepted, flare model (fig. 1.7) incorporates magnetic reconnection along with plasmoid elevation through the corona forming a cusp shaped structure (Tsuneta et al., 1992). This is a significant development on the CSHKP models (Shibata et al., 1995).

Flare classification is largely dependent upon the intensity of the SXR (soft X-ray) photon flux radiated from the SXR sources.

1.1.3 Flare Classification

Hα ribbon emission had historically classified flares according to the area of the Hα brightening (Zirin, 1988). Then space observations revealed the soft X-ray component in the corona. Today, the GOES (Geostationary Operational Environmental Satellite) SXR classification is most popular. The GOES weather satellite determines the power of a flare according to its peak intensity in the 1-8 Å(*Ångstroms*) wavelength light-curve (1-7keV). For soft X-ray

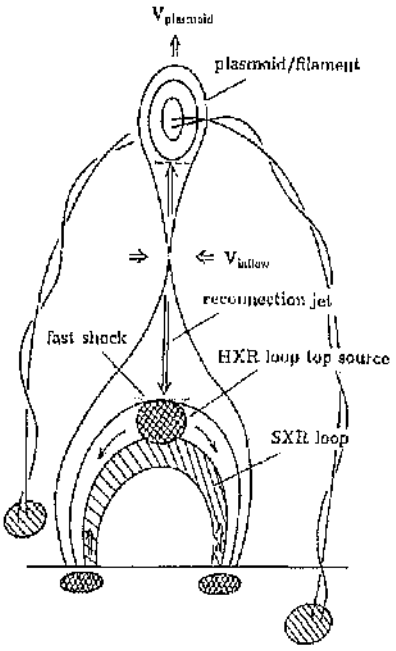

Figure 1.7: The standard flare model illustrates different flare phases outlined in 'Flare Structure and Evolution'.

flares the classification scheme uses 5 letters (A , B , C , M , X) followed by a number. The letters denote the order of magnitude of flux detected according to the power of 10 of the flux in units of Wm^{-2}.

GOES Class	Flux $[Wm^{-2}]$
A1	10^{-8}
B1	10^{-7}
C1	10^{-6}
M1	10^{-5}
X1	10^{-4}

Table 1.1: Definition of GOES Classification

It is also possible to distinguish between different classes of hard X-ray flares. Classification is not dependent upon flare area or intensity but rather more importance is given to duration and shape of the HXR light-curve (Tanaka, 1987), described in table 1.2.

HXR Class	Description
A *Hot Thermal*	Smoothly varying flux vs. time profile, with limited soft HXR emission and single loop.
B *Impulsive*	Spikey flux vs. time profile, associated with microwave emission and large loops
C *Gradual Hard*	Long enduring time profile (30min), gradual peaks, hard spectrum. Very large loops.

Table 1.2: HXR Classification Types

1.1.4 The Solar Flare problem : An Incomplete Solution

The study of solar flare phenomena, which I have briefly touched upon, focuses on answering two fundamental questions, How and where is the source of primary energy released in flares ?, and How do electrons propagate throughout the whole volume of the flare?. Understanding in detail the mean electron distribution spectra in flares will enable us to accurately answer these questions.

We have seen that, since the beginning of space based observations, significant hard X-rays were found to be radiating from the relatively cool chromosphere, explainable through non-thermal emission models (Brown, 1971). Masuda et al. (1995) presented and analyzed the first imaging observation of a hard X-ray coronal source in the limb of the Sun (1994), and at the loop-top of the magnetic flux tube of soft X-rays. The popularly named Masuda Flare is in a sense one of a kind, in that there are relatively few direct observations of loop-top hard X-ray emission in flares that are clearly distinct from the foot-point sources, and fewer as intense as the Masuda event. It seems likely that a thin target equivalent, due to the thin coronal atmosphere, of the collisional thick target model is involved in loop-top sources.

Understanding the mechanisms surrounding acceleration of electrons, as their transport from the reconnection site throughout the source volume of the flare, will be assisted through reconstructing accurate, flare electron spectra. This will also be imperative to our understanding of the flare energy transport mechanisms and, even more importantly, the origins of primary energy release in flares. Constructing flare electron spectra accurately depends

on the accuracy and resolution of the hard X-ray spectrum observed from space.

Space Observations :

The first balloon-borne observations of hard X-rays from solar flares sparked a great advance in both the spectral and temporal resolution of such violent events (Peterson and Winckler, 1959). Great progress has been made in exploring the sun-solar system through continual advances in ground and space based instrumentation, particularly with satellites such as Voyager, Skylab, Solar Maximum Mission (SMM), TRACE[1], SOHO[2], *Yohkoh* (Ogawara et al., 1991), and more recently the Reuven Ramaty High Energy Solar Spectroscopic Imager (RHESSI)[3] (Lin et al., 2002) mission. SMM in the 1980's and *Yohkoh* in the 1990's uncovered great detail in solar flare phenomena in the HXR energy range eg. the Masuda flare. However, some might say that the achievements of the RHESSI mission have excelled in all aspects of solar atmosphere observations.

1.1.5 RHESSI

The RHESSI spacecraft is the 6th NASA Small Explorer (SMEX) mission. RHESSI was launched on the 5^{th} February 2002 and recorded its first observations on 12^{th} February 2002.

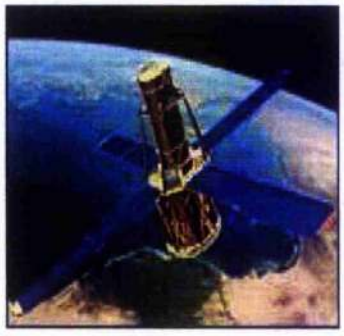

Figure 1.8: The RHESSI satellite in orbit (taken from RHESSI mission description, 2003).

The aim of the RHESSI mission is to study particle acceleration processes and explosive

[1] *http : //vestige.Imsal.com/TRACE/*
[2] *http : //sohoww.nascom.nasa.gov/*
[3] *http : //hesperia.gsfc.nasa.gov/hessi/*

energy release in flares using high resolution X-ray and γ-ray imaging and spectroscopy.

RHESSI Spectrometer :

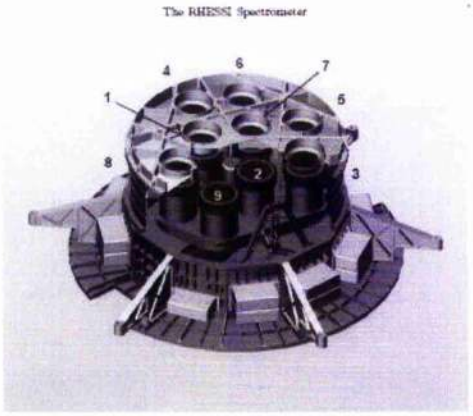

Figure 1.9: The RHESSI spectrometer with part of the housing cut away to reveal detector modules inside. The numbering scheme of the detectors matches the grids (D.M.Smith et al.,Sept., 2002).

The energy resolution of the detectors, made of hyper-pure germanium, is $\approx$1keV FWHM (Full-Width-Half-Maximum) in the front segments, and $\approx$3keV in the rear segments. A specific arrangement of the electrodes for each detector is divided into front and rear segments. As a result the front segment is most sensitive to incoming X-ray radiation detectable in the energy range 3-300keV, whereas the more highly energetic and penetrating γ-rays (up to $\sim$ 17MeV) (Dennis et al.2004) are mostly stopped in the rear segment and registered there (Smith, 2002). Each detector is associated with one of 9 grids, and allows for the construction of detailed images, as shown in figure 1.9.

When X-rays or γ-rays from flares impact on the detectors the energetic photons release electrons, which in turn lose energy creating many electron-hole pairs (Smith, April 2002). A strong magnetic field across the detectors causes the electrons and holes to drift towards the electrodes where a current pulse is generated. The total charge in the pulse is proportional to the photon energy. The pulse is registered as a count with a certain size depending upon the

incident photon energy, resulting in a count rate spectrum stored as observational summary data.

RHESSI Detector Response Matrix :

The response matrix is a non-diagonal (N × M) array defining the probability distributions of counts (N elements) per detected photon (M elements) for all photon energies (keV). Hence, the DRM has dimensions of count energy and photon energy. The full RHESSI response matrix is presented in figure 1.10 (Smith, 2002). The DRM is constructed prior to the launch of the satellite and is unique for different attenuator states and different detectors. The DRM will be discussed in more detail in chapter 3.

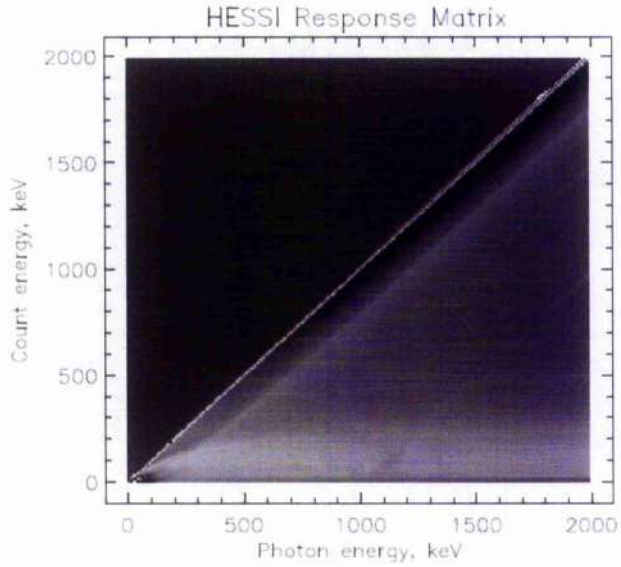

Figure 1.10: The full RHESSI response matrix shows a diagonal photon peak (diagonal line), Compton edge (the ridge below the diagonal line), and backscatter peak (near horizontal ridge near 200keV count space energy).

RHESSI Attenuators :

Each detector views flare emission through four beryllium windows and four blankets of multilayer aluminized Mylar insulation. Absorption of the X-ray energies of interest here is dominated by the Mylar insulation (Philips et al., 2006). Attached on-top of the spectrometer

are two lightweight movable frames each of which carries 9 aluminium disks (attenuators) that can be moved in front of the detectors (Smith et al., 2002). They are designed to cut down the photon flux during high intensity flares, through absorption of low energy photons and preventing saturation of the detectors for measurement purposes and also to increase the lifetime of the detectors.

In normal circumstances the attenuators are held out of the line of sight of the detectors with the sun. This is known as the A0 attenuator state. As the X-ray counting rate increases above a prescribed level, the thin attenuators are inserted in the field of view. This is the A1 attenuator state. Attenuator state A2 (thick attenuators only) is not used in practice since it is so similar to A3. If the emission rises further to another prescribed count rate level, the thin/thick attenuators are inserted. This is called the A3 attenuator state. The transmission factor drops, due to a reduction in count rate, to 1% at ~4keV in the A0 state,~8keV in A1 state and ~13keV in the A3 state (Philips et al., 2006). The effect of the attenuation in any state is significant for incident photons with energies up to ~35keV.

1.2 Motivation for thesis

In this thesis I will examine a number of HXR solar flare events observed by RHESSI. Through such hard X-ray detection and spectrometry of flares we can interpret accelerated electron dynamics in the source volume of the flare. A strong relation exists between flare energy release and particle acceleration. HXR Spectroscopy will enable me to determine electron flux distributions of the thermal and accelerated non-thermal electrons via the RHESSI detector response matrices (DRM). HXR photons produce counts and result in measured/recorded count rate spectra. In theory, using the cross-section for the interaction between the electron and proton (bremsstrahlung cross-section) will allow us to relate the photon flux to the electron flux using a linear integral relation (Brown, 1971). Likewise, count flux spectra are related to photon flux spectra via a similar integral relation which requires knowledge of the DRM. However, the integral relations between counts and photons,

(first step) and photons and electrons (second step) are integral equations (Volterra-type) (Craig & Brown, 1986), and so their inversions are unstable due to the non-diagonal nature of the DRM and bremsstrahlung cross-section, resulting in large noise amplification in the recovered solutions. This will be covered in more detail in chapter 3. Introduction of a new approach which greatly simplifies the problem at hand will contain both steps, from counts to photons then photons to electrons, into one step from counts to electrons, without losing fidelity in the recovered electron flux spectrum. A one step process rather than two is more efficient, more attractive, and statistically more desirable for recovering detail in the regularized solution, and hence a truer interpretation of particle acceleration mechanisms in flares. Firstly, I must define the integral relations discussed above for thermal and non-thermal X-ray emissions.

1.3 Hard X-Ray Emission Processes

X-ray radiation is the product of both thermal and non-thermal electron interactions and is observed in the photon flux spectra, with distinguishable thermal and non-thermal spectral components. Knowledge of the hard X-ray photon flux spectrum $I(\varepsilon)$ from the whole flare volume tells us about the mean electron flux spectrum $\bar{F}(E)$, via the bremsstrahlung cross-section $Q_b(\varepsilon, E)$ of the electron-proton interaction. Since X-rays of energy ε are not produced significantly in electron-proton bremsstrahlung by electrons of kinetic energy $E \geq \varepsilon$ (Koch and Motz, 1959), a cross-section with application of the Elwert (1939) correction to the relativistic bremsstrahlung cross-section of Haug, 1997 will be adequate. The bremsstrahlung cross-section of Haug (1997) will be used throughout this analysis.

1.4 Thermal Bremsstrahlung

Thermal emission due to electrons can be either black body emission or thermal bremsstrahlung. However, black body emission is not relevant to flares since the optical thickness of the material in the X-ray range is not sufficient. Consequently, we need consider only thermal bremsstrahlung which results when the plasma becomes hot enough for ionization leading

to free-free transitions of electrons.

An isothermal plasma in thermal equilibrium has a *Maxwellian* distribution of electron velocities. This results in an exponential drop off in the photon flux spectra (see figure 1.11) due to bremsstrahlung emission of electrons in the hot plasma. The result is that there are very few highly energetic thermal photons and mostly soft X-rays are emitted, such that $I(\varepsilon) \propto \frac{1}{\varepsilon} \cdot e^{-\varepsilon/kT}$. Here, I($\varepsilon$) is the photon flux (photons $\sec^{-1}$ $\mathrm{cm}^2\,\mathrm{keV}^{-1}$)as a function of photon energy ε (keV), with Boltzmans constant k and temperature T (Kelvin).

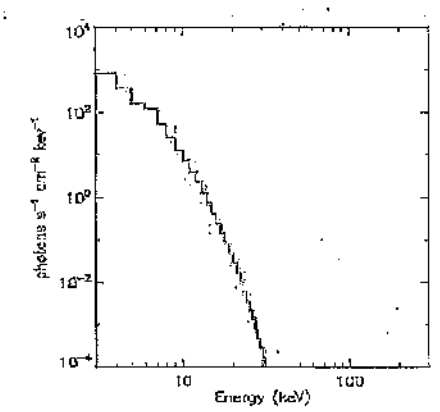

Figure 1.11: Illustration of thermal bremsstrahlung spectrum indicates rapid exponential decrease in photon flux intensity between SXR emission to HXR emission.

The number of HXR photons emitted in general by bremsstrahlung is expressed as:

$$\frac{dI}{d\varepsilon}\,dV = n_p n_e(E) v_e(E) Q_b(\varepsilon, E)\,dV \tag{1.1}$$

where n_p is the target proton density, $v_e(E)$ is the electron velocity and $n_e(E)$ is the fast electron density. Equation 1.1 tells us about the photon flux per unit range of photon energy (ε), locally in the emitting volume (dV)(cm^3). Equation 1.1 can also be expressed as an integral relation, giving

$$\frac{dI}{d\varepsilon} = \int_V n_p n_e(E) v_e(E) Q_b \, dV. \tag{1.2}$$

However, the above expression is for mono-energetic electrons. A flux spectrum of electrons $F(E)$ is equivalent to $n_e(E)v_e(E)$ such that

$$F(E)dE = v(E)\frac{dn_e}{dE}dE, \tag{1.3}$$

We can then calculate the photon flux density spectrum I(ε) (photons sec^{-1} cm^{-2} keV^{-1}), observed at Earth, from the entire source volume V since we know $R = 1$ AU, namely (with Q=0 for $\varepsilon > E$) (Brown 1971, Brown et al. 2003,2006).

$$I(\varepsilon) = \frac{1}{4\pi R^2}\int_V n_p(r)\int_\varepsilon^\infty F(E,r)Q_B(\varepsilon,E)dE\,dV. \tag{1.4}$$

Above, F(E,r) is the local electron flux density spectrum (electrons cm^2 sec^{-1} keV^{-1}) at position r in the source volume V. The thermal component of the bremsstrahlung emission is found by considering a hot ($\geq 10^7$K) plasma with electron density n_e, and isothermal Maxwellian energy distribution with constant temperature T and volume V (Brown, 1974; Prato et al., 2006), giving

$$F(E,r) = \frac{2^{3/2}}{(\pi\, m_e)^{1/2}}\frac{n_p(r)E}{T^{3/2}}exp(-E/T). \tag{1.5}$$

where T is in energy units. Note that Boltzmans constant is needed only if we measure temperature in degrees Celcius and is not when temperature is in energy units, ergs or keV. The thermal component of the photon flux spectra observed at Earth is a result of bremsstrahlung emission with stationary protons of equal number density across the source volume.

Through substituting equation 1.5 into equation 1.4 we get

$$I(\varepsilon) = (\frac{1}{4\pi R^2})(\frac{2^{3/2}}{(\pi\, m_e)^{1/2}})\int_V n_p^2(r)\int_\varepsilon^\infty \frac{E}{T^{3/2}}exp(-E/T)Q_B(\varepsilon,E)dE\,dV. \tag{1.6}$$

From equation 1.6 it can be shown that increasing the electron energy E will result in exponential decrease of $I(\varepsilon)$. Since the electron energy is directly proportional to the photon

energy ε, the photon flux must therefore be inversely proportional to the photon energy. This results in exponential decrease in the photon flux with photon energy.

1.5 Non-Thermal Bremsstrahlung

Three possible non-thermal X-ray emission mechanisms in solar flares are collisional bremsstrahlung, Inverse Compton Scattering and Synchrotron Radiation, otherwise known as Magneto - bremsstrahlung, is produced by relativistic electrons spiralling in a magnetic field. Synchrotron radiation requires the electron distribution function to extend into the several MeV energy range and so is unlikely to be a plausible mechanism for flare hard X-rays, due to high synchrotron energy loss rates. Inverse Compton scattering was ruled out as it also required relativistic electrons and high radiation density. Korchak (1967, 1971) concluded that electron-ion collisional bremsstrahlung was the primary mechanism for producing non-thermal HXR radiation. Collisional bremsstrahlung emission is applicable to both thick and thin target plasma sources. Non-thermal electrons in plasma do not exhibit Maxwellian distributions of electron velocities. Instead, they are observed to have more like a power law spectrum ($\varepsilon^{-\delta}$) with a roughly constant spectral index (δ), see figure 1.12.

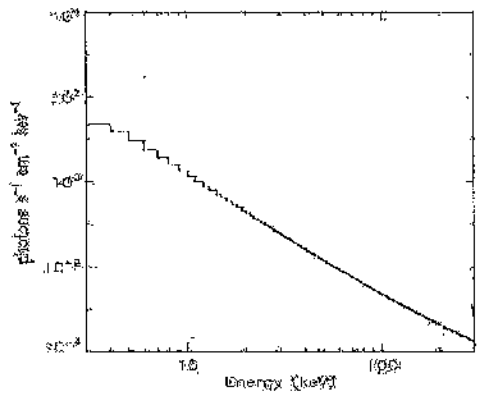

Figure 1.12: Illustration indicating a typical non-thermal bremsstrahlung HXR power law spectral model taken from OSPEX (Object Spectroscopy Executive) package.

Non-thermal models invoke a population of electrons in both the loop-tops and foot-points resulting in thin and thick target emission models, respectively (de Jager and Kundu,1963; Arnoldy, Kane, Winckler, 1967; Brown, 1971).

- **The Thin Target Scenario** :

It has been discussed that accelerated electron beams traverse magnetic flux tubes in the corona directed by magnetic field lines, releasing part of their energy into space as bremsstrahlung HXR photons, before continuing to precipitate into the dense chromospheres. Within the loop-top HXR source (thin-target) the non-thermal electrons emit characteristic hard X-ray radiation via non-collisional bremmstrahlung. Thin target sources occur whenever non-thermal electron beams leave the X-ray source with no significant change of energy. In the limit where the energy losses are small the situation is termed thin target. Hence, if the escape time $\ll$ the electron stopping time then the target is thin or the collisional mean free path is long compared with the loop length.

We now want to consider again equation 1.2 in order to determine the bremsstrahlung photon flux spectrum ($I(\varepsilon)$), due to thermal and non thermal electrons expressed through the mean electron flux distribution $\bar{F}(E)$. For thin target X-ray emission

$$I_{thin}(\varepsilon) = \int_V n_p(r) \int_\varepsilon^\infty F(E,r) Q_b(\varepsilon, E)\, dE\, dV, \tag{1.7}$$

which can be rewritten as (Brown, 1971)

$$I_{thin}(\varepsilon) = \int_\varepsilon^\infty Q_b \left(\int_V n_p F(E) dV \right) dE \tag{1.8}$$

$$= V \bar{n}_p \int_\varepsilon^\infty Q_b(\varepsilon, E)\, \bar{F}(E)\, dE \tag{1.9}$$

where

$$\bar{n}_p = \frac{1}{V}\int_V n_p(r)\,dV \tag{1.10}$$

and the mean electron flux distribution is defined as:

$$\bar{F}(E) = \frac{1}{\bar{n}_p}\int_V F(E,r)n_p(r)\,dV \tag{1.11}$$

The mean electron flux distribution $\bar{F}(E)$, averaged over the data integration time, is the only quantity that can be inferred unambiguously from the X-ray photon flux spectrum $I(\varepsilon)$ (Brown et al. 1971, 2003). $\bar{F}(E)$ is weighted with respect to the plasma proton density n_p, and is the equivalent $F(E)$ in a homogeneous source of density n_p.

- **The Thick Target Scenario :**

When propagating electrons lose all their energy after injection into a source during the observation time, the source target is thick. If fast electrons are injected into the dense chromosphere from the corona they decay very rapidly due to Coulomb collisions, also radiating hard X-rays. Such thick-target emission photon spectra can be predicted from the electron injection spectrum, $\mathcal{F}_0(E_0)$ $(E(z=0)=E_0)$, to be defined, where z is along the electron path.

The relation between the volume averaged fast electron distribution $F(E)$ and the injection spectrum $\mathcal{F}_0(E_0)$, depends on how the electrons lose energy. The energy loss rate (keV s^{-1}) purely by Coulomb collisions of electrons in a plasma is

$$\frac{dE}{dt} = -Q_c(E)n_p v_e E = -\frac{2\pi\, e^4 \Lambda\, n_p v_e}{E} \tag{1.12}$$

where $Q_c(E) = 2\pi\, e^4\Lambda/E^2$ is the Coulomb energy loss cross-section, Λ is the Coulomb Logarithm which is treated as a constant, and $v_e(E)$ is the electron velocity.

Consider an electron with initial energy E_0 incident on a thick target plasma emitting

collisional bremsstrahlung radiation until $E \leq \varepsilon$. The number of photons per unit energy $\nu(\varepsilon, E_0)$, per unit ε emitted during the electron lifetime is given by

$$\nu(\varepsilon, E_0) = \int_{t_0\ start(E=E_0)}^{t_1\ end(E=\varepsilon)} n_p Q_b(\varepsilon, E(t)) v_e(t)\, dt \tag{1.13}$$

$$- \int_{\varepsilon}^{E_0} \frac{Q_b(\varepsilon, E)}{E Q_c(E)}\, dE \tag{1.14}$$

This expression is derived through substituting the energy loss rate equation 1.12 in the form $dt = dE/Q_c E n v$ into equation 1.14.

The expression for the thick target X-ray photon flux spectrum, observed at Earth (Brown, 1971), is given by

$$I_{thick}(\varepsilon) = \frac{A}{4\pi\, R^2} \int_{\varepsilon}^{\infty} \mathcal{F}_0(E_0) \int_{\varepsilon}^{E_0} \frac{Q_b(\varepsilon, E)}{E Q_c(E)}\, dE dE_0 \tag{1.15}$$

Here, A is the injected ion area.

The mean electron distribution function (equation 1.11) equivalent of $\mathcal{F}_0(E_0)$ (Brown and Emslie, 1988) is given as

$$\bar{F}(E) = \frac{A\, E}{K \bar{n} V} \int_{E}^{\infty} \mathcal{F}_0(E_0) dE_0, \tag{1.16}$$

Conversely, we can derive the electron injection spectrum from $\bar{F}(E)$, given by

$$\mathcal{F}_0(E_0) = -\frac{K \bar{n} V}{A} \left[\frac{d}{dE} \frac{\bar{F}(E)}{E} \right]_{E=E_0}. \tag{1.17}$$

Inferring Mean Electrons from Photons :

Equation 1.9 has the form of a linear (Volterra-type) integral equation (of the first kind). The most general form of any such linear integral equation is

$$\alpha(x)f(x) + \lambda \int_{a(x)}^{b(x)} k(x,y)f(y)\,dy = g(x). \tag{1.18}$$

λ is a known constant, $\alpha(x)$ is a known function, $f(y)$ is the source function to be determined, $g(x)$ is the given data function, and $k(x,y)$ is the kernel of the equation. When $\alpha(x)$ is zero, then λ can be set to unity, and the integral equation is of the *First Kind* (Craig & Brown, 1986). When $b(x)$ is constant we define the Volterra type equation as

$$\int_{a(x)}^{b} k(x,y)f(y)\,dy = g(x). \tag{1.19}$$

In our problem, $Q_b(\varepsilon, E)$ is the known kernel function and solution of the equation gives $f = \bar{F}(E)$ from the hard X-ray photon spectrum $g = I(\varepsilon)$.

To solve the practical problem we have to solve such functional forms (**F**,**I**,**Q**) as discretized source and data vectors (**F**, I) and kernel matrix (**Q**), giving simply

$$\mathbf{QF} = \mathbf{I}. \tag{1.20}$$

where $\mathbf{I} = \mathbf{I_j}$ such that $\mathbf{I_j} = I(\varepsilon_j)$ etc. The formal solution for the mean electron distribution function is an inversion of the matrix equation, expressed as

$$\mathbf{F} = \mathbf{Q^{-1}I}. \tag{1.21}$$

It is widely accepted that the inversion of the kernel matrix is problematic due to off-diagonal elements creating issues of non-uniqueness, instability and ill-posedness in the recovered solution of F (Craig & Brown, 1986; Johns and Lin, 1992; Thompson et al., 1992; Piana, 1994; Piana et al., 2003; Massone et al., 2003; Kontar et al., 2004, 2005). In particular inversion with different cross-sections (eg. Bethe-Heitler, Kramers) can lead to the following situations (Brown, 2004)

- $\mathbf{Q}^{-1}\mathbf{I}$ does not exist for some $I(\varepsilon)$.

- $\mathbf{Q}^{-1}\mathbf{I}$ exists but is not unique for some $I(\varepsilon)$.

- $\mathbf{Q}^{-1}\mathbf{I}$ exists and is unique but is unstable for small changes in $I(\varepsilon)$.

- $\mathbf{Q^{-1}I}$ exists but is unphysical (**F** negative) for some $I(\varepsilon)$.

This inversion problem has achieved unprecedented importance because of the high resolution photon spectra ($\Delta\varepsilon \sim 1$ keV) obtained from RHESSI. More importantly, the knowledge of possible features in reconstructed forms of photon and mean electron spectra could yield important information on plasma heating and conduction processes (Brown, 1974; Brown, Melrose and Spicer, 1979; Gabriel, 1992). Most inversion methods have been formulated within the framework of regularization theory for ill-posed inverse problems (Bertero, 1989), such as with Tikhonov regularization methods (Tikhonov, 1963). The issues of ill-posed inverse problems and regularization techniques will be explored further in chapter 3 and 4.

Inferring photons from counts C(ε) :

In order to infer electron distributions $\bar{F}(E)$ we must first determine the photon flux data vector (**I**) from the measured, discretized data function for the count flux **C**, using the detector response matrix (DRM) as the known kernel matrix. So to infer $I(\varepsilon)$ from $C(\varepsilon)$ we can again express this relation in discretized matrix form as

$$\mathbf{C} = (\mathbf{DRM}) \cdot \mathbf{I}. \tag{1.22}$$

DRM is the detector response matrix.
Following inversion of the **DRM** matrix (array of probability distributions for conversion from count energy space to photon energy space) we can write a solution for the photon flux spectrum as

$$\mathbf{I} = (\mathbf{DRM})^{-1}\,\mathbf{C}. \tag{1.23}$$

As with inferring electrons from photons, inversion of the **DRM** matrix is ill-posed and unstable making direct inversion for **I** problematic due to noise amplification, resulting from instrumental effects in the detector and background radiation. The double inversion proce-

dure in getting to $\bar{\mathbf{F}}$ from $\mathbf{C}$ worsens the overall instability. As a result, a single combined inversion procedure, proposed in this thesis in chapter 4, may help recover $\bar{\mathbf{F}}$ more faithfully. Direct inversion of $\mathbf{I}$ from $\mathbf{C}$ data is considered in greater detail in chapter 4 of this thesis, and tested on selected flare events.

We first consider simpler parametric forms (power law spectra) of the mean electron distribution function $\mathbf{F}$ to determine some interesting relations between the mean electron distribution and the X-ray photon flux spectrum, which are unique in both the thin and thick target scenarios.

Parameterization of $\bar{\mathbf{F}}(\mathbf{E})$

The mean electron flux $\bar{F}(E)$ (electrons $\sec^{-1}$ cm^{-2} keV^{-1}) is often expressed as a power law

$$\bar{F}(E) = C\,E^{-\delta}. \tag{1.24}$$

Here C can be expressed in terms of the total flux, $F_1(\mathrm{cm}^{-2}\ \sec^{-1})$, of electrons of energy $E \geq E_1$ namely

$$\bar{F}(E) = (\delta - 1)\frac{F_1}{E_1}(\frac{E}{E_1})^{-\delta}. \tag{1.25}$$

The spectral index value δ differs between thin and thick target scenarios, for the same photon spectrum. For simple cross-sections the corresponding HXR spectrum for emission from both thin and thick target scenarios will also have a power law distribution of energies ε, expressed as:

$$I(\varepsilon) = a\varepsilon^{-\gamma} \tag{1.26}$$

where γ is the spectral index of the HXR spectrum. This can be proved below. The spectral index γ is graphically described by the log-log gradient of a HXR spectrum and γ

is dependent on δ. Inserting the parametric form (equation 1.25) of $\bar{F}(E)$ into equation 1.2, we get

$$\int_{\varepsilon}^{\infty}\int_{V} n_p n_e v_e Q_b \, dV dE = (\delta - 1)\frac{F_1}{E_1}\Delta N A \int_{\varepsilon}^{\infty}(\frac{E}{E_1})^{-\delta} Q_b(\varepsilon, E)\, dE, \tag{1.27}$$

For a dimensional source of area A then $\Delta N = \int_z n_p \, dz$ is the column density of the source (assumes Δ N is small). To show the relation between this $\bar{F}(E)$ and the HXR spectrum we use the bremsstrahlung cross section $Q_b(\varepsilon, E)$ (Haug, 1997) hence

$$I_{thin}(\varepsilon) = (\delta - 1)\frac{A\Delta N}{4\pi R^2}\frac{F_1}{E_1}\int_{\varepsilon}^{\infty} E^{\ (\delta\,|\,1)} Q_b(\varepsilon, E)\, dE \tag{1.28}$$

where $I_{thin}(\varepsilon)$ has units (cm^{-2} keV^{-1} sec^{-1}). It can be seen from equation 1.28 that, after integration by parts (Brown, 1971), we get the relation

$$I_{thin}(\varepsilon) \propto \varepsilon^{-(\delta+1)} \tag{1.29}$$

Here we see that in the case of thin target emission the spectral index for the HXR spectrum is larger than that of the source electron spectrum, i.e.

$$\gamma = \delta + 1. \tag{1.30}$$

Using this same power law description and cross-section it can be shown that the non-thermal electron distribution spectral indices for a thick emission model, with respect to the HXR spectral indices, have the following relation (Brown, 1971)

$$\gamma = \delta - 1 \tag{1.31}$$

Hence, equation 1.31 and 1.30 show that the photon spectral index γ for the same electron distribution (index δ) will always differ by 2 between thick and thin target non-thermal spectra.

1.5.1 Use of the Parameterized $\bar{F}(E)$

The problems we are faced with in this thesis are two fold. Firstly we want to determine accurately the true HXR photon flux spectrum from the count rate spectrum, for a number of flare events, observed and recorded with the RHESSI spectrometer. Secondly, we want to apply to the photon flux spectrum of the observed, the derived linear integral equation for thin target emission to infer the mean electron flux distribution. In both problems we are faced with a problematic unstable inversion procedure. One solution to such problems is the forward fitting technique which avoids the difficulties presented by direct inversion of the linear integrals relating count spectra to photon spectra. Forward fitting was first applied to RHESSI observations by Holman et al. 2003. Through the forward fitting technique I can predict, for parametric models of $\bar{F}(E)$, their respective HXR spectra in count space, as recorded by RHESSI, with the aid of RHESSI spectral analysis Solar Software (SSW) and OSPEX (Object Spectroscopy Executive). In this approach, a parametric form of $\bar{F}(E)$ is assumed, and the corresponding form of the HXR photon model predicted. Finally, through parameter adjustment and re-fitting the best form of $\bar{F}(E)$ is found. Ultimately, determination of the true photon flux spectrum inferred from the count flux spectra may be crucial for accurate reconstruction of $\bar{F}(E)$. In Chapter 2, I will spectrally analyze a number of flare events from the RHESSI flare catalogue using the forward fitting technique with χ^2 testing to produce a resulting mean electron distribution spectrum for each event. The 3 flare events chosen will each have different attenuator states during their impulsive phases, for the purpose of comparing the impact of attenuators during the analysis of the photon and mean electron flux spectra. In Chapter 3, I will discuss the linear integral equation relating the count flux spectrum to the photon flux spectrum and solve it (direct inversion) for each of the flare events selected. In Chapter 4, I will go on to analyze both the mean electron distribution spectrum and photon flux spectrum of each flare event, using generalized regularized inversion algorithms, following a discussion of this regularized inversion technique. In Chapter 5, conclusions are drawn on the quality of the results obtained and techniques used with respect to the selected events, in order to shed more accurate light on the complexities of these violent and dynamic processes.

Chapter 2

Spectral Analysis with RHESSI

"The remote observer finds himself in a situation, akin to that of a spectator at a magic show, ..."

I J D Craig & J C Brown, 'Inverse Problems in Astronomy',1986

2.1 Motivation

I will now spectrally analyze three contrasting flare events, which occurred on 17^{th} September 2002 (A0 state), 12^{th} April 2002 (A1 state) and 31^{st} October 2003 (A3 state). The special nature of these events concerns their attenuator states. Each event has recorded the impulsive phase of the respective flare in a different attenuator state. The impulsive phase is important since the hard X-ray emission occurs during this phase and so the fit interval for forward fitting will occur during the period when the attenuators are in position for the 12^{th} April 2002 and 31^{st} Oct. 2003 events. Problems arising in this analysis, such as effects of the attenuator state of the detectors will also be examined, and conclusions drawn on whether the attenuators are due major consideration in spectral analysis. More importantly, however, I will study the inferred mean electron distributions from the HXR spectra.

2.1.1 Generating the Count Rate Spectrum

The RHESSI spectral analysis package produces a count flux spectrum from the count rate, in units of counts (sec^{-1} cm^{-2} keV^{-1}), corrected for known instrumental effects (Smith et al. 2002), which include:

- Absorption in Mylar blanket, cyrostat windows and grids.
- Compton scattering into and out of the detectors.
- Compton scattering off the Earth's atmosphere, particularly affecting rear segments below 100keV.
- Noise in the electronics - background counts.
- Low energy cut-off imposed by the electronics.

A file containing the Spectral Response Matrix (SRM), which contains all detector responses in all attenuator states, is generated initially to account for instrumental effects, decimation and energy binning calibration. The DRM represents photon to count conversions per photon energy for the specified detectors and attenuators present during the fit interval of the spectral analysis. Flare events are dealt with on a case-by-case basis.

The RHESSI OSPEX package contains all the procedures necessary to read the fits data files, prepare and plot light curves, images and spectra. (Lin et al. 2002). OSPEX allows control of background removal and is used to convert the count-rate spectrum into the spectrum of the incident photons.

2.1.2 Flare Selection

When searching the flare catalogues with the RHESSI software, I flagged for flares with relatively high total counts and with a particular attenuator state during the flare peak. There were also to be no particle precipitation or non-solar events during the observation. The

Flare	17^{th} Sept. 2002	12^{th} April 2002	31^{st} Oct. 2003
Number	2091709	2041209	3103110
GOES Class	C2	M1	C3
Start Time	05:49:08	13:07:36	11:21:32
End Time	05:57:28	13:16:08	11:22:56
Total Counts	211440	697572	15576
Energy Range (keV)	3 - 300	3-300	3 - 300
Flags	**A0(None)**	**A1(thin)**	**A3(thick and thin)**

Table 2.1: List of flares selected for spectral analysis and their characteristics

selected flares and their characteristics are tabulated in Table 2.1.

The observational summary is a representation of the flare time profile presented as count rate (counts sec^{-1} $detector^{-1}$) versus time for selectable energy intervals between the start and end time indicated in Table 2.1 and presented in figure 2.1.

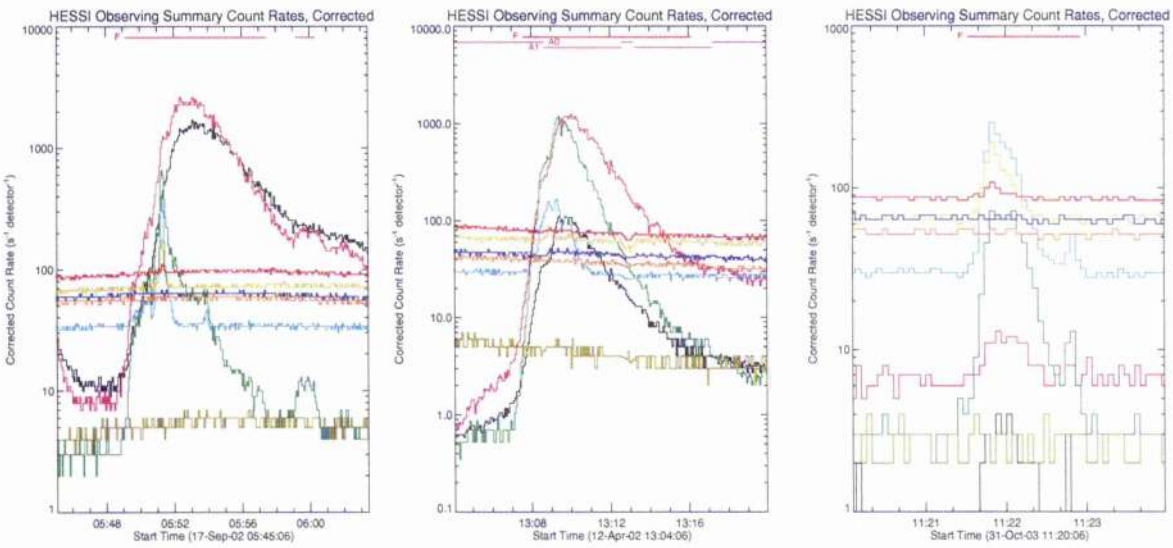

Figure 2.1: Observational summaries for each flare event stored in flare catalogues 3-6keV (*Black*), 6-12keV (*Magenta*), 12-25keV (*Green*), 25-50keV (*Blue*), 50-100keV (*Yellow*), 100-300keV (*Red*).

Photons with energies ranging from soft X-rays up to very hard X-rays are clearly detected by the RHESSI germanium detectors during flare impulsive phases. The horizontal red line at the top of the 17/09/02 graph indicates that all attenuators were out of the detector fields of view at this time. For the 12/04/02 RHESSI event the horizontal line drops during the impulsive phase of the flare to the A1 state on two occasions and during the 31/10/03

event RHESSI remains in attenuator state A3 throughout. The count rate for the 12/04/02 event at all energies up to 25keV rose very rapidly until about 13:08 UT when the thin attenuators moved into the detector fields of view. (Notice that positioning of the thin shutters occurs where the total count rate exceeds 10,000 counts per second). Thereafter, the thin attenuators were removed for 1-minute intervals to test the low energy rate from the flare, with clear changes in the counting rate. Finally, at about 13:20 UT, the rates began to drop to their non-solar background levels as the flare entered the gradual phase. The total count rate for the 17/09/02 RHESSI event peaks at around 2,000 counts per second, hence there was no requirement for attenuators to be positioned. However, the 31/10/03 event has thick shutters in position continuously. It is the largest event here since the count rate is in excess of 100,000 counts sec^{-1} $detector^{-1}$, hence thick shutters are positioned. I have chosen 4 seconds as the optimum time resolution for all observations because this is the time for which count rates are independent of rapid modulation as the satellite spins. RHESSI rotates about its own axis approximately 15 times in one minute.

2.1.3 Energy Binning Considerations

It is important to remember that the selection of energy bin widths, over the entire energy range under observation, should be small enough that the thermal and non-thermal components of the spectra are distinguishable, but not so small that the uncertainties get too large. Energy observations down to 1 keV energy are to be desired for the flare events. Using 1keV bins up to approximately 15 keV give the best information on the iron and nickel lines at ~6.7 and ~8 keV respectively. However, 1 keV resolution gives a large count noise uncertainty for high energy photons. As a consequence, in this analysis I have chosen to use variable energy binning:- 1keV from 3 to 40 keV, 3 keV from 40 to 100 keV, 5 keV from 100 to 150 keV, and 10 keV from 150 to 300 keV. This binning selection will be used for all the flares observed to limit uncertainties in the energy intervals particularly at higher energies when the bin widths become greater. Changing the size of the energy bin widths becomes important when we consider the signal to noise ratio, with respect to the robustness of the results. Increasing the bin size presents results which become increasingly less robust and

exhibit significantly larger noise instabilities at higher energies. This is turn creates larger deviations in the residuals of the fits, and affects our judgement of the goodness-of-the-fits. Signal to noise is considered in more detail in the "Error Analysis" section of this chapter.

Restrictions on Energy range selection :

When constructing count flux spectra, it is to be noted that all the counts below 6keV suffer from K-escape in the presence of an attenuator state (A0, A1), and do not provide information about the incident photon spectrum (Smith et al., 2002). This phenomenon is a result of ionization of a germanium atom by an incident photon with energy above the germanium K-edge at 11.1 keV. The ionized atom will almost instantly emit a Kα or a Kβ photon with energies 9.25 keV and 10.3 keV respectively (Phillips, Chifor & Dennis, 2006). Hence, the minimum energy for the fits will be approx. 10keV. The maximum energy will also be limited for each flare analysis. Noise and other instrumental effects again restrict how far, in terms of photon energy, we can fit. When the count uncertainty becomes too great and the background emission exceeds the flare emission, the relevant energy range for analysis (fit energy range) will have reached its upper limit. This will mostly occur below our maximum of 300 keV, at approximately 100 keV, and will be dependent on the selected flare. Hence, the total energy band width for each event in this analysis is from 10 - 100 keV i.e. hard X-ray range.

2.1.4 The Count Flux Spectrum

Only front segments will be considered for all the detectors on all the flares chosen here, excluding detectors 2 and 7. Detector 2 generally had a threshold of $\sim$ 20 keV and should not be used at lower energies. Before March 2004, it was not segmented and all the counts were included in the front segment channel. Its energy resolution is significantly worse than the other detectors. Detector 7 has a threshold of $\sim$10 keV and significantly worse energy resolution than the other detectors[1]. SSW then calibrates the SRM file containing the full

[1]see webpage *'http : //hesperia.gsfc.nasa.gov/ dennis/OSPEX/The_Basics/index.htm'*for more details on detector selection.

RHESSI response matrix, for energy binning, pileup and decimation. I can then proceed to produce the count flux spectrum for each of the flares in units of counts cm^{-2} s^{-1} keV^{-1}. These are illustrated in figure 2.2.

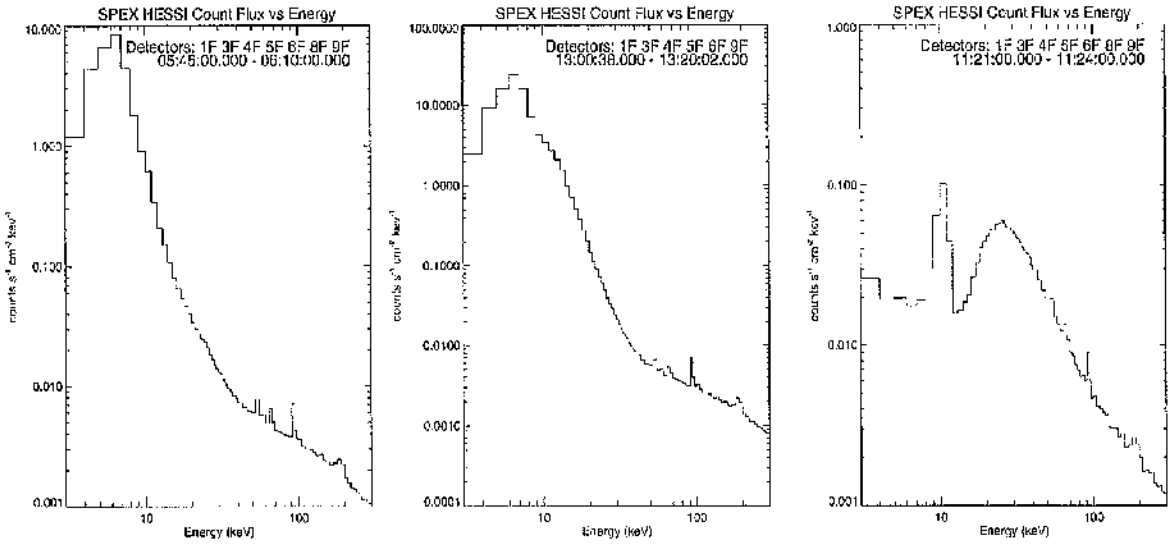

Figure 2.2: Count flux spectrum (counts sec^{-1} cm^{-2} keV^{-1}) of each flare event under analysis, prior to background removal.

In figure 2.2, the sharp peaks that can be seen in the spectrum at energies above 50 keV are lines from the germanium detectors and are not of solar origin. The distortion in the spectra up until approx. 25 keV coincides with the upper limit on the energy range over which the thick shutter attenuators have an influence on the spectrum. The SRM and fits files are transferred to the OSPEX package for background removal and forward fitting of the parameterized electron distribution functions to the count flux data.

2.1.5 Background Removal from the Count Flux Spectrum

To determine the nature of the signal recorded by the detectors we must minimize the extent to which noise interferes with the data stream. The noise in the signal and the sources of error comprise the following elements **Background radiation**, **Instrumental effects**, **Systematic Uncertainty** (built into the OSPEX software accounting for 0-5% of error per count energy bin).

To remove the background we generate background count rate polynomials in time, independently for each energy interval. Background counts during the flare are determined by interpolating between these polynomial background level fits before and after the flare event (Holman et al. 2003). Background estimation intervals defining the start and end of the polynomials are chosen at post and pre flare time periods when background emission dominates. Background radiation can sometimes be considered to be constant through time. However, if the background emission for the post flare period differs from the pre-flare period, we must choose more than two background intervals and map over the data with a higher order polynomial to give a better estimate of the background. Figure 2.3 shows the observed count rate light curves (black) for each energy interval for the 17^{th} Sept. 2002 flare with background count rate polynomials mapped (Green) along with background removed count rate data in each energy interval (purple). With increasing energy from top left to bottom right, the intensity and duration of the impulsive phase in the count rates become progressively reduced by background subtraction since background emission becomes more significant with increasing energy particularly at 100-300 keV. Consequently, the background-removed lightcurves decline to zero where the background polynomial crosses the recorded data.

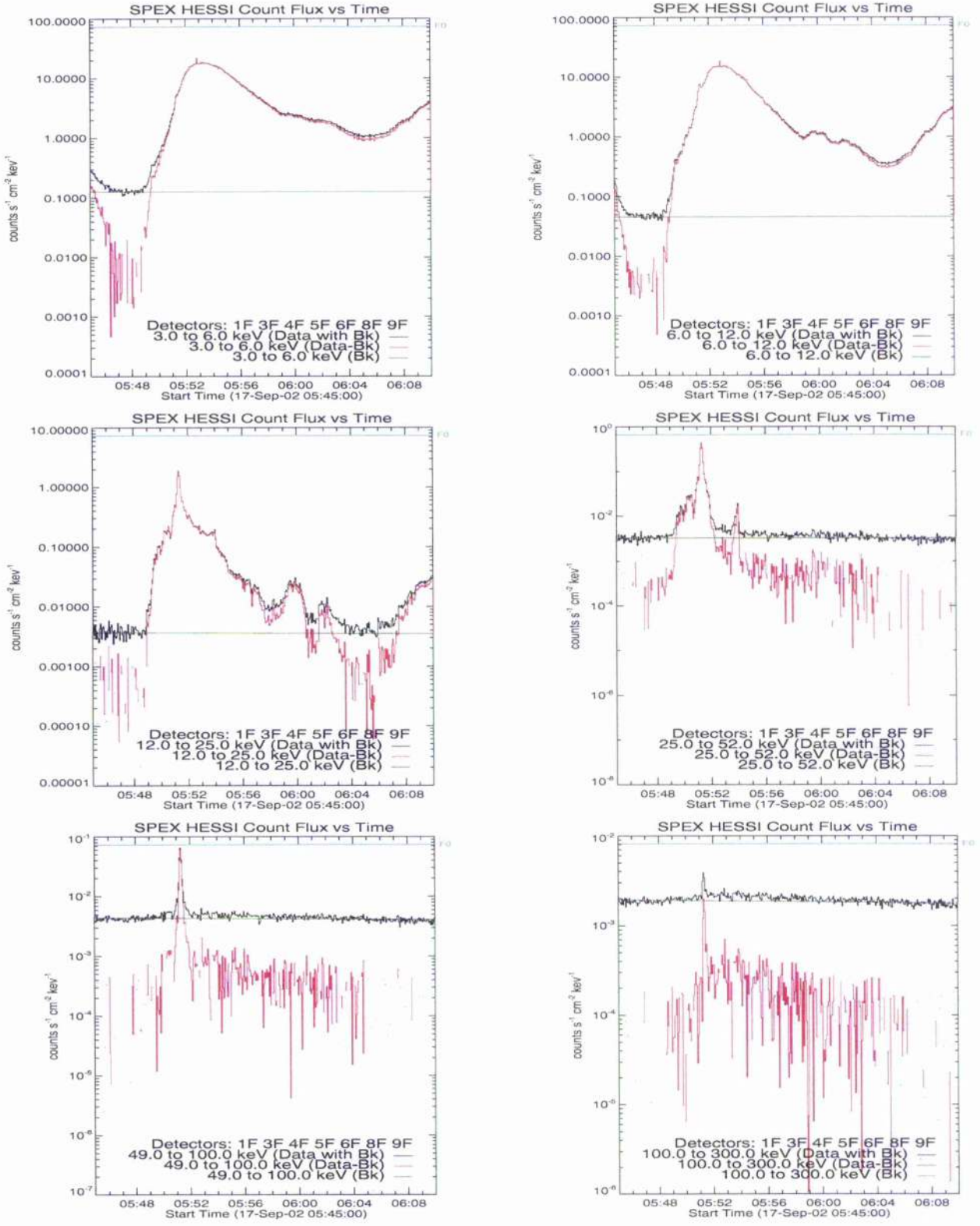

Figure 2.3: Background removal for specific energy intervals on the count flux spectrum for 17^{th} Sept. 2002 flare event.

Figure 2.4, on the left shows a summary of the data with all polynomials for all the energy intervals. The plot on the right is the observation summary for the same event, except it presents *count rate data − minus background counts*. Similar treatment will also be used on the other two flares in this analysis but are not presented here.

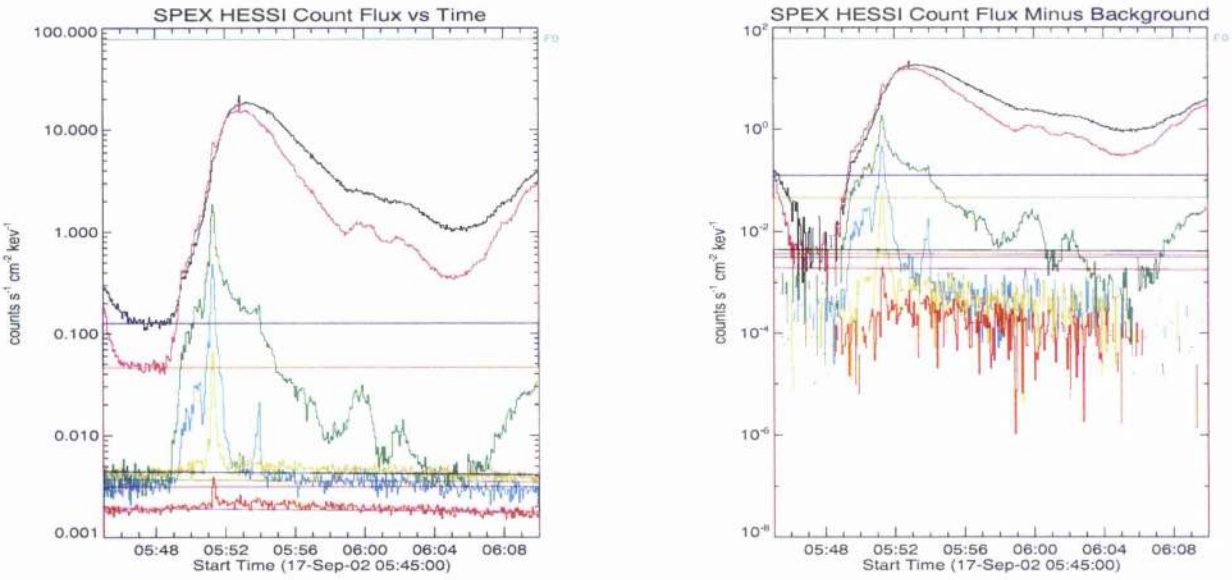

Figure 2.4: Count Flux spectra inclusive of background emission polynomials per energy interval (*Left*). Background removed count flux data with respect to the background polynomials per energy interval (*Right*).

Once the background radiation is removed we can fit the true signal with parametric electron distribution functions and construct forward fitted photon flux models and spectra, for each flare event.

2.1.6 Fitting Parametric Electron Distribution Models

The time interval within which we will fit thermal and non-thermal distribution functions to the count flux spectra will be the period (minutes) which captivates the peak emission of both soft and hard X-rays (10-100 keV). This interval will be selected from the count rate time profile for each flare event in the software and will last as long as there is hard X-ray radiation detection in the background removed data. This period is observed as the flare impulsive phase. The fit interval for the 17^{th} Sept. 2002 event is presented on figure 2.5. Most importantly, the fit interval period must lie within the period in which the attenuators

of interest are in position for the 12/04/02 and 31/10/03 events. The fit interval period cannot be less than 4 seconds i.e. the chosen time resolution of the observation.

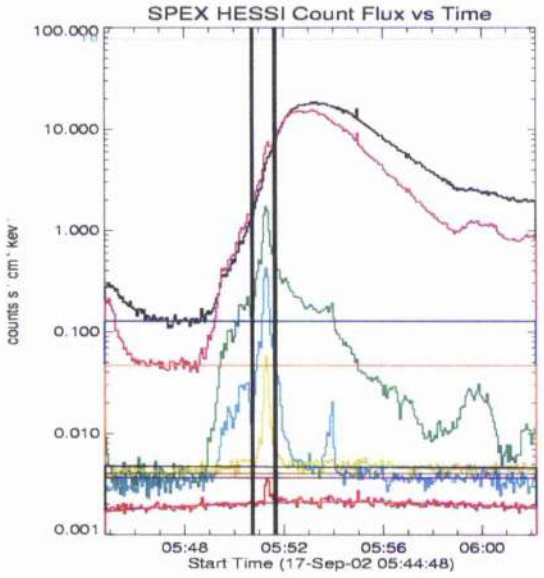

Figure 2.5: The fit interval for the 17^{th} Sept.2002 event. As can be seen, the narrow fit interval covers the period when photons of harder energies exceed the background level. The same procedure applied to the other flare events but not displayed here.

There are a number of parameterized fit functions which can give us information on the electron distribution in the flare. A list of the possible fit functions along with the parameter descriptions is presented in the literature[†], including the thermal, thin target bremsstrahlung, thick-target bremsstrahlung, multi-thermal exponential, broken power law function, triple broken power law function, ion function etc.

Throughout this analysis I chose to fit only the isothermal function plus a thin target double power law distribution function, giving 9 free parameters, for each flare event. The thin-target bremsstrahlung function will represent the non-thermal component of the hard X-ray spectra, which sets 6 parameters (outlined in the bottom table in Table 2.2) allowing control of the low and high energy cutoff in the non-thermal electrons, for an electron distribution with double power law form. A thin-target functional form of incident flux non-thermal spectral component is imperative in this instance, for each event under analysis, in

[†]see OSPEX software within IDL for further details on function properties,titled "Function Descriptions."

order to deduce the mean electron flux of the density-weighted source volume. A description of each parameter is outlined in table 2.2.

Parameter	*Variable Thermal Function – Parameter Description*
1	Emission measure in units of $1 * 10^{49}$cm ^{3}
2	Plasma temperature in keV.
3	Relative abundance for iron and nickel, relative to coronal abundance for chianti.

Parameter	*Thin – Target Bremsstrahlung Function Parameter Description*
4	Normalization factor = (plasma density*source volume*nonthermal electron flux density in $1.0 * 10^{55}$cm$^{-2}sec^{-1}$.
5	Power-Law index of the electron distribution function below break energy.
6	Break energy in electron distribution function (in keV).
7	Power-Law index of the electron distribution function above break energy.
8	Low Energy cutoff in electron distribution function.
9	High Energy cutoff in electron distribution function.

Table 2.2: Fit function parameter descriptions applicable to spectral analysis of all flare events.

2.1.7 Fitting the Models to the Data

Upon estimation of the parameters of the fit functions a photon flux model is subsequently predicted and fitted to the data (count minus background) function. The fitting procedure should provide:

1. Parameters as estimators of a model which are adjusted to achieve a minimum in the merit function (agreement between the model and data), yielding best-fit.

2. Error estimates on the parameters.

3. Statistical measure of the goodness-of-fit.

Starting parameters are determined to ensure that the fit is sufficiently close to the data enabling convergence to the best-fit solution, with a true minimum in χ^2. The systematic error is estimated on the flux in each energy bin, and dominates the random noise at high

count rates (Holman et al. 2003). This error is accumulated in the overall energy bin interval uncertainties, and added in quadrature in the error calculation.

The functions are folded through the detector response matrix (DRM) in a series of iterations for the attenuator state in each flare event, to predict the count flux model. This calculation to convert from modeled photons to modeled counts, using the DRM has already been presented in equation 1.22, in chapter 2. The count flux model is χ^2 tested against the count flux spectrum (background-subtracted) via a least squares minimization which ensures that the free parameters are varied until a minimum χ^2 fit to the count flux is obtained. The results for the selected parameter values for the fit functions, with acceptable fits to of the models to the data, are listed for each of the flare events in Table 2.3. Using the fit of the count flux models to the data we can analyze the data and determine the goodness-of-fit. A χ^2 goodness-of-fit test is applicable here since we assume that the residuals in each energy bin are mutually independent i.e. the residuals between the observed and predicted photon fluxes are assumed to be uncorrelated.

Parameter	$17^{th} Sept.'02$	$12^{th} April'02$	$31^{st} Oct.'03$
1	$4.03 * 10^{-3}$	0.1346	$3.7175 * 10^{-3}$
2	1.6022	1.6117	1.5228
3	0.4334	0.1195	9.5642
4	0.6331	6.2947	0.7562
5	0.6961	0.1101	0.6723
6	50.1568	17.6719	54.5841
7	3.0075	3.4419	2.5726
8	18.5045	1.0230	20.3290
9	300	300	300
Systematic error	0.01%	0.00%	0.01% ,

Table 2.3: Fit function parameter values of the electron flux model assigned for each flare event including the relative uncertainty measure on the errors of each event, and used to estimate the photon flux model. The parameters are described in detail in fig. 2.2.

Converting from Counts to Photons :

Upon acceptable fitting of the count model to the count flux data, a conversion factor relating the count flux model to the photon flux model is acquired. The conversion factor is

fundamentally an approximated configuration of the DRM, used to infer true photons from count space. The evaluation of this factor is model dependent and its fidelity limited by the accuracy of the forward fitting technique. The conversion factor is a unit-less vector and can be expressed as

$$\texttt{Conversion Factor} = \frac{\texttt{Count Flux Model}}{\texttt{Photon Flux Model}} \tag{2.1}$$

where the Count Flux Model = DRM·Photon Flux Model.

Figure 2.6 show how the conversion factor varies across the HXR energy range for each of the flare events.

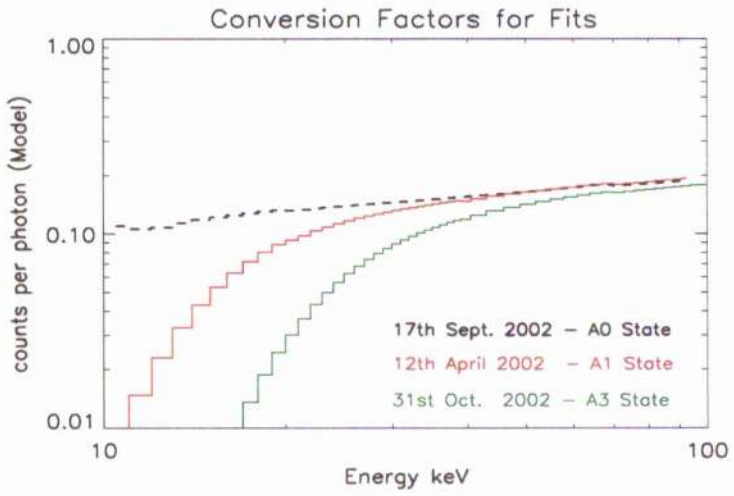

Figure 2.6: The plot displays the conversion factors for each of the flare events for comparison.

The conversion for each of the events does not ever exceed 0.2. With increasing attenuation (going from A0 to A3), it is clear from figure 2.6 that the conversion from photons to counts becomes weaker at lower hard X-ray energies (10-30 keV). This has a considerable impact when one wants to recover accurate photons from counts. It is also interesting to compare figure 2.6 with figure 2.7.

The top line in figure 2.7 represents the attenuation in A0 state, caused by the thermal blankets and beryllium windows positioned above the detectors. The line below the A0 state line represents attenuation for state A1 (thin shutter), followed by A2 (thin-in, thick-out)

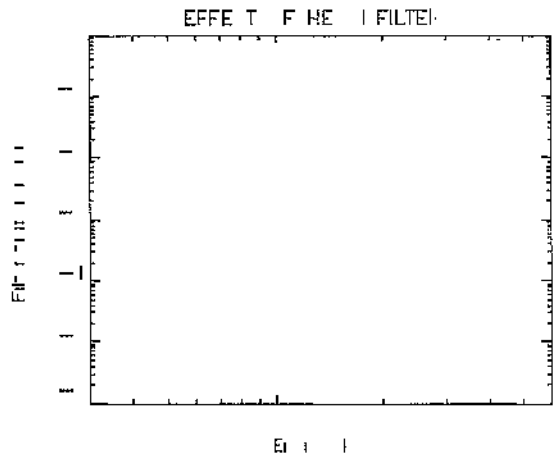

Figure 2.7: Attenuation factor of the different attenuator configurations as a function of energy, taken from Smith, 2002.

(not used with RHESSI) and A3 (thick shutter) (Smith, 2002). The effect of attenuation is significant up to 30-40 keV, as is evident in both figure 2.6 and 2.7, but moreso with conversion factors in state A3. The attenuators substantially diminish the photon flux that reaches the detectors at lower energies (Holman et al. 2003). Hence, the DRM calibration is not well established for lower photon energies particularly in attenuator state A3. We will consider the DRM calibration further with direct inversions in Chapter 3.

The χ^2 Test and Residuals :

I will fit N data points (x_i, y_i) $i = 1, ..., N$, to a model which has M adjustable parameters a_j, $j = 1, ..., M$. Least squares fitting allows us to estimate the maximum likelihood parameters , hence determine which particular set of parameters $a_1, ..., M$ is correct. The maximum likelihood estimate of the model parameters, through least squares fitting within the OSPEX software, is obtained by minimizing a quantity called 'chi-square (χ^2)'. This quantity can be interpreted as the probability of obtaining a normal distribution with mean zero in the residuals of the fit, under the null hypothesis that the expected model is correct. The expected value of the reduced χ^2 is unity, and we can use the residuals of the fit as a measure for the goodness-of-fit of the model. The χ^2 quantity is calculated as follows

$$\chi^2 \equiv \frac{1}{(N-m)} \sum_{i=1}^{N} \left(\frac{y_{obs}(x_i) - y_{fit\,model}(x_i; a_1 \ldots a_m)}{\sigma_i} \right)^2 . \tag{2.2}$$

Above, y_{obs} and $y_{fit\,model}$ are the observed photon flux and the photon flux given by the model at energy ε respectively, $N - m$ is the number of degrees of freedom to which the chi-square distribution is normalized. σ_i is the size of the measurement error in the observed photon flux intervals i. It is the standard deviation in each data point (x_i, y_i). In this analysis $y_{obs}(x_i) = I(\varepsilon_i)$ and $y_{fit\,model}(x_i) = I(\varepsilon_i) = y_{fit\,model}(x_i; a_1 \ldots a_m)$.

The goodness-of-fit should be observed in the context of non-systematic random and reduced residuals. The residuals represent the difference between the fitted model and the data for both photon and count flux spectra. This is the deviation of the data from the model across the entire energy range, normalized to the standard deviation (σ) in the count flux for each energy. The expression for calculating the residuals is as follows:

$$\texttt{Residuals} = \frac{(\texttt{C}_{\texttt{(observed)}}(\varepsilon) - \texttt{C}_{\texttt{fitmodel}}(\varepsilon))}{\sigma(\varepsilon)} \tag{2.3}$$

The plots in figures 2.8 and 2.9 show the fit results for converted photon flux spectrum for each flare event under analysis, along with the fit residuals. The thermal function (green), for all events, is exponential (by definition).

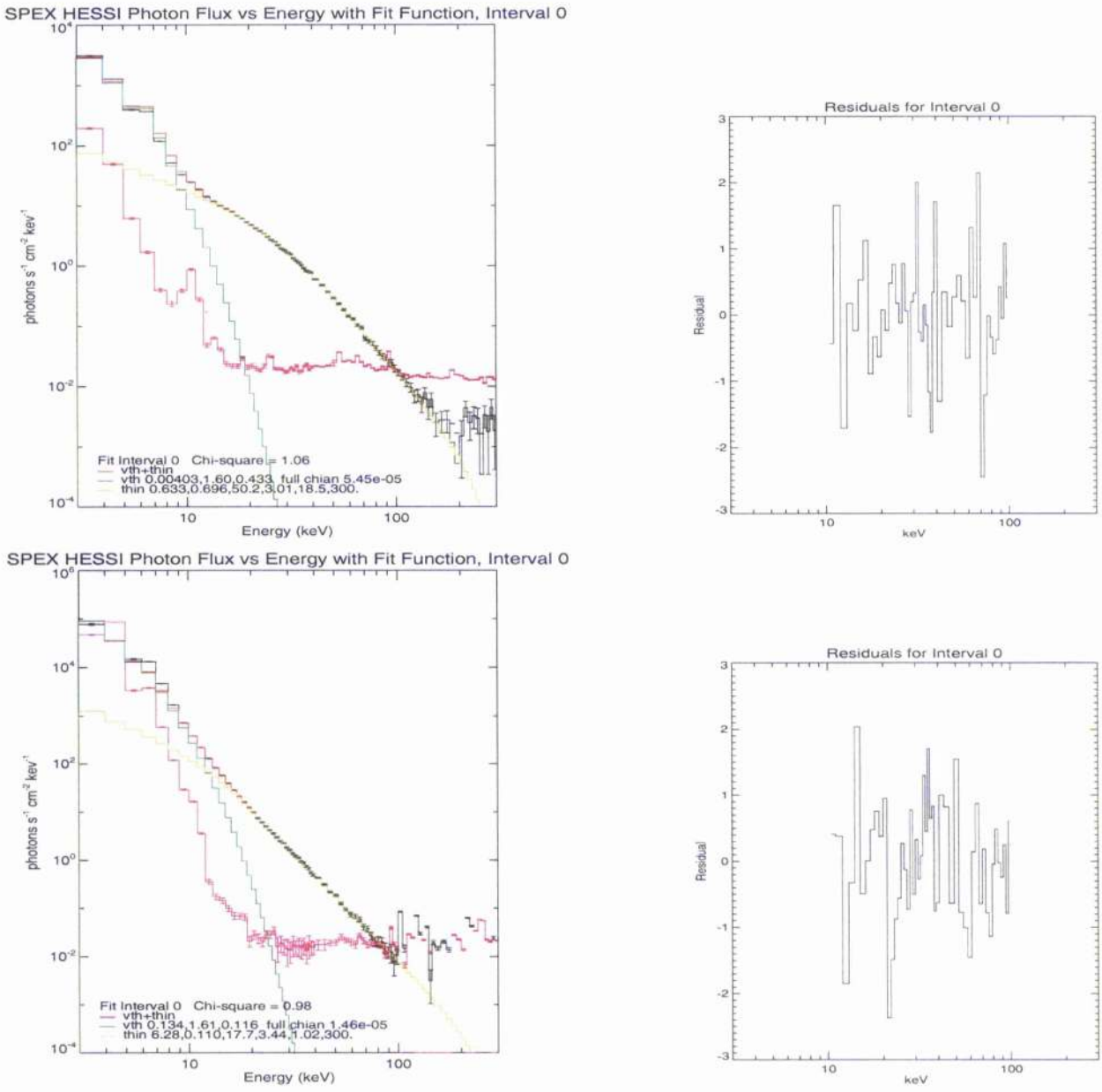

Figure 2.8: Photon flux spectra with functions fitted and residuals for 17^{th}Sept.2002 (*top two*) and 12^{th}April 2002 (*bottom two*) events.

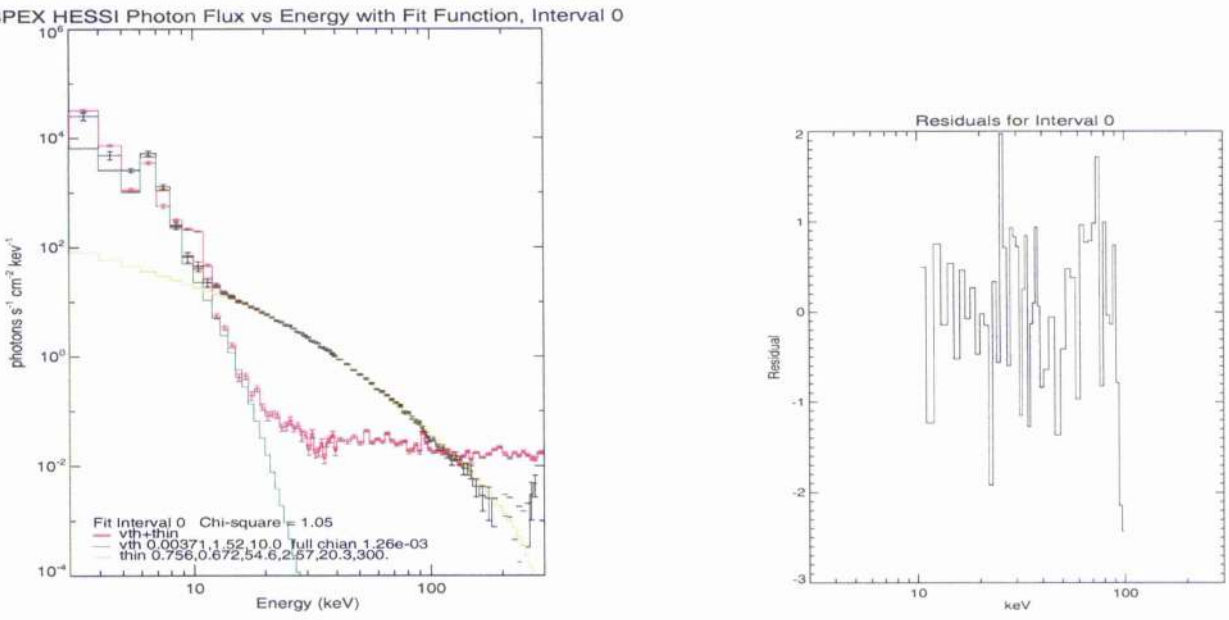

Figure 2.9: Photon flux spectra with functions fitted and residuals for 31^{st}Oct.2003.

The thin target bremsstrahlung function (yellow) is a double broken power law which combines with the thermal function to create the photon flux model (red) fitted in the photon energy range from 10 - 100 keV. The purple line is the background emission spectrum, which exceeds the photon flux spectrum (black) at higher energies. The signal will be useful so long as the purple line never exceeds the data.

2.1.8 Error Analysis

Statistical analysis of the errors can be done through generating histograms of the residuals of the fits, as shown in figure 2.10.

Figure 2.10 shows the distribution of the sizes of the normalized residuals for each event. For a good fit, the residuals should fit a Gaussian noise distribution. The standard deviation is evaluated as 0.493σ in 17/09/02, 0.905σ in 12/04/02 and 1.841σ in the 31/10/03 event. Within the fit range for all events we accumulate 82 count energy intervals (N). Hence, the standard error in the mean is $0.493\sigma/\sqrt{82}$=0.054σ for 17/09/02, 0.01σ for 12/04/02 and 0.203σ for 31/10/03. From figure 2.10 we see that the noise in the fit is not a exactly Gaussian in distribution which is in some respect would be too ideal. Also, the standard

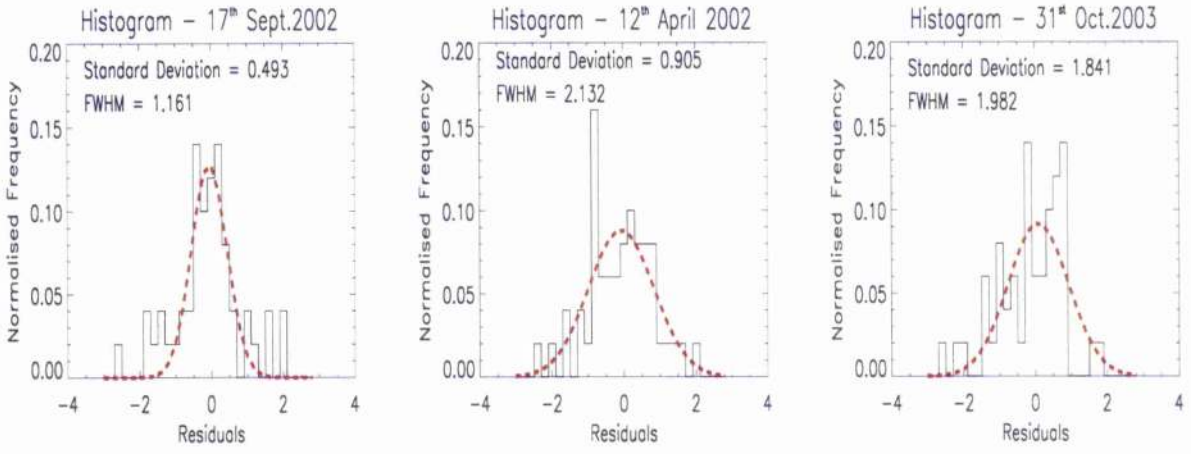

Figure 2.10: Histogram plots for the residuals of the fits for each flare event, 17^{th} Sept. 2002 (*Left*), 12^{th} April 2002 (*Centergoo*) and 31^{st} Oct.2003 (*Right*).

deviation of the normalized residuals is not 1.0 in any of the events, as expected, despite acceptable unsystematic residual distributions and χ^2 evaluations. The chi-square test only explicitly makes use of the mean and the variance of the residuals, neither of which would change if you randomly re-ordered the residuals. For these reasons, it should be stressed that the residuals having a Gaussian distribution, is not a sufficiently stringent test for goodness-of-fit. It is necessary to consider the distribution of the residuals with respect to energy ε. To do so we calculate the normalized cumulative residuals S(ε). This is found using the following expression

$$S(\varepsilon) = \frac{1}{N}\sum_{i=1}^{N} r_i. \tag{2.4}$$

Above, the quantity $S(\varepsilon)$ is the averaged (normalized) residual over the photon energy range, r_i is the i^{th} normalized residual corresponding to the photon energy (10+i) keV, and ε = (10+N)keV is the photon energy of the N^{th} residual. Figure 2.11 presents the normalized cumulative residuals for the fits of each event. Through this analysis we can see, for each event, the distribution of the residuals with respect to photon energy ε. This approach will assess the level of clustering of positive and/or negative residuals across the fitted energy range (Piana et al. 2003).

If the residuals were randomly distributed, S(ε) would exhibit a random walk with a stan-

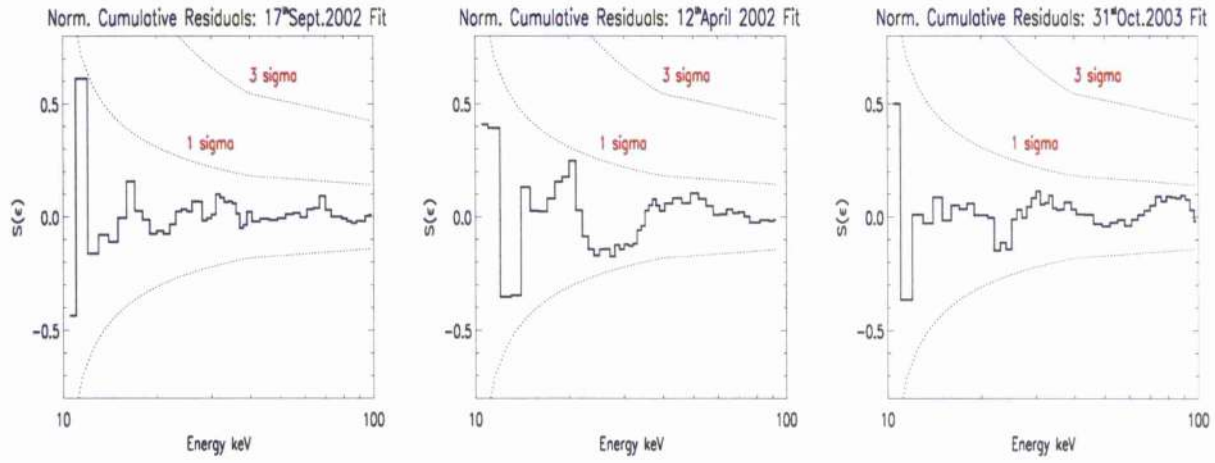

Figure 2.11: Normalized cumulative residuals of the fits for each flare event, 17^{th} Sept. 2002 (*Left*), 12^{th} April 2002 (*Center*) and 31^{st} Oct.2003 (*Right*).

dard deviation $\sigma = 1/\sqrt{N}$. It has been shown in figure 2.11 that the cumulative residuals of the fits lie within this 1σ level, which is very good. It has also been shown that the normalized residuals fluctuate evenly between the positive and negative in the photon energy range, in all events. If the deviation of residuals from zero is greater than this 1σ level then an unacceptable level of clustering of residuals exists and the parametric form of the fitted model would have to be rejected at the 99% confidence level, and adjusted for re-fitting. Hence, from figure 2.11 I can conclude that the residuals are statistically acceptable for the fits, and consistent with random data noise in each event. However, in order to uncover more detail in the models it would be necessary to increase the number of parameters, applied through the fit functions. Increasing the number of parameters may make it more difficult to get statistically acceptable residuals. In other words, the fit here is easily acceptable due to the small number of parameters for fitting, yet we may uncover more detail in the HXR spectrum by other methods, without losing fidelity in the residuals. Comparing residuals of the fits of the data with the models will be important when we want to compare between different methods.

Calculation of the errors in the HXR Spectrum :

The errors on the forward fitted photon flux spectrum can be derived from the errors on the count flux spectrum using the conversion factor. The standard approach to error

estimation [†] states that the error on a given energy bin/interval (i) is expressed as:

$$\sigma_{(\varepsilon_i)} = \sqrt{N_i}. \tag{2.5}$$

Above, N_i is the total counts in energy interval ε_i, $(C(\varepsilon_i))$. The total counts in any given energy bin is the sum of the number of observed counts and the background counts. This is expressed as:

$$C(\varepsilon_i) = C(\varepsilon_i)^{obs.} + C(\varepsilon_i)^{backg.} \tag{2.6}$$

The errors can be defined as $\sigma_{(\varepsilon_i)^{obs.}} = \sqrt{C(\varepsilon_i)^{obs.}}$ and $\sigma_{(\varepsilon_i)^{backg.}} = \sqrt{C(\varepsilon_i)^{backg.}}$, hence the error on the total counts for each bin/interval, $\Delta C(\varepsilon_i)$, is derived as:

$$\Delta C(\varepsilon_i) = \sqrt{(\sigma_{\varepsilon_i}^{obs.})^2 + (\sigma_{\varepsilon_i}^{backg.})^2} + \gamma_{systematic}. \tag{2.7}$$

$\gamma_{systematic}$ is the systematic uncertainty added in quadrature.
$\Delta C\varepsilon_i$ is compiled within the OSPEX software during the fit procedure. To convert between count flux errors and photon flux errors, $\Delta I(\varepsilon_i)$, the software uses the conversion factor relation, expressed in equation 2.8, giving:

$$\Delta I(\varepsilon_i) = \frac{\Delta C(\varepsilon_i)}{\texttt{Conversion Factor}} \tag{2.8}$$

The error spectra have been plotted along with the solution on the forward fitted HXR spectrum, along with the photon flux models for each event, for comparison. Results for each event are presented in figure 2.12.

The signal to noise ratio is critical when choosing suitable energy binning in spectroscopy. The signal to noise ratio determines the error ratio in the energy bins for each of the events, presented in figure 2.12. All energy intervals here have statistical uncertainties on their measured counts, and subsequently on their photon flux. In general, for any flare event small energy bin intervals of 1 keV worsen the signal to noise ratio at higher energies, increasing the noise in the fit residuals. To see this, consider a large flare event with N total counts

[†] errors determined from Poisson Distribution standard deviation.

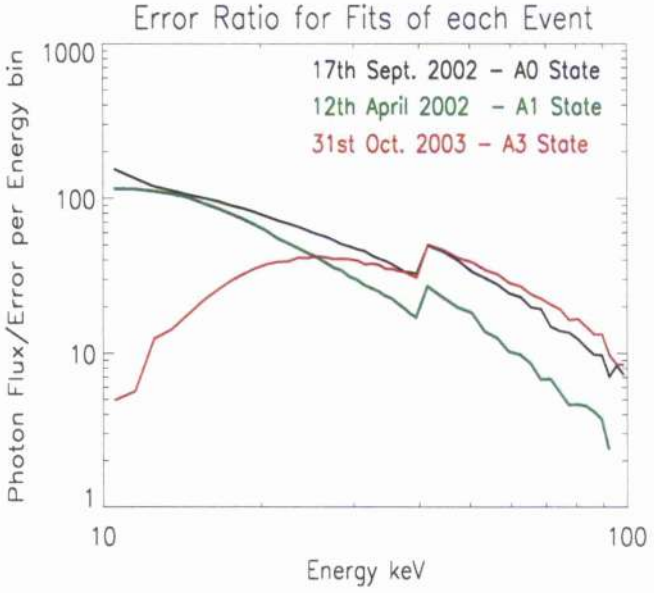

Figure 2.12: The error ratios for each event.

in an energy range from 10 to 100 keV. If we we divide the energy range into x equal bin intervals we have approx $\frac{N}{x}$ counts per bin. The fractional error on each bin can be expressed as:

$$\sigma = \frac{\sqrt{\frac{N}{x}}}{\frac{N}{x}} = \sqrt{x}\frac{\sqrt{N}}{N} \tag{2.9}$$

From this expression, we see that $\sigma \to \infty$ as $x \to \infty$. In other words, the energy bin size decreases, as the error increases. This is why we used uneven energy binning.

The jump in the error ratio at 40 keV, evident in figure 2.12 signifies reduced errors, since the error ratio becomes larger until 100 keV. The jump coincides with a change of energy binning in the fits i.e. from 1 keV to 3 keV bins, at the 40 keV interval. Increasing the bin size has improved the signal to noise ratio through reducing the errors. The signal to noise ratio is very poor in the 31/10/03 event from 10 keV up until 25-30 keV, with large errors per energy bin. This is a direct result of the thick shutter attenuators. The background emission is responsible for the increased errors and worsened signal to noise ratio in the 12/04/02 event from 25-100 keV. The signal to noise ratio will increase for low count rates, as can be seen for the 31/10/03 event.

2.2 Mean Electron Distribution Spectra by Forward Fitting

With an acceptable photon flux spectrum we can next consider the best fit mean electron distribution for the parametric forms of the thermal and non-thermal fit functions of each event, as outlined in table 2.3. The fit to the photon flux spectrum provides the parametric solution we are seeking i.e. $\bar{F}(E)$. The results of the best fit parametric form of the mean electron flux spectrum of each event are shown on figure 2.13.

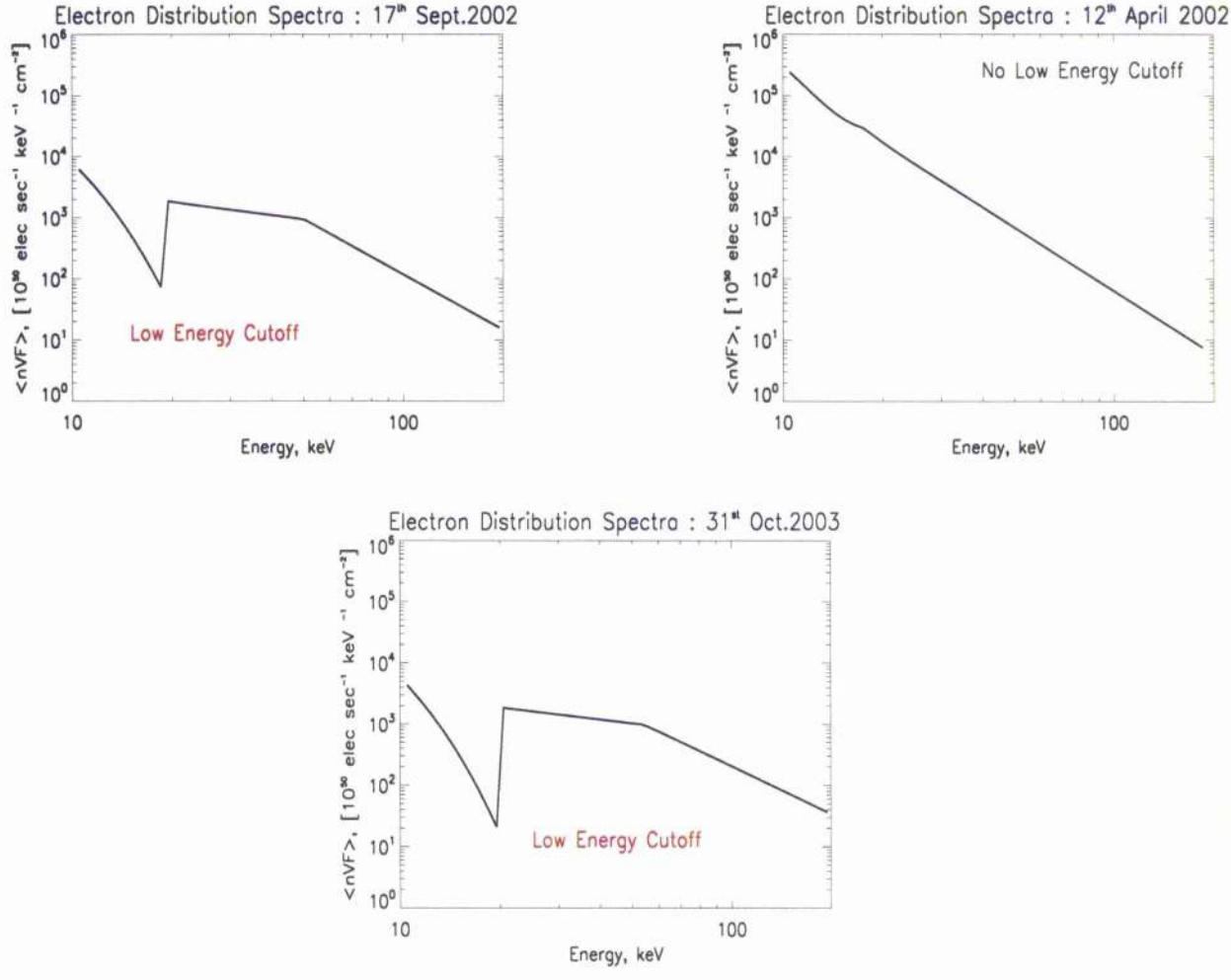

Figure 2.13: Best fit electron distribution spectra models by forward fitting for 17^{th}Sept.2002 (*top left*), 12^{th}Oct.2002 (*top right*) and 31^{st}*Oct.*2003 (*bottom*) events.

From the table of parameters in figure 2.3 we see that parameter 8 is the low energy cutoff in the electron distribution function. The value of this low energy cutoff is within the

fit energy range for 17/09/02 and 31/10/03, at approx. 20 keV in both cases. A statistically acceptable fit ($\chi^2 \approx 1.00$) was found for all events, but an acceptable fit with low energy cutoff could not be found in the 12/04/02 event. Forward fitting presents a model interpretation of mean electron flux spectrum with a limited number of basic features, such as low energy cutoff and break energy, as seen from figure 2.3. The electron distribution spectrum of non-thermal electrons must have a low energy cutoff, due to their power law distribution, which would otherwise extend indefinitely. A low energy cutoff can allow us to distinguish between thermal and non-thermal electrons and keeps the number of non-thermal electrons within a finite range. When we observe the fitted HXR spectrum for the 17^{th} Sept. 2002 and 31^{st} Oct. 2003 events in figure 2.9 there is indeed greater flattening of the photon model at lower hard X-ray energies when compared with the HXR spectrum for 12/04/02. This proves that given knowledge of the HXR spectrum we can infer information on the corresponding mean electron distribution in flares. The limited number of features in the best fit electron models is a consequence of the limited number of parameters in the fit functions, making forward fitting disadvantageous for anyone wanting to infer detail in flare electron dynamics.

Controversially, figure 2.14 shows that no low energy cutoff features in the electron distributions for the 17^{th} Sept. 2002 and 31^{st} Oct. 2003 events is an equally likely scenario. The statistical accuracy in the fits is just as acceptable for no low energy cutoff featured model as it is with a low energy cutoff featured model. The corresponding HXR spectrum, χ^2 result, errors, normalized residuals and cumulative residuals are presented below the electron models for these events.

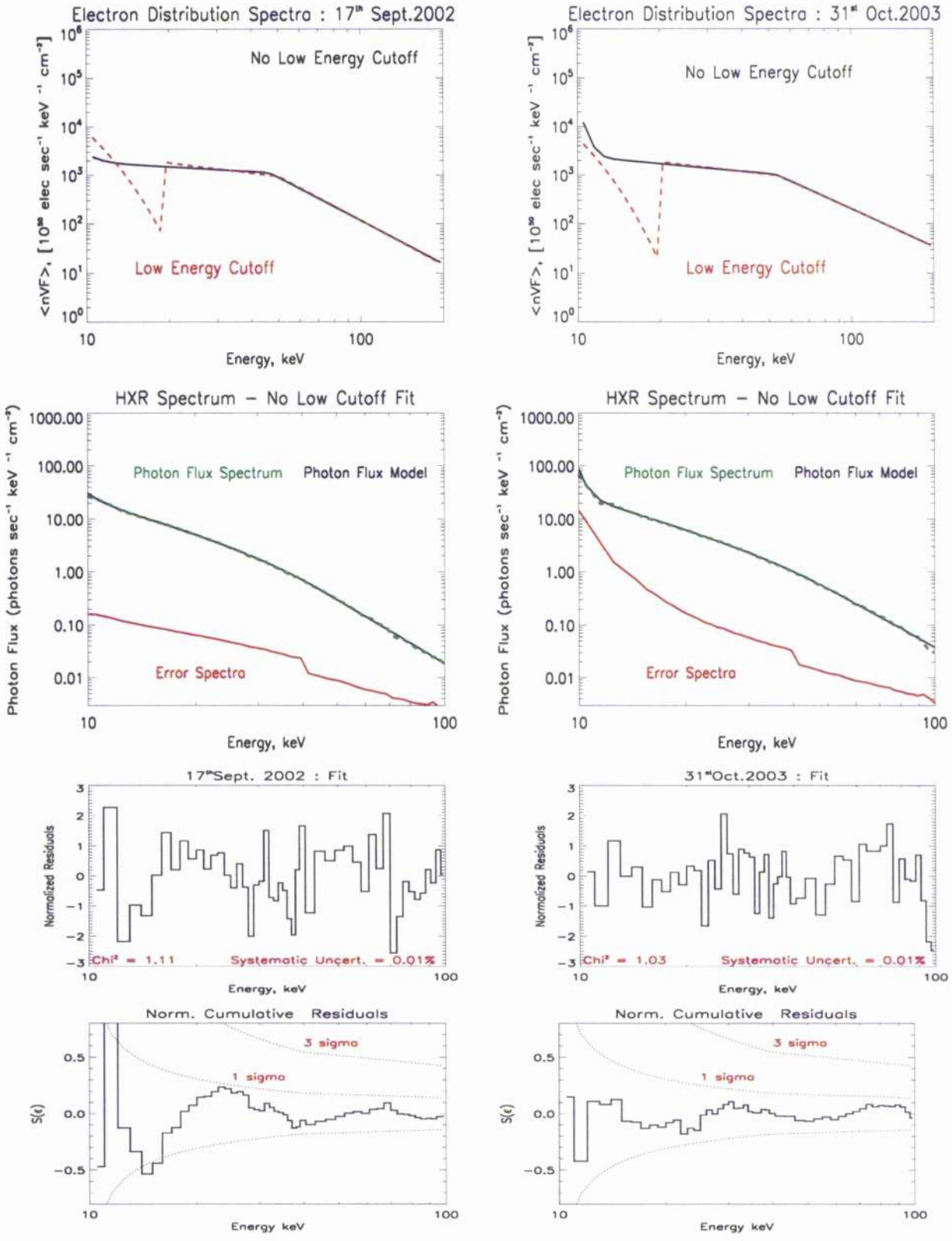

Figure 2.14: No low and low energy cutoff by forward fitting for 17^{th}Sept.2002 (*Left Column*) and 31^{st}Oct.2003 (*Right Column*) events.

The fits for HXR spectra for the two events presented in figure 2.14, present very acceptable χ^2 values (see results on figure). As well as this, residuals are non-systematic (do not fluctuate between positive and negative values across the energy range) and are reduced (generally quite small). The cumulative residuals are within $\pm 1\sigma$ confidence level. To ensure no low energy cutoff in the fitting procedure we change its parameter value so that it lies outside the 10-100 keV (HXR) fit range and will not feature in the resulting electron distribution spectrum. Hence, the new low energy cutoff parameter for fits of the 17/09/02 and 31/10/03 events are presented in Table 2.4.

Parameter	Min.	Max.	$17^{th} Sept.'02$	$31^{st} Oct.'03$
Low Energy Cutoff	1.00	9.00	7.889	4.226

Table 2.4: Low energy cutoff parameter values assigned for 17^{th} Sept. 2002 and 31^{st} October 2003.

The other parameter values have changed also to suit the new fit. However, the important point here is that the low energy cutoff parameter has been deliberately excluded in the fits presented in figure 2.14 to show that two equally acceptable forward fit solutions are possible. The two solutions present different features in the returned electron distribution models, making it difficult to establish which solution is real and which is not.

2.2.1 Conclusions on the Forward Fitting technique

In this chapter, we presented the results for the HXR photon flux spectra and corresponding best fit electron distributions of three interesting flare events using a forward fitting technique. Through spectral analysis we found that the extracted photon flux spectrum is a model dependent approximation of the true photon flux spectrum. With forward fitting, the HXR spectrum is deemed acceptable within the limits of the errors and integrity of the residuals, after refinement of the count flux spectrum due to background noise and emission. The conversion factor for determining photons from counts in the photon energy range is fundamentally an approximation of the DRM and is unrecovered in the presence of attenuators. Despite this, the corresponding best fit electron distribution can still recover certain characteristic features such as the low energy cutoff. Yet, I have shown that equally accept-

able fits can be achieved without including certain features such as the low energy cutoff, as done for the 17^{th} Sept. 2002 and 31^{st} Oct. 2003 events. This result makes it difficult to determine which forward fitted result for the mean electron flux distribution is correct, thus, highlighting a major failing of the forward fitting technique. We must consider model independent calculations to more accurately evaluate the true forms of the HXR and mean electron distributions, rather than approximations (conversion factors) with forward fitting. Direct inversions of the relevant integrals is a logical alternative to forward fitting and must be considered to determine whether or not an improvement in the recovered HXR spectrum and mean electron distributions is possible.

Chapter 3

Direct Inversion Approach

"Why are there errors !? .. Programs should be forced to run regardless !"

Office roommate

3.1 Direct Inversion Calculations

As an alternative to forward fitting of hard X-ray spectra derived from measured count flux spectra, direct inversion addresses the problem through solution of a linear system of equations, rather than approximations with a model. Direct calculation of photons from counts, is a more logical approach for solving the problem analytically, and does not require forward fitting of the data with any parametric models. For this reason, direct inversion calculations provide a model independent approach to solving for photons. In this chapter I will address the problem of deducing the photon flux spectrum from the measured count flux spectrum, as the discretized matrix transform of equation 1.22.

The DRM :

Equation 1.22 states that the data function $C(\varepsilon)$, is contributed to by all the values of the source function $I(\varepsilon)$, using the DRM which is an array of probability distribution functions for converting from photons to counts for each photon energy in the photon energy range (Craig & Brown, 1986). Consider the source function in the energy range ε_{min} to ε_{max}, with

bin width intervals $\delta\varepsilon_i$. The expression for the data function in equation 1.22 integrates over the energy range of the source function spectrum, accumulating the finite column area bounded by the energy bin intervals. Hence, the equation can be expressed as a summation over the energy interval of the source function spectrum, giving

$$C(\varepsilon_i) = \sum_j \mathtt{DRM_{ij}} \cdot I(\varepsilon_j), \tag{3.1}$$

$\mathtt{DRM_{ij}}$ in equation 3.1 corresponds to element (i,j) in the DRM array which has dimensions of N×M elements. The DRM is represented as a matrix with dimensions of N count energy intervals (number of DRM columns), and M photon energy intervals (number of DRM rows). The number of counts of count energy ε_i is found through matrix multiplying all the DRM array column elements (j) in that i^{th} row with the photon data at all photon energies. In terms of matrices, equation 1.22 is

$$\begin{bmatrix} C(\varepsilon_1) \\ C(\varepsilon_2) \\ C(\varepsilon_3) \\ \vdots \end{bmatrix} = \begin{bmatrix} a_{11} & a_{21} & \cdots & a_{N1} \\ a_{12} & a_{22} & \cdots & a_{N2} \\ \vdots & \vdots & \ddots & \vdots \\ a_{1M} & a_{2M} & \cdots & a_{NM} \end{bmatrix} \cdot \begin{bmatrix} I(\varepsilon_1) \\ I(\varepsilon_2) \\ I(\varepsilon_3) \\ \vdots \end{bmatrix} \tag{3.2}$$

(3.3)

Here, $N < M$. For example

$$[C(\varepsilon_1)] = [a_{11}\, I(\varepsilon_1) + a_{2:}\, I(\varepsilon_2) + + a_{N1}\, I(\varepsilon_N)] \tag{3.4}$$

Each a_{ij} element in the DRM is the probability that a photon with given energy ε_j is detected as a count of energy ε_i. The rows of the DRM for each energy interval (in count space) are essentially probability distribution functions used by the detectors as a response to a photon with photon energy, ε_j. Hence, allowing us to evaluate photons in photon energy space in terms of measured counts in count energy space. In other words, at each element in the DRM array denoted by $\mathtt{DRM}_{ij}$ we have a probability to convert a photon of energy (ε_j)

to a count of energy (ε_i). The diagonal terms of this matrix represent the probability that a photon with given energy produces a count of the same energy. However, there is a finite probability that a photon of any energy gets redistributed as a count of any energy. This redistribution can be seen graphically on figure 3.1.

In practice, when converting from counts to photons the DRM configuration used by the detectors depends on the attenuator state in position. The difference between the DRM configurations is presented in figure 3.1.

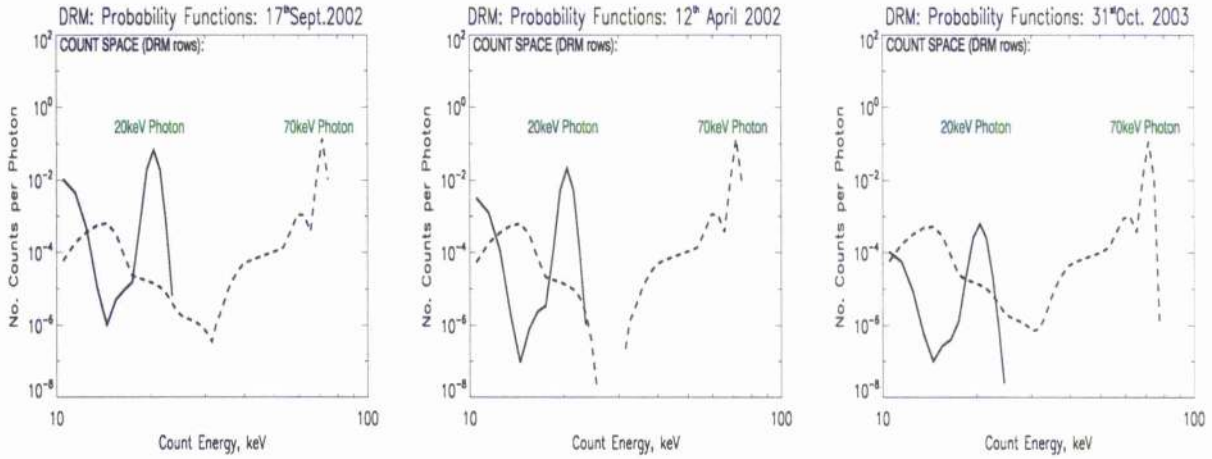

Figure 3.1: DRM probability distribution functions for attenuator state - A0 (*left*), attenuator state - A1 (*center*) and attenuator state - A3 (*right*), which are applicable to each of the events respectively. Solid lines for each event is the probability for conversion of a photon with energy 20keV to a count of certain energy. The 70keV photon distribution is marked by the dashed line in each event.

The solid line for each event in figure 3.1 presents a probability that should not extend beyond 20 keV since a 20 keV incident photon, in theory, can only be recorded with a count energy equal to or less than the photon energy of 20 keV. Hence, a perfect detector would have presented a straight vertical line at 20 keV (delta-function) with count per photon ratio of exactly 1. In reality this is not possible. So for the 20 keV photon in each event, and likewise for the 70 keV photon, the probability distributions exhibit what appears like a point spread function characteristics at 20 and 70 keV count energiesi.e. with part of the distribution extending slightly beyond 20 and 70 keV respectively. This is a primarily due to inefficiency in the calibration of the DRM.

In certain cases there is a probability that the detectors responds to, say, a 20 keV photon by interpreting it as two 10 keV photons. For example, the 70 keV photon distribution in all events in figure 3.1 appears to have another peak consistently around a count energy of 15 keV. The reason for this peak may be because of another peak at approx. 55 keV in the same distribution i.e. 55 keV + 15 keV = 70 keV, which was intended. Thus, reiterating the point made regarding the possibility of a photon being registered as multiple photons of lower energies which can be summed to equal the energy of the actual photon. Notice also that the probability of registering a 20 keV photon becomes significantly worse with increasing attenuator state. The probability curve for the 70 keV photon (dashed lines) remains unchanged in each event. This highlights the fact that the deterioration in the solid lines at lower energies must be due to the attenuators. For hard X-rays, approaching 100 keV, the general trend from all three plots in figure 3.1 shows that it is more probable that photons will be recorded with their true energy rather than a lower energy. The efficiency of the detectors is highest around 100 keV. In theory the perfect DRM array would be represented by an identity matrix. The semi-calibrated DRM takes only the diagonal elements of the response matrix. Clearly, the response matrices are much more complex and using purely the diagonal elements severely restricts the accuracy in the recovered HXR spectrum.

The Inverted DRM :

Hard X-ray spectra can be inferred using a direct calculation of $I(\varepsilon)$ from $C(\varepsilon)$ using the inverted DRM, DRM^{-1}. In order to calculate the DRM^{-1} from the DRM, we must truncate the DRM array so that the number of photon intervals (M) is reduced to equal the number of count energy intervals (N) i.e. for matrix inversion the DRM array must be square (N=M). Then

$$\mathrm{DRM}^{-1} \cdot C(\varepsilon) = \mathrm{DRM}^{-1} \cdot \mathrm{DRM} \cdot \mathrm{I}(\varepsilon) \tag{3.5}$$

$$\mathrm{DRM}^{-1} \cdot C(\varepsilon) = I(\varepsilon) \tag{3.6}$$

The inverted DRM, like the DRM is a 2-dimensional array with dimensions in count energy space and photon energy space. The rows now represent the probability distributions for the number of photons per keV per count. The expression for calculating the photon flux from count flux is written in discretised matrix format as

$$\begin{bmatrix} a_{11} & a_{21} & \cdots & a_{N1} \\ a_{12} & a_{22} & \cdots & a_{N2} \\ \vdots & \vdots & \ddots & \vdots \\ a_{1N} & a_{2N} & \cdots & a_{NN} \end{bmatrix}^{-1} \cdot \begin{bmatrix} C(\varepsilon_1) \\ C(\varepsilon_2) \\ \vdots \\ C(\varepsilon_N) \end{bmatrix} = \begin{bmatrix} I(\varepsilon_1) \\ I(\varepsilon_2) \\ \vdots \\ I(\varepsilon_N) \end{bmatrix} \tag{3.7}$$

(3.8)

where $N = M$.

Since we have 82 count energy bins for each event with varying energy binning in the energy range 10-300 keV, there are 92 photon energy bins but with energy range 10-600 keV. This is because there is a probability that a photon of 600 keV can be recorded as a two counts of 300 keV and the energy range of possible photon energies will always be greater than the count energy range. Consequently the DRM has array dimensions of 82×92. In order to invert the DRM we must truncate it and remove the last 10 photon energy distributions creating 82 photon energy intervals. The invertable DRM array must be square with dimensions 82×82. The implications of this will be explored later. Figure 3.2 show the probability distributions for conversion to photons for a count with energy of 20 keV and 70 keV.

Figure 3.2 presents a similar trend for the 70 keV photons, as with the 70 keV counts from figure 3.1, i.e. no change in the probability distribution with increasing attenuation from A0 to A1 to A3. The difference with figure 3.1, is that the negativity in the inverted DRM functions for both the 20 keV and 70 keV counts means that a logarithmic y-axis cannot be used to show detail in the functions at very low photons per count. This negativity will also have significant consequences on the returned HXR spectrum particularly in 31^{st} Oct.

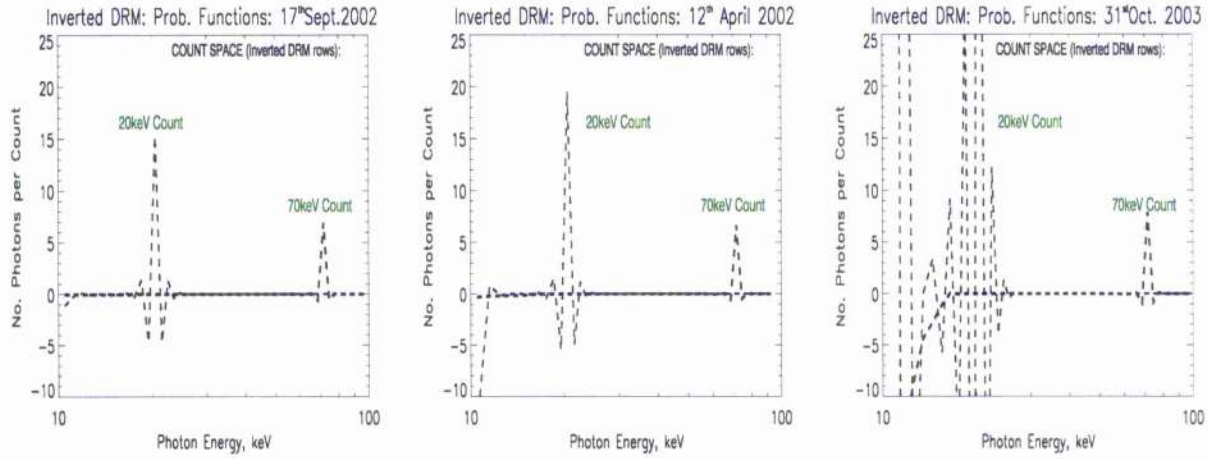

Figure 3.2: Inverted DRM probability distribution functions for atenuator state - A0 (*left*), attenuator state - A1 (*center*) and attenuator state - A3 (*right*), again applicable to each event respectively.

2003 event. The most notable similarity between figure 3.2 and 3.1 is the change in the probability distribution for the 20 keV photon for each attenuator state. The significant increase in the noise and instability of the DRM, amplified through inversion, is clear for the 20 keV photon in A3 attenuator state ans less so for A0 state. For the A3 state the inverted DRM is severely distorted for low energies, in the range of the attenuator impact, with massive fluctuations in both the positive and negative axis.

3.2 The Inversion Problem

There is a significant weakness with the direct inversion approach which can be highlighted in the context of the selected flares. There is also an interesting connection with the attenuator state of the detector during certain flare impulsive phases which will be presented here.

The weakness in this calculation is a result of the non-diagonal nature of the DRM array, creating an ill-posed inverse problem. The inversion is ill-posed in the sense that small changes in the data can give rise to large changes in the solution for the inverted DRM. Inversion presents noise amplification due to inescapable sources of error compounded by the nature of the measurement itself and furthermore from systematic instrumental effects. The severity of this instability is so great that the gain in information on the source function

is small even for large improvements in the data accuracy (Craig & Brown, 1986).

Off-axis elements in the DRM represent the probability that photons are redistributed to another energy. For harder X-rays, more photons are recorded with their true energy than at lower energy, but above 100 keV this is reversed. Consequently, photons of higher energies can be registered as counts of a lower energy. Subsequently, we get a non-diagonal array of photon energies with respect to count energies in the DRM. Figure 3.3 (*Left*) presents the full DRM for the count energy range of the selected flares (10-300 keV).

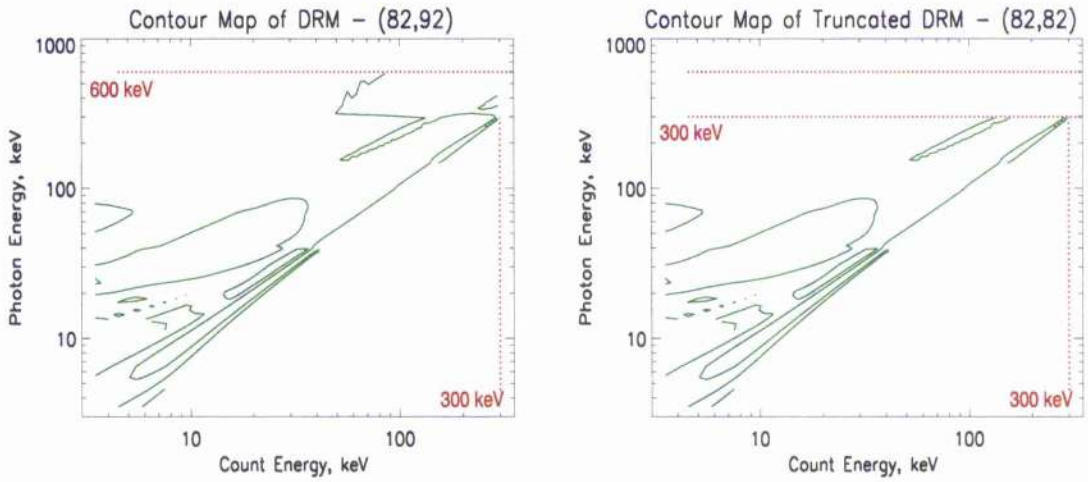

Figure 3.3: Contour map of the full DRM for count energies (6-300 keV) (x-axis) with respect to photon energies (y-axis) for 17^{th}Sept.2002 event (*Left*). Effect of truncation of the DRM (*Right*).

The count energy range of 10-300 keV corresponds to a photon energy range of 10-600 keV as can be seen on figure 3.3. The lower triangular region of this contour map exhibits insignificant counts per photon response, as is also the case with the full RHESSI response image in figure 1.10. From figure 3.3 (*Right*) it is clear that truncation of the DRM completely removes part of the observed photons energies. To meet the requirements of inversion, we must truncate from 300 keV to 600 keV photon distributions, thus removing some information on higher energy photons. There are 6 contour levels describing the DRM array structure. It is clear that the higher values (contours) tend to lie along the matrix diagonal elements. This is expected since the probability for conversion from photon energies

to count energies should be one to one eg. a 50 keV photon should most likely result in a 50 keV recorded count, as previously discussed.

3.3 Error Analysis with Direct Inversion

In our error analysis of direct inversion calculations we determine the Poisson errors for photon flux spectra, using the same approach as with forward fitting. For direct inversion the error in the photon flux is the matrix product of the inverted DRM and count flux errors, $\Delta C(\varepsilon_i)$. Errors in the photon flux spectra $\Delta I(\varepsilon_i)$ by direct inversion are therefore expressed as

$$\Delta I(\varepsilon) = \mathrm{DRM}^{-1} \cdot \Delta \mathrm{C}(\varepsilon). \tag{3.9}$$

From equation 2.6 the error in the count flux $\Delta C(\varepsilon)$ is the square root of the sum of the measured errors in the observed and background count flux. Similarly, the errors on the photon flux of a given energy, are the square root of the cumulative square errors on the count flux at all energies, multiplied by the matrix probability function of the response to that photon. Hence, this calculation is expressed as:

$$\Rightarrow \Delta I(\varepsilon_i) = \sqrt{\sum_{j=i}^{N} \left[\mathrm{DRM}^{-1}_{ij} \cdot \Delta \mathrm{C}(\varepsilon_j)\right]^2} \tag{3.10}$$

Equation 3.10 tells us that the errors in all the photon energy bins are accumulated from this expression. The error ratio is calculated using the following expression:

$$\mathtt{Photon\ Flux\ error\ ratio} = \frac{\mathrm{I}(\varepsilon)}{\Delta \mathrm{I}(\varepsilon)} \tag{3.11}$$

As with forward fitting the error ratios reflect the general trend of the signal to noise ratio. The results for hard X-ray spectra by direct inversion along with their errors are presented on figure 3.4.

Direct inversion calculations for the HXR spectra for the 17^{th} Sept. 2002 and 12^{th} April 2002 events show degrading effects due to the ill-posed inversion, with instability in the

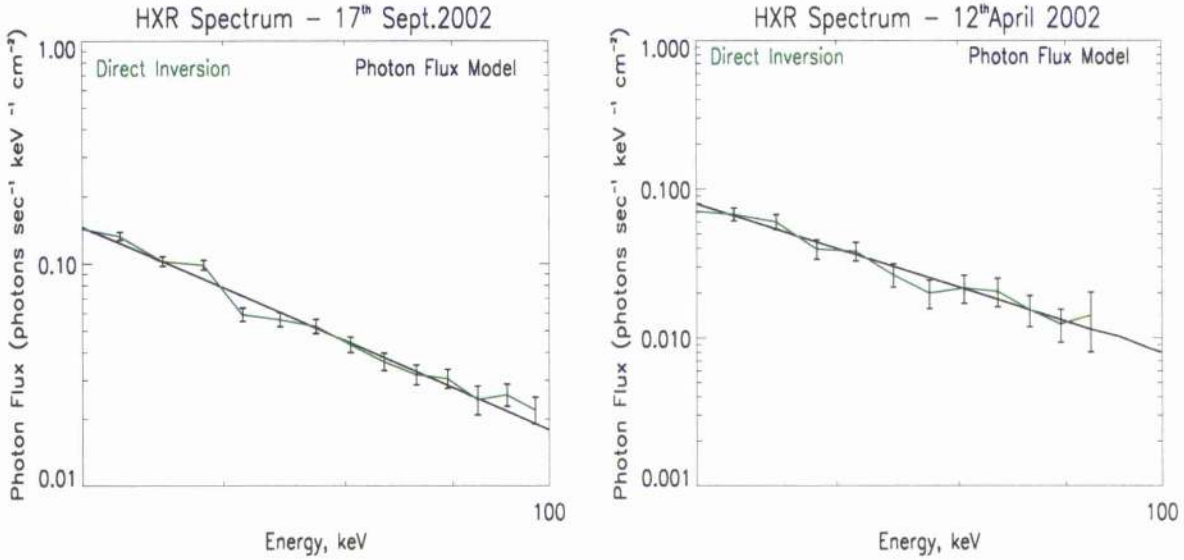

Figure 3.4: Direct Inversion HXR Spectra for 17^{th}Sept. 2002 (*Left*) and 12^{th}April.2002 (*Right*) within energy range 60-100 keV for purposes of highlighting instability in recovered HXR spectra.

solution. Noise amplification is evident to some degree in both events, moreso in 12^{th} April. 2002 where negativity (noise) in the solution is evident at >90 keV. This degradation in this event is most likely due to the influence of the thin shutter attenuators, compared with 17^{th} Sept. 2002 event which has no shutter influence upon the DRM. The instability in 31^{st} Oct. 2003 is much greater as is clearly demonstrated in figure 3.3 in the 10-30 keV energy range.

Noise in the returned solution is evident at lower energies which fall under the influence of the thick shutter attenuators. The effect of the thick shutter attenuators diminishes the signal and presents a severe lack of sensitivity in the DRM array probability distributions. Deterioration and noise amplification in the HXR solutions resulting from increasing attenuation on the DRM configuration is analogous with the result for the conversion factors shown in figure 2.6. Until 40 keV, conversion factors severely degraded in the A3 state compared with A1 and A0 states. The conversion factors are approximations of the DRM and so the result in the direct inversion solution for A3 shows significant degradation compared with A1 and A0 state solutions, in the 10-40 keV range.

We can also compare forward fitting and direct inversion through their residuals. This is presented in figure 3.6.

The residuals for direct inversion are calculated as follows

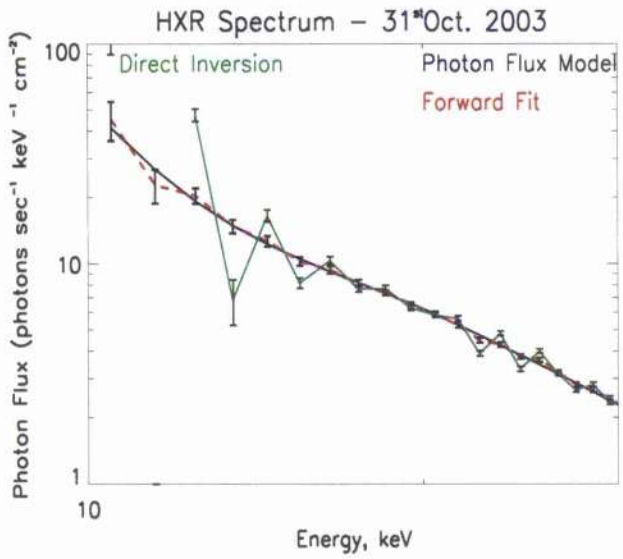

Figure 3.5: HXR spectrum for 31^{st} Oct. 2003 event in the 10 - 30 keV energy range. Comparing direct inversion and forward fitting with the photon flux model.

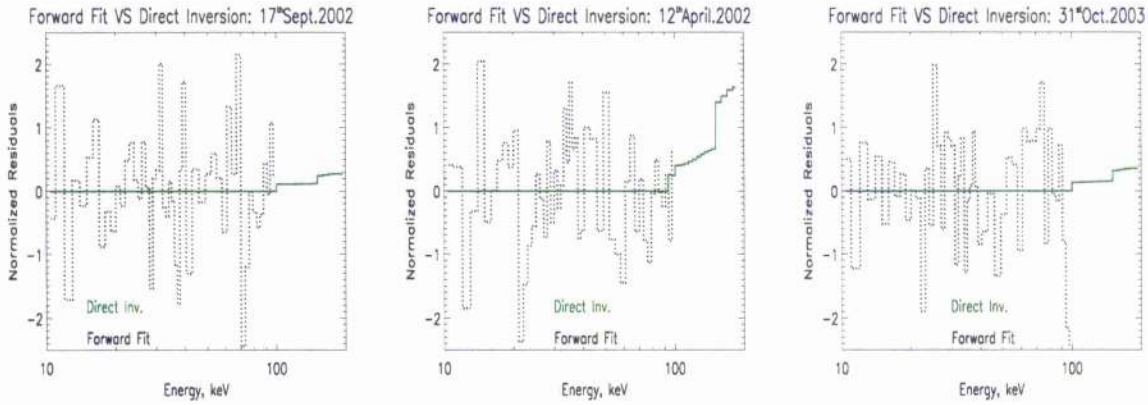

Figure 3.6: Residuals for direct inversion compared with forward fitting for each event.

$$R_{direct} = \frac{C_{true}(\varepsilon) - C_{direct}(\varepsilon)}{\sigma(\varepsilon)} \tag{3.12}$$

$C_{true}(\varepsilon)$ is the true count flux spectrum as measured with RHESSI. It is clear that within the fit range the counts from direct inversion from photons, using the truncated DRM, should be identical to the true count flux. For this reason the residuals are zero up to 100 keV, which is the upper energy value of the fit range. However, the residuals for energies greater than 100 keV are positive in all events and result from the true count flux calculated from photons using the full DRM i.e. not truncated. The residuals at these higher energies signify the

truncation region elements of the DRM array. The instability brought about by the ill-posed inversion is further emphasized here by the fact that the residuals are indeed zero within the fit energy range, but the solution for the HXR spectra is far from stable and clearly will not show zero in the residuals, as would be expected.

3.3.1 Conclusions on Direct Inversion

Negative photon flux and noise amplification in the HXR spectrum is a consequence of the low flux levels combined with instability in the inverted DRM configuration. The attenuators substantially diminish the photon flux for lower energies. This is more apparent in the 31^{st} Oct. 2003 event with A3 attenuator state, and least of all in the 17^{th} Sept. 2002 event with A0 attenuator state. Direct inversion presents unsatisfactory solutions in the HXR spectrum, compared with a forward fitting approach, resulting in a continued lack of smoothness and other un-physical ramifications. The results for direct inversion here agree with the literature (Craig & Brown, 1986), and must be deemed useless due to their instability in recovering the full photon flux spectrum. Such problems of noise in determining photons from the count flux spectrum can be suppressed by employing a regularized inversion technique which introduces physical constraints and smoothing upon the inversion solution. This approach will be taken further and used for inferring mean electron distributions from photons.

Chapter 4

Generalized Regularized Inversion Technique

Our goal is to return high resolution photon flux spectra from count flux space, and further more mean electron distribution spectra from HXR spectra, in a way which is complimented by effective suppression of noise induced un-physical behaviour. Even the most accurate photon spectra are contaminated by noise, which becomes amplified when continuing to infer the electron flux spectrum. By making a prior assumption of smoothness and inverting the data set spectrum with a Tikhonov regularization algorithm (Tikhonov, 1963), we can infer reliably such features in the source spectrum as the data allow. Every experimental problem described by equation 1.9 is affected by numerical pathology termed ill-conditioning, such that the unconstrained solution for the source function is contaminated with measurement noise amplification reflected through unphysical oscillations in the constructed source function, as seen with direct inversion. To stabilize the inversion problem, extra information is introduced by way of a smoothness condition on the source function.

Thompson et al. (1992) first applied regularization to high resolution solar HXR spectra and showed that regularization produced the best overall solution rather than obtaining a solution with a specified resolution or noise level. Johns and Lin (1992) practised regularization through coarse energy binning to maintain good statistical accuracy. Regularized inversion of the integral equation relating photons to electrons was then employed by Piana

et al. 1994, 2003; Piana and Brown, 1998. A regularization algorithm was later applied by Piana et al., 2003 with singular value decomposition (SVD). Piana et al., 2003 applied zero order regularized inversion and recovered real features in the mean electron distribution spectrum, such as local minima, for the 23^{rd} July 2002 RHESSI event which was not realizable by Holman et al., 2003 in their limited parameter forward fitting approach.

Tikhonov regularized inversion directly solves the minimization problem relating the data set (count flux spectrum) to the expected photon flux model. In applying the regularization algorithm the linear Volterra integral from equation 1.9 can be expressed in discretized matrix format given in equation 1.20. Likewise, the counts to photons relation has been written in matrix format in equation 1.22. We can summarize these relations in a general equation for relating any source function g to the data function $\bar{\mathbf{F}}$ using a kernel function $\mathbf{A}$, given by

$$\mathbf{g} = \mathbf{A}\,\bar{\mathbf{F}}. \tag{4.1}$$

So we can express equation 1.9 in the form

$$(\mathbf{A}\,\bar{\mathbf{F}})(\varepsilon) = \frac{1}{4\pi\,R^2} nV \int_{\varepsilon}^{\infty} \bar{F}(E)\sigma_b(\varepsilon, E)\,dE \tag{4.2}$$

$\mathbf{g}$ is an M-vector, $\mathbf{A}$ is the $M \times N$ matrix representing the bremsstrahlung cross-section, $\bar{\mathbf{F}}$ is the N-vector representing the mean electron spectrum, $\bar{F}(E)$, in this case. A general expression for $\mathbf{A}$ is given as:

$$\mathbf{A}_{ij} = \frac{\bar{n}V}{4\pi\,R^2} Q_b((\varepsilon_{i+1} + \varepsilon_i)/2, (E_{j+1} + E_j)/2)\delta E_j, \tag{4.3}$$

$$i = 1, ..., N \; j = 1, ..., M \geq N \tag{4.4}$$

Since $M > N$ there is no unique solution of the linear integral system. Tikhonov regularization seeks the smoothest solution using a least squares minimization algorithm relating the data and source spectra. Generalized regularization for all orders of regularization solves

this problem described by

$$\mathcal{L}(\bar{\mathbf{F}}) \equiv || \mathbf{A}.\bar{\mathbf{F}} - \mathbf{g} ||^2 = \texttt{Minimum} \tag{4.5}$$

Here the double bars (||..||) denote the Euclidean norm of a vector (Bertero, De Mol and Pike, 1985).

Generalized regularized inversion incorporates a GSVD (Generalized Singular Value Decomposition). Physical constraints consist of properties which are to be conserved or to be minimized/maximized, such as $||\bar{\mathbf{F}}|| = \texttt{min.}$, at all times. Generalized regularized inversion will apply such physical constraints to the least squares minimization problem which solves for the source spectrum. Kontar et al. (2004) have shown how to recover mean source electron spectra $\bar{F}(E)$ in solar flares through physical constraint regularization analysis of the bremsstrahlung photon spectrum $I(\varepsilon)$. Kontar et al. (2005) applied such generalized regularization techniques with GSVD to RHESSI data from a solar flare observed on 26^{th} February 2002.

Applying physical constraints to the Minimization problem :

The physical quantity $\bar{\mathbf{F}}$ must satisfy various physical conditions such as $\bar{\mathbf{F}} \geq 0$ and any known constraints such as properties to be conserved or minimized/maximized.

The general expression, given the constraint operator, states that the minimization problem from equation 4.5 can be rewritten as:

$$\mathcal{L}(\bar{\mathbf{F}}) \equiv || \mathbf{A}\bar{\mathbf{F}} - \mathbf{g} |^2 + \lambda || \mathbf{L}\bar{\mathbf{F}} ||^2 = \texttt{Minimum} \tag{4.6}$$

The regularization parameter λ, in equation 4.6 tunes the trade-off between the fidelity in the data fit corresponding to $|| \mathbf{A}\bar{\mathbf{F}} - \mathbf{g} ||$ and the smoothness in the recovered $\bar{\mathbf{F}}$. To solve the minimization problem, as presented in equation 4.6, we effectively smooth the source function solution thus suppressing noise and other unphysical disturbances in the inversion.

The source function $\bar{\mathbf{F}}$ which will satisfy this minimization is shown to be (Hansen,1992)

$$\bar{\mathbf{F}}_\lambda = (\mathbf{A}^*\mathbf{A} + \lambda \mathbf{L}^*\mathbf{L})^{-1}\mathbf{A}^*. \tag{4.7}$$

$\mathbf{A}^*$ is the adjoint of the matrix $\mathbf{A}$, and likewise for $\mathbf{L}$. The computational heaviness involved in the calculations of the cross-product matrices in this expression makes it difficult to solve. It is more effective to use the GSVD (Generalized Singular Value Decomposition) algorithm which is incorporated into the OSPEX software. In order to compute the solution of the generalized minimization problem we evaluate the GSVD of $\mathbf{A}$ and $\mathbf{L}$.

GSVD method :

Following van Loan (1976) we consider a $M \times N$ matrix $\mathbf{A}$ and a $P \times N$ matrix $\mathbf{L}$ where $M \geq N \geq P$. The diagonal elements of a diagonal square matrix are singular values. In GSVD we have to evaluate the singular values of non-diagonal matrices, denoted here as $\mathbf{A}$ and $\mathbf{L}$. For each pair of real matrices $(\mathbf{A}, \mathbf{L})$ there exists a set of singular values σ_k^A, σ_k^L satisfying the relation:

$$(\sigma_k^A)^2 + (\sigma_k^L)^2 = 1 \tag{4.8}$$

To determine the diagonal elements a double transformation on the matrices is required, denoted by singular vectors. There exists a set of singular vectors $\tilde{\mathbf{u}}_\mathbf{k}, \tilde{\mathbf{v}}_\mathbf{k}, \tilde{\mathbf{w}}_\mathbf{k}$, where the first two sets are orthogonal and the third one is a set of linearly independent vectors satisfying the simultaneous equations

$$\mathbf{A} = \tilde{U} \begin{pmatrix} \mathtt{diag}(\sigma_\mathbf{k}^\mathbf{A}), & 0 \\ 0 & \mathbf{1_{N-P}} \\ 0 & 0 \end{pmatrix} \tilde{\mathbf{W}}^{-1}, \tag{4.9}$$

$$\tag{4.10}$$

$$\mathbf{L} = \tilde{\mathbf{V}}(\mathtt{diag}(\sigma^\mathrm{L})0)\tilde{\mathbf{W}}. \tag{4.11}$$

Here the $M \times M$ matrix $\tilde{\mathbf{U}}$ is formed from the M column vectors $\tilde{\mathbf{u}}_\mathbf{k}$, $k = 1, ..., M$, with similar definitions for the $P \times P$ matrix $\tilde{\mathbf{V}}$ and the $N \times N$ matrix $\tilde{\mathbf{W}}$. The generalized singular values are therefore defined as the ratios $\sigma_k = \sigma_k^A / \sigma_k^I$. We can express the solution of the generalized minimization problem for the source function as (Hanson, 1992; Kontar, et al., 2004,2005)

$$\bar{\mathbf{F}}_\lambda = \sum_{k=1}^{P} \left(\frac{\sigma_k^2}{\sigma_k^2 + \lambda} \frac{(\mathbf{g}\, \tilde{\mathbf{u}}_\mathbf{k})}{\sigma_k^A} \right) \tilde{\mathbf{w}}_\mathbf{k} + \sum_{k=P+1}^{N} (\mathbf{g}\, \tilde{\mathbf{u}}_\mathbf{k}) \tilde{\mathbf{w}}_\mathbf{k}. \tag{4.12}$$

Higher Order Regularization :

The solution for the source function $\bar{\mathbf{F}}$ is differentiable and can be determined for higher order derivatives. This is referred to as higher order regularization. The are three orders of regularization incorporated into the inversion software:

Zero Order Regularization ; This is employed by Piana et al. (2003), and uses the Euclidean norm $||\bar{\mathbf{F}}||$, $\sim$ the total electron flux. This is met through assigning a value of $\mathbf{L} = 1$ in the minimization problem.

First Order Regularization : Consider again equation 1.17. The source function $\bar{\mathbf{F}}$ is differentiable to a first order, and is related to the injection spectrum in the thick target scenarios. This requirement is applied with $\mathbf{L} \approx \mathbf{D^1}$, in the minimization problem, where $\mathbf{D^1}$ is the differentiation operator.

Second Order Regularization : The injection spectrum found through the first order derivative of the mean electron flux would also be differentiable and have a differentiable first derivative. The requirement on the minimization problem for this condition would be a second order derivative in the constraint operator $\mathbf{L} \approx \mathbf{D^2}$.

Piana et al. (2003) analyzed the 23^{rd} July 2002 flare event, which was also spectrally analyzed by Holman et al. (2003) with a forward fitting technique. They found that zero order regularization was capable of revealing features in the mean electron distribution spectra such as a local minimum near 55 keV, significant excess over the isothermal form in the ~30-45 keV range, increase in the mean electron spectrum over the energy interval ~55 to ~60 keV, which was not accessible with simpler forms associated with forward fitting.

Kontar et al. (2004), found that applying GSVD and higher order regularization to reconstruct a simulated electron spectrum is more effective than using the zero order regularization algorithm, due to the added terms in the regularization solution resulting from higher order differentiation assuring correct behaviour of both the normalized and cumulative residuals.

The Picard Condition :

Achieving the most meaningful construction of the regularized solution lies in the analysis of the quantities (Groetsch, 1984):

$$c_k = \left| \frac{(\sigma_k)^2}{(\sigma_k)^2 + \lambda} \frac{(\mathbf{g}\tilde{\mathbf{u}}_\mathbf{k})}{\sigma_k^A} \right| \qquad k = 1, ..., N, \tag{4.13}$$

c_k are the absolute values of the coefficient of the generalized regularization solution, or the 'condition number'. According to the *Picard Condition* the singular values σ_k should decrease faster on average than the coefficients $(\mathbf{g}, \mathbf{u_k})$. In general, for solar flare HXR spectra (typically steep) an ideal solution structure becomes established when c_k decreases faster with k, so that smaller values of λ, which preserve more fidelity in the solution, can be used.

The Regularization Parameter λ :

The properties and limits on the constraints fundamentally determine the Lagrange mul-

tiplier λ. However, since we do not have prior information on the total flux of X-ray producing electrons we must use knowledge of the errors in the recovered solution to choose λ. In general the optimal λ tends to zero when the noise level tends to zero. According to the *Morozov Discrepancy Principle* (Morozov, 1966) the best value of λ is given by

$$|| \mathbf{A}\bar{\mathbf{F}}_\lambda - \mathbf{g} ||^2 = ||\delta\mathbf{g}||^2. \tag{4.14}$$

$||\delta\mathbf{g}||^2$ is equal to the mean square of the data noise (Tikhonov et al.,1995). However, empirical tests have shown that the parameter it provides is often too large, and the regularized solution over-smoothed (Kontar et al. 2004).

Figure 4.1 presents the results of the Tikhonov Regularization and Picard Condition for HXR spectrum of each event. This is what we are expected to get for every regularized solution in the remainder of this chapter.

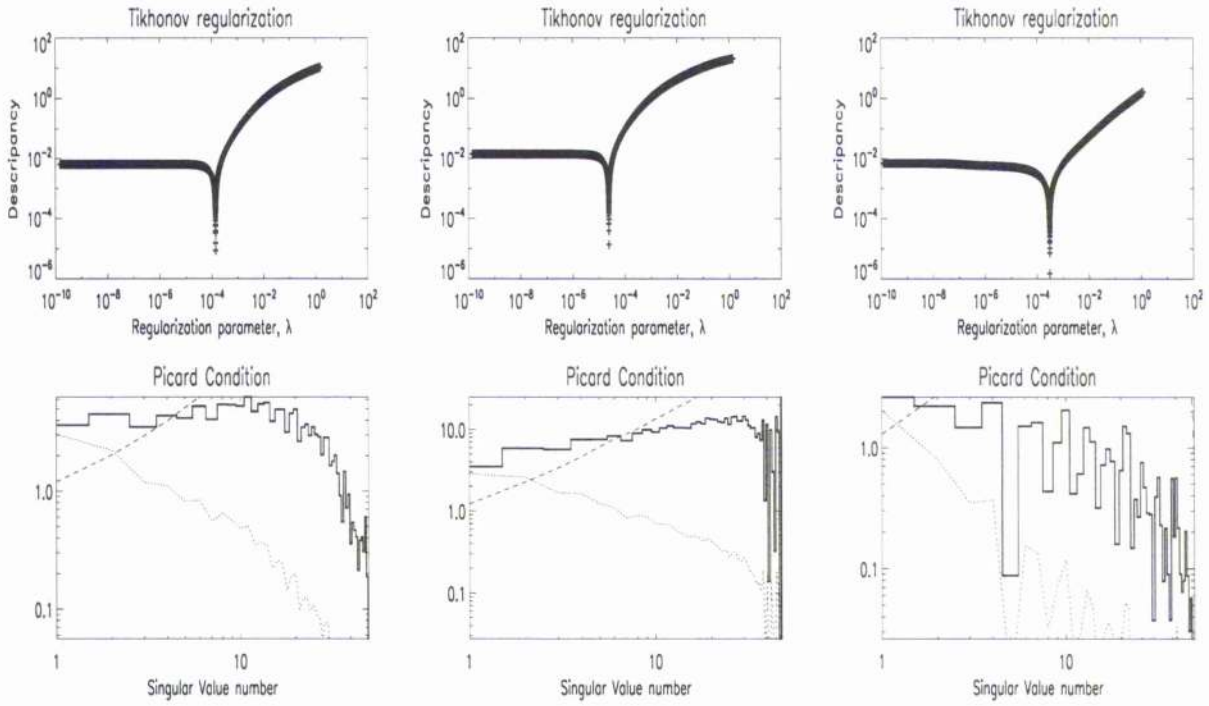

Figure 4.1: Picard condition *bottom row*: Variation of the coefficients c_k (*Solid line*), variation of the coefficients $(\mathbf{g}\tilde{\mathbf{u}}_\mathbf{k})$ (*dotted line*) and variation of the singular values σ_k, i.e. c_k without coefficients $(\mathbf{g}\tilde{\mathbf{u}}_\mathbf{k})$ (*dashed line*), as functions of vector number k from equation 4.13. Tikhonov discrepancy *Top row* for the 17^{th} Sept.2002 (*Left*), 12^{th} April 2002 (*Center*) and 31^{st} Oct.2003 (*Right*) events.

The second row of plots in figure 4.1 tells us that the rate of decrease in the singular values (x-axis) compared with the coefficients is greater for increasing singular values in 17^{th} Sept. 2002, 31^{st} Oct. 2003 and the 12^{th} April 2002 events. The discrepancy principle outlined in equation 4.14 can be written as a minimization problem, given by

$$|| \mathbf{A}\bar{\mathbf{F}}_\lambda - \mathbf{g} ||^2 - ||\delta \mathbf{g}||^2 = \mathtt{Min.} = \wp(\lambda), \tag{4.15}$$

where $\wp(\lambda)$ is a function of λ, the regularization parameter. When the discrepancy declines to zero the minimization is satisfied and the value of λ is determined. From figure 4.1 we see that the regularization parameter used for the regularization solution is around 10^{-4} in each event. This method of evaluation of the regularization parameter will be applied in all regularized solutions to follow and is built into the inversion software. Kontar et al., (2004) also propose a procedure for evaluating the optimal λ based on analysis of the residuals using the following expression

$$r_k = ((\mathbf{A}\bar{\mathbf{F}}_\mathbf{k}) - \mathbf{g_k})/\delta g_k. \tag{4.16}$$

Ideally the normalized residuals should be consistently smooth and unsystematic, along with acceptable variation within random walk limits, as discussed in forward fitting. Generally, a small set of values for the cumulative residuals indicates insufficient smoothing, whereas a set of values consistently exceeding the limits outlined indicates too great a regularization parameter. In all, the problem revolves around adopting a regularization parameter that balances the size of the residuals against the smoothness of the solution. To determine an acceptable regularization parameter we apply χ^2 hypothesis testing. Ideally, the regularization parameter should satisfy

$$\frac{||\mathbf{A}\bar{\mathbf{F}}_\lambda - \mathbf{g}||^2}{||\delta \mathbf{g}||^2} \simeq 1 \tag{4.17}$$

Figure 4.2 illustrates the smoothing effect of the regularization parameter on the HXR spectrum of the 17^{th} Sept. 2002 event with 1keV binning. The regularized solution is smoothed towards the photon flux model from forward fitting, which is a precondition to

the inversion. The solution is best fitted with the model, in this case, when $\lambda = 1.7$. When $\lambda \rightarrow 0$, the solution becomes less smooth and noisy i.e. from top left to bottom right in the figure. When λ=0 the regularized solution matches the direct inversion solution and the second term on the right in the minimization problem in equation 4.5 disappears, leaving only the left term. When λ is included in the minimization the noise in the direct inversion solution is suppressed and the solution is smoother.

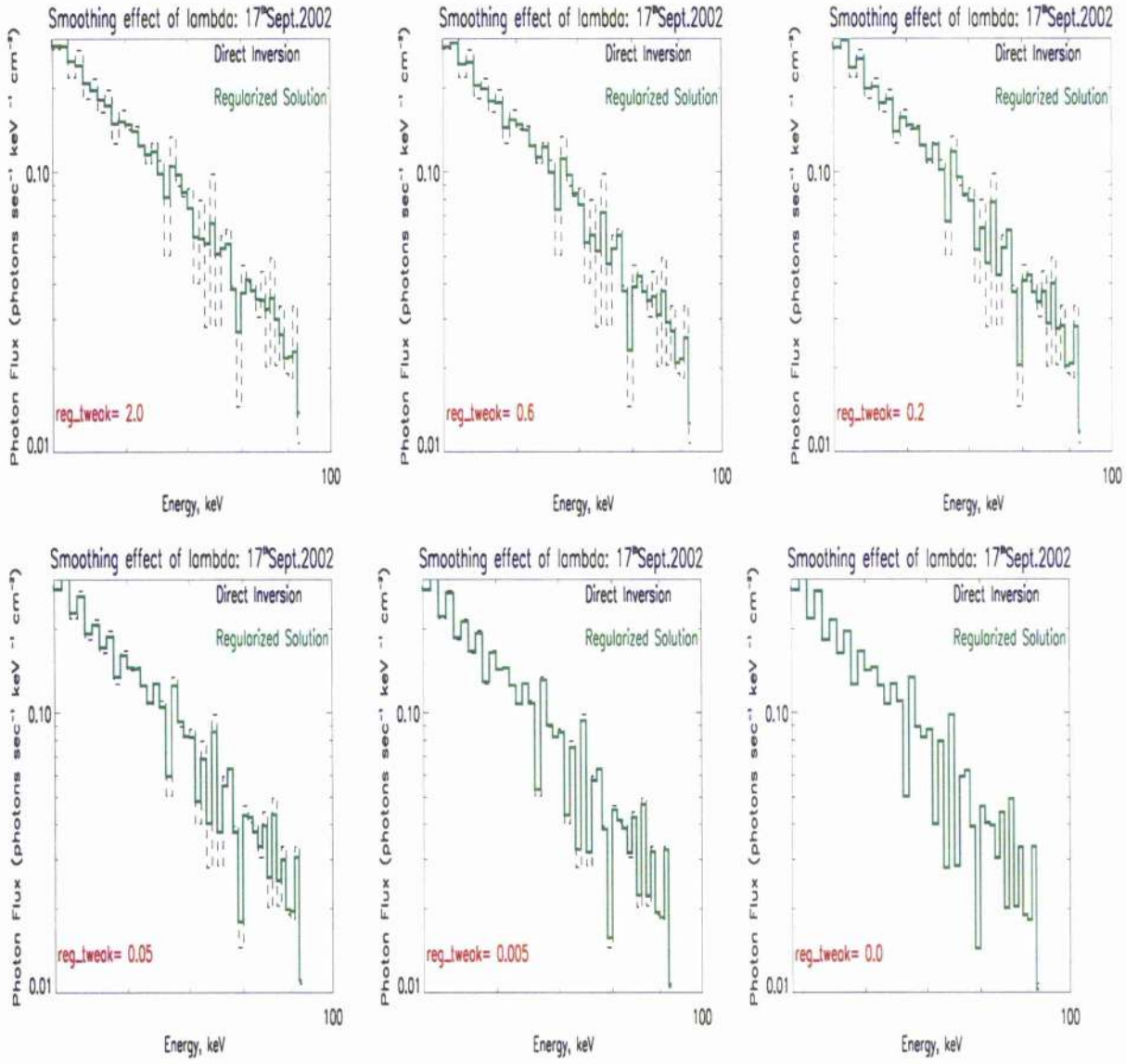

Figure 4.2: Effect of the regularization parameter λ on the regularization photon flux solution, compared with the direct inversion solution for the 17^{th} Sept. 2002 event with 1 keV binning. Notice 1 keV binning creates greater instability and noise amplification in the direct inversion solution compared with a variable binning approach, used in chapter 3. The energy range is 50-100 keV for purposes of clearly observing the smoothing effect due to λ.

4.1 Counts to Photons

We have seen in chapter 3 the derivation of the DRM in the discretized matrix expression (equation 1.22) of the linear integral expression which relates the count flux spectrum to the HXR photon flux spectrum.

It has been shown that inversion of equations of this type are ill-posed with notable instability so generalized regularization should be applied. In this case the source function represents the HXR photon flux spectrum and the count flux spectrum is the data function. We can now introduce these functions into the derived generalized regularized minimization problem from equation 4.6, giving

$$|| \mathbf{DRM} \cdot \mathbf{I} - \mathbf{C} ||^2 + \lambda || \mathbf{L}(\mathbf{I} - \mathbf{I_0}) ||^2 = \texttt{Minimum} \tag{4.18}$$

where $\mathbf{I_0}$ is the photon flux model from the forward fit with respect to the flare event analysis. The **DRM** corresponds to the kernel **A** and is also an $M \times N$ matrix. To control the value of the regularization parameter λ, which effectively controls the level of smoothness in the recovered solution relative to the model, a regularization tweak parameter is assigned as an input into the discrepancy principle in the inversion software. Due to the fact that λ is dependent upon analysis of the normalized residuals relating the regularized photon flux solution and the photon flux model, as well as the Picard condition, we must have control of the discrepancy to ensure acceptable minimization of the solution and evaluation of the regularization parameter. We incorporate the regularization tweak into the inversion software via the discrepancy principle (which calculates λ as a scalar giving

$$|| \mathbf{DRMI}_\lambda - \mathbf{C} ||^2 = \texttt{reg\_tweak} || \Delta \mathbf{C} ||^2. \tag{4.19}$$

ΔC is 1σ uncertainty on the count flux (counts sec^{-1} cm^{-2} keV^{-1}).

The Regularized Inversion Software :

The inversion software created by Eduard P. Kontar (2005)[†], for regularized inversion of count flux to photon flux spectra and count flux to mean electron flux spectra, creates count flux, count flux error, DRM, photon flux model, count space and photon space energy bin data files for the fits, through extraction from OSPEX. The constraint functional with Lagrange multiplier can be used with various orders of regularization selected as an input. GSVD evaluates the singular values and eigenvectors comprised within the regularization solution structure and taken from the DRM array, through a singular value decomposition subroutine. The regularization parameter is then calculated and the solution found through application of equation 4.12. The normalized and cumulative residuals are determined along with the Picard condition for the absolute value of the coefficients and plotted. The results are amended with (`reg_tweak`) until satisfactory residuals, χ^2 test, cumulative residuals and the Picard Condition is observed, depending on the choice of constraint. Regularized inversion error calculations will be also be examined in this chapter. Other such inputs for running the software include

* **order** - Order of regularization (integer). Can be 0(default), 1 or 2.

* **Guess** - Can be 1 or 0(default). To use (=1) or not to use (=0) forward fit model in the constraint. We can choose to incorporate ω into the regularization parameter and solution calculations as a starting value for the minimization of the solution i.e. noise suppression. The variable ω is defined as

$$\omega = \hat{\mathbf{W}}^{-1}(\bar{\mathbf{F}}_0 \cdot \texttt{Guess}) \tag{4.20}$$

So when Guess = 1 the modelled solution from the forward fit becomes important in the regularized solution, whereas when Guess = 0 the model does not become applicable in the solution calculation. The results for the HXR spectrum by generalized regularized inversion of the selected events, from count flux space, are presented in figure 4.3.

[†]Quick start with the inversion software can be found at http://www.astro.gla.ac.uk/users/eduard/rhessi/inversion/

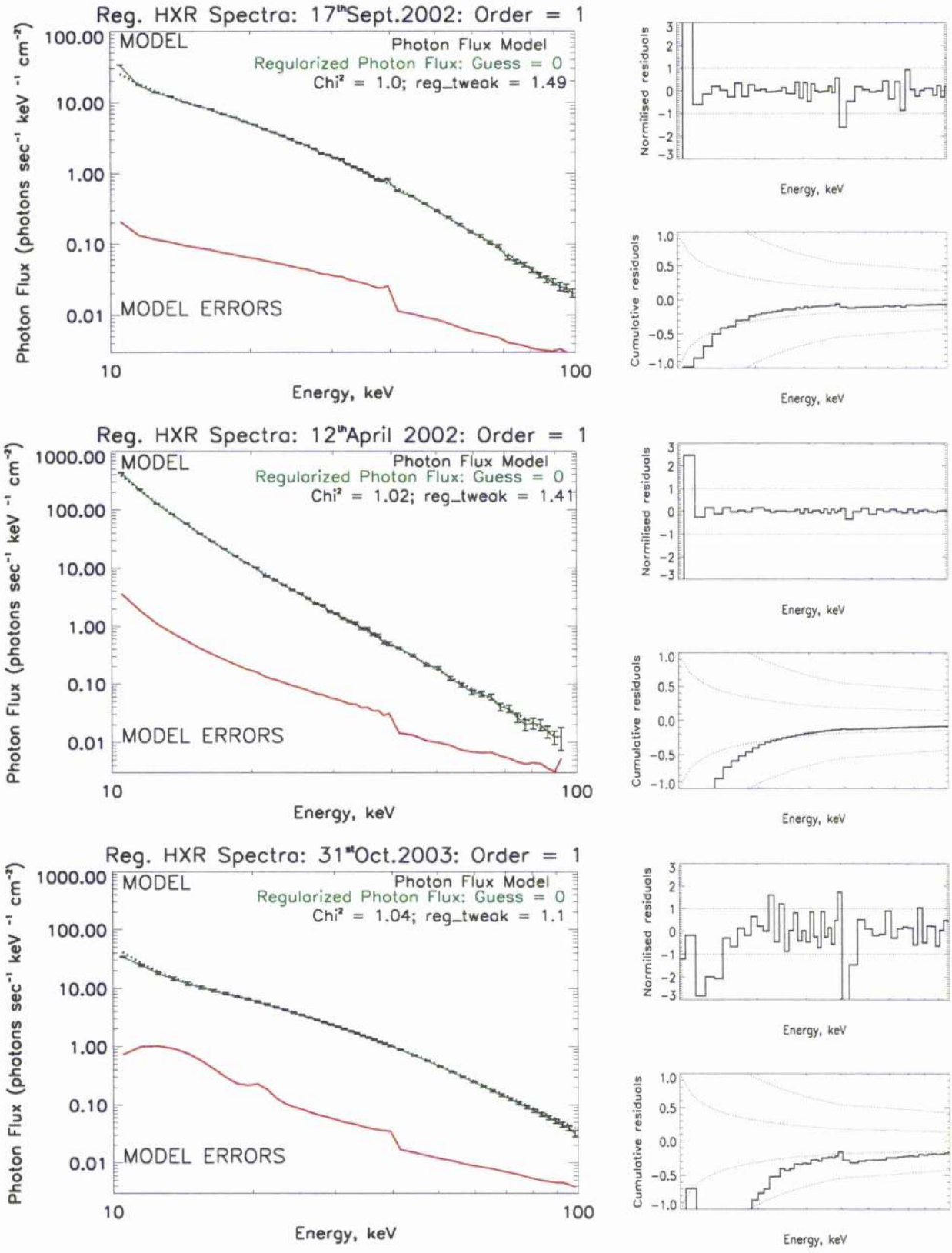

Figure 4.3: The regularization solution for the HXR spectrum from the count flux spectrum for all the events analyzed.

From the results on figure 4.3 noise has been suppressed for the 12^{th} April 2002 and 17^{th} Sept. 2002 events at harder X-ray energies, when compared with the direct inversion results from figure 3.4. The most notable improvement is seen in the 31^{st} Oct. 2003 event from 10 until 40 keV. The negativity and noise in the HXR spectrum at low energies, found with direct inversion, does not exist in the 31^{st} Oct. 2003 event. The effect of the attenuator shutters is effectively solved with regularization through smoothing of the instability which they create in the DRM. The peak in the residuals found at ~11 keV, in both 17^{th} Sept. 2002 and 12^{th} April 2002 events is an emission line which was predicted due to K-escape discussed in chapter 2. The error ratios for each event, comparing the results for the regularized solution and forward fitting, are presented in figure 4.4.

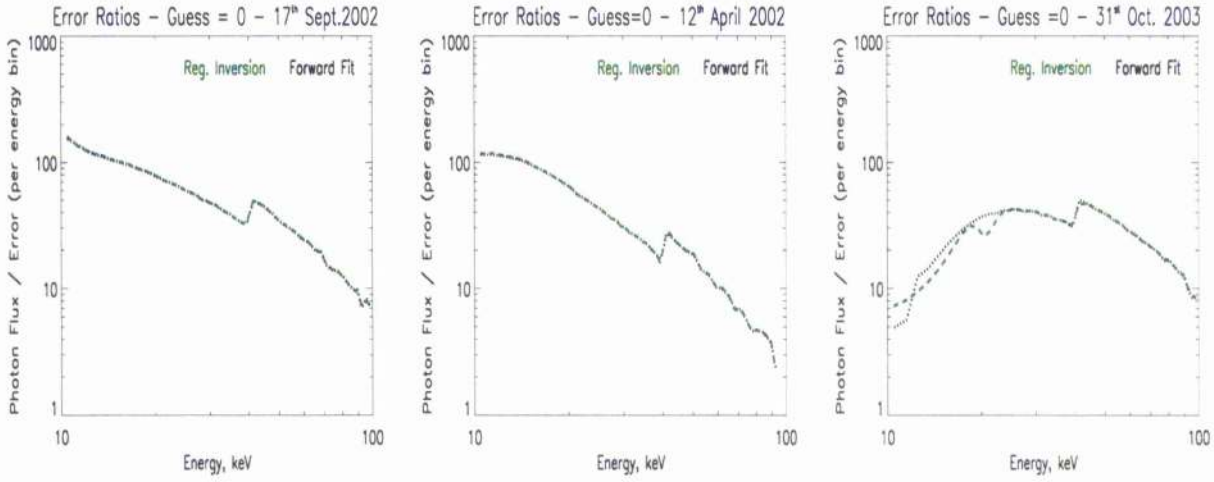

Figure 4.4: Error ratios found through regularization and forward fitting, for comparison. 17^{th} Sept. 2002 *Left*
, 12^{th} April 2002 *Center* and 31^{st} Oct. 2003 *Right*.

The fact that the error ratios are so similar show that estimation of the errors in the regularized inversion technique is just as accurate as those calculated through forward fitting. This allows for accurate and reliable comparisons to be made between the solutions found through each technique. We can conclude that the smoothed solutions from regularized inversion are valid and physically real, without suppression of real features, and the lack of smoothness in forward fitted solutions is most certainly due to noise. The regularized solutions have all been successfully smoothed to the photon flux model while maintaining ac-

ceptable statistical analysis is the normalized residuals and χ^2 ($\approx$1) testing. A regularization order of 1 was applied for each of the results giving maximum likelihood of recovering spectral features. Figure 4.5 presents the residuals for the regularized solution to be compared against the forward fit residuals in the HXR spectrum.

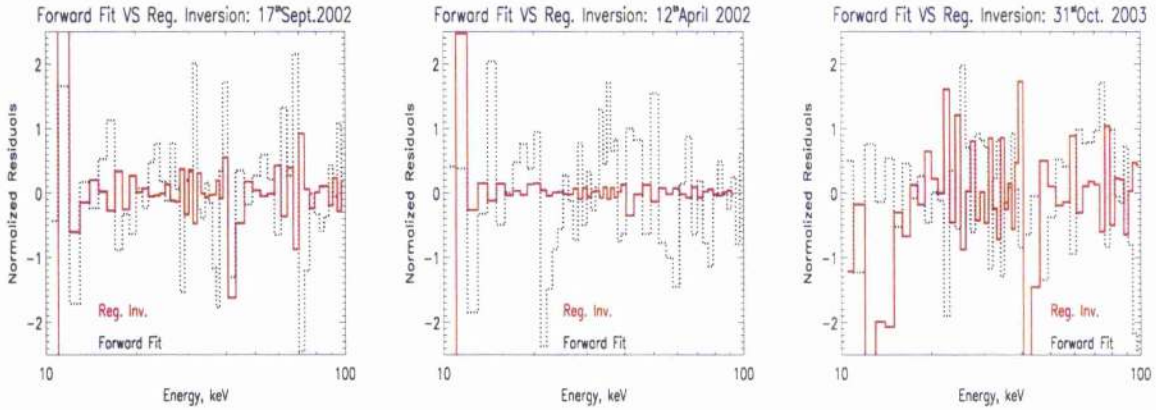

Figure 4.5: Compare residuals for regularization with direct inversion approaches, for 17^{th} Sept.2002 (*Left*), 12^{th} April 2002 (*Center*) and 31^{st} Oct.2003 (*Right*).

The smoothing effect of regularized inversion, found within each of the events, is most obvious through comparison of the residuals in figure 4.5. The residuals from the fit of the regularized solution with the forward fitted photon model is significantly less noisey in all events. This is particularly evident in the 17^{th} Sept. 2002 and 12^{th} April 2002 events. The statistical acceptability in the regularized solution and choice of regularization parameter is monitored through the normalized and cumulative residuals, χ^2 testing, Picard condition and Tikhonov discrepancy, as described earlier. The solutions found with regularization are clearly more statistically acceptable than those found with forward fitting, while complimented by noise suppression. This conclusion is drawn from the fact that the two methods present equally acceptable χ^2 testing and error estimation, but with much improved normalized residuals and cumulative residuals in the case of regularized inversion.

Effect of Guess on the Solution :

The input value for Guess used in the software to determine the regularized solutions was set to 0 for each event. This implies that the forward fitted photon model, for each event,

would not be used in the constraint. Guess = 0 is preferred to Guess = 1, for determining regularized photons from counts when we observe the residuals for the regularized solution fit to the model of each event. The residuals become less unsystematic and more amplified by noise with Guess = 1, resulting in cumulative residuals extending beyond the random walk limits of $\pm 1\sigma$. More importantly the error ratio is distorted and poorer at lower energies with Guess = 1. This is evident when we compare the error ratios for Guess = 1 in figure 4.6 (*Left*) and Guess = 0 in figure 4.4 for the 17^{th} Sept. 2002 event, and also the error ratio for Guess = 1 on figure 4.6 (*Right*) and Guess = 0 on figure 4.4 for the 31^{st} Oct. 2003 event.

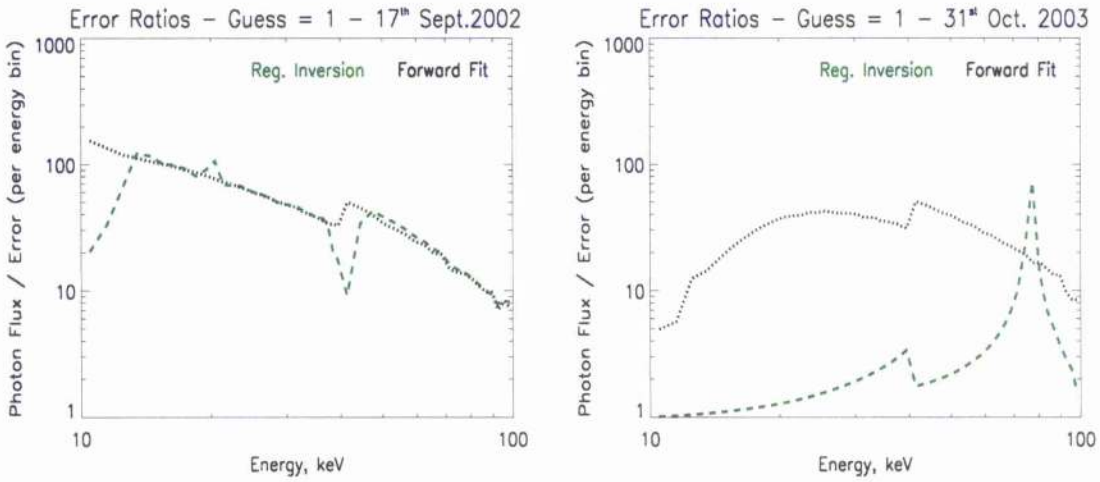

Figure 4.6: The effect of selecting 'Guess = 1' in the inversion parameters results in increased errors of the regularized solution, compared with 'Guess = 0' for 17^{th} Sept.2002 (*Left*) and 31^{st} Oct. 2003 (*Right*).

The effect of Guess in the counts to regularized photons procedure presented in the previous figure is also evident in the 12^{th} April 2002 event, which is not presented.

4.2 Error Calculations in Regularized Inversion

The discretized linear inverse problem we want to solve can be rewritten to include the error in the data function

$$\mathbf{g} = \mathbf{A}\bar{\mathbf{F}}_{\mathbf{true}} + h. \tag{4.21}$$

Here, h is the error in the data function of $\mathbf{g}$.

The solution of the general regularized source function through GSVD, given in equation 4.12, can be expressed in simpler terms as

$$\bar{\mathbf{F}}_{reg} = \mathbf{R}^{-1} \cdot \mathbf{g}. \tag{4.22}$$

$\mathbf{R}^{-1}$ is a regularization matrix operator representing the linear set of equations characterized by the components of the solution equation 4.12. Therefore $\mathbf{R}^{-1}$ exists for all methods of regularization. Clearly then, we can assume that $\mathbf{R}^{-1} \approx \mathbf{A}^{-1}$. The error in the regularized solution is therefore the difference between the regularized solution of the source function and the true solution of the source function. By substituting equation 4.21 into equation 4.22 and subtracting the term $\bar{\mathbf{F}}_{\mathbf{true}}$ from both sides of the new version of equation 4.22 we get the error calculation for the regularized solution of the source function

$$\Delta\bar{\mathbf{F}} = \bar{\mathbf{F}}_{reg} - \bar{\mathbf{F}}_{true} = \mathbf{R}^{-1}(A\bar{F}_{true} + h) - \bar{F}_{true} \tag{4.23}$$

$$\Rightarrow \Delta\bar{\mathbf{F}} = (\mathbf{R}^{-1}A - 1)\bar{\mathbf{F}}_{true} + \mathbf{R}^{-1}h \tag{4.24}$$

To determine the regularization errors the inversion software is adapted to include the left and right components of the above equation. The left term from equation 4.24 tells us about the energy resolution in the regularized solution. Consider that $\mathbf{G} = \mathbf{R}^{-1}A$ is not equal to 1, but has some non-diagonal elements i.e. a point spread function. The energy bin resolution is therefore probabilistic, much the same as the photon energy resolution with the DRM, and can be represented as a Gaussian distribution with FWHM (Full-Width-Half-Maximum). The FWHM will be presented on the mean electron distribution plots, as horizontal error bars, for each event.

The last term describes the noise propagation across the energy range of the source function (vertical errors in solution). This can be seen as a classical approach to error analysis again with a Poisson error distribution. The problem presented in equation 4.22 is very similar to the problem of calculating photon flux errors by direct inversion. However,

instead of a DRM matrix we have a regularization operator (R^{-1}). The expression for calculating photon errors from count errors using discretized matrices with the inverted DRM could be written as

$$\Delta\tilde{F}_{direct}(\varepsilon_j) = \sqrt{\sum_{j=1}^{N} \left[\mathbf{DRM}_{ij}^{-1} \,.\, \Delta g(\varepsilon_j)\right]^2} \tag{4.25}$$

Since $\mathbf{R^{-1}} \approx \mathbf{DRM^{-1}}$ we can now write an equivalent error expression for the errors in the regularized solution of the source function (new method) i.e. which should be applicable to both HXR photon flux spectra and mean electron distribution spectra

$$\Delta\tilde{F}_{reg}(\varepsilon_j) = \sqrt{\sum_{j=1}^{N} \left[\mathbf{R}_{ij}^{-1} \,.\, \Delta \mathrm{g}(\varepsilon_\mathrm{j})\right]^2} \tag{4.26}$$

The original software determined vertical errors in terms of confidence intervals (old method). A confidence interval is an interval between two numbers (upper and lower limits of vertical error bars) with an associated probability. The probability functions in this case are with respect the energy intervals of the regularization operator matrix with M-dimensions. The vertical extent of the errors were deduced from repeated inversions using uniform random realizations of the data set, with the uncertainties in the photon spectrum deduced from the Poisson uncertainties in the instrument count rates in each 1 keV energy channel (Piana et al., 2003). The original inversion software determines the confidence interval within 1σ uncertainty on the probability functions, using the data function errors. Through calculating numerous regularized solutions within this 1 sigma confidence strip i.e. adjusting the data function in the range of its errors, we can estimate the upper and lower limits to the regularized solution. All possible solutions within the data function errors, contribute towards the regularized solution confidence interval.

The regularized inversion and forward fit error ratios are presented in figure 4.7 for the 17^{th} Sept. 2002 event only, for comparison between old and new methods of vertical error evaluation.

Figure 4.7 tells us that the classical Poisson method is a better way of determining the errors in the regularized solution. The regularized error ratio of the (*Left*) plot is consistently

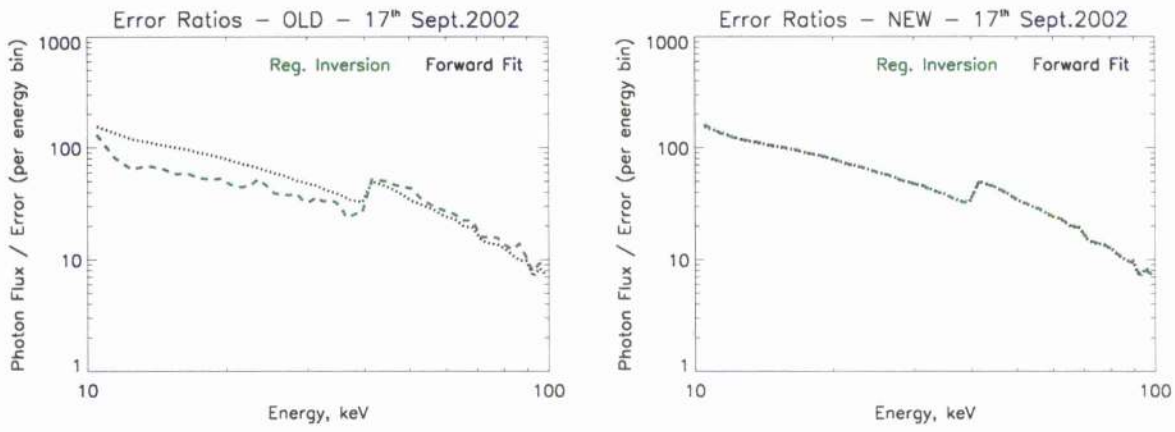

Figure 4.7: Error ratios through forward fitting, direct and regularized inversion, when using the software error analysis method (*Left*) compared with the Poisson errors (*Right*). This trend is also applicable to the other events.

reduced compared with the forward fit result up until 40 keV. Ideally, the error ratios should match, or at least improve upon forward fit errors, as is the case with a Poisson error analysis (*Right*). Adapting the software to include a calculation of the errors in the regularized solution is done through inputting the errors in the count data into the regularization solution calculation procedure, as opposed to the count data itself.

4.3 Counts to Photons : Effect of Preconditioning on the Solution

For regularization, the data on the measured count rate is required to solve for the photon flux spectrum, with minimization towards a photon flux model, taken from forward fitting. Information is drawn from OSPEX by the inversion procedure on the count flux spectrum and errors along with the photon flux model. With the regularization procedure the actual photon flux model is called as a precondition to the inversion. However, we can assign a photon flux model such as a power spectrum with the spectral index as precondition. There is a distinct effect on the regularized solution for certain precondition values resulting in a distortion in the solution at higher photon energies. Figure 4.8 presents the results for the regularized HXR spectrum for different values of the precondition in the model of the 12^{th} April 2002 event.

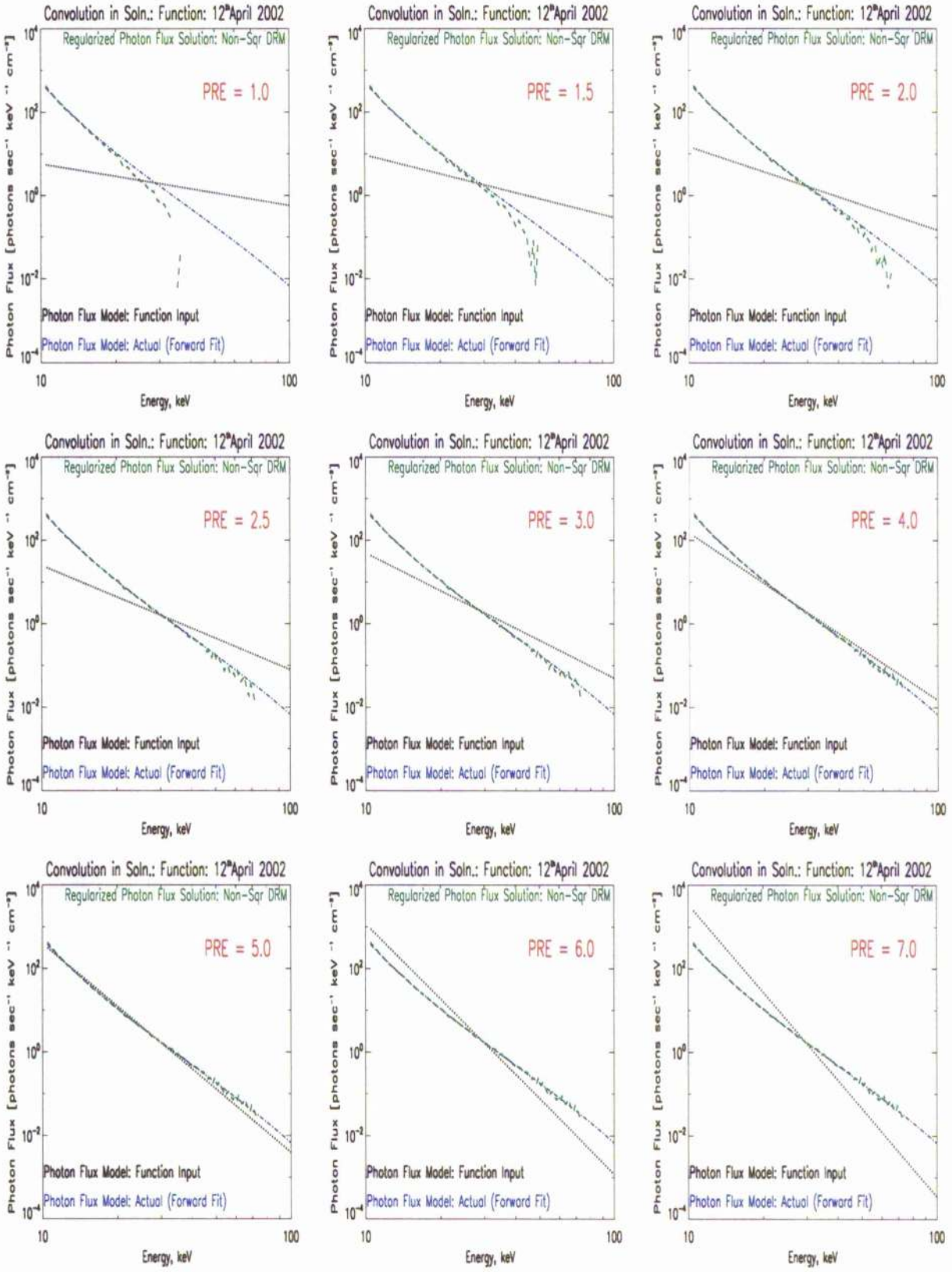

Figure 4.8: Changing regularization solution due to the input photon model index precondition. The input photon model rotates clockwise from the top left plot down to the bottom right plot, with increasing preconditioning value. The actual photon model of the fit for the event is over-plotted for comparison.

Figure 4.8 shows a problem when determining the regularized solution for preconditioning values which do not match the spectral index of the actual model. For example precondition 2, results in a regularized solution which attempts to satisfy minimization in favour of the input photon model while compensating for what the DRM, along with the count flux spectrum, considers to be the true photon model. As a result the solution found with the input photon model becomes significantly degraded at harder energies, for low precondition values, compared with the solution found using the actual photon model from the forward fit. Ideally both solutions should follow each other, independent of the input model. The degree by which the regularized photon flux solution is distorted from the true photon flux model (forward fit) is controlled through determination of the energy range of the observation with respect to the fitted energy range. In other words, controlling the size of truncated region elements in the prescribed DRM array is important. The effect of the truncated region elements results in the problem outlined in figure 4.8. Figure 4.9 presents the regularization solution, for the same 12^{th} April 2002 event, with an input of a square (truncated) DRM, non-square (full) DRM and photon flux models with precondition 2.

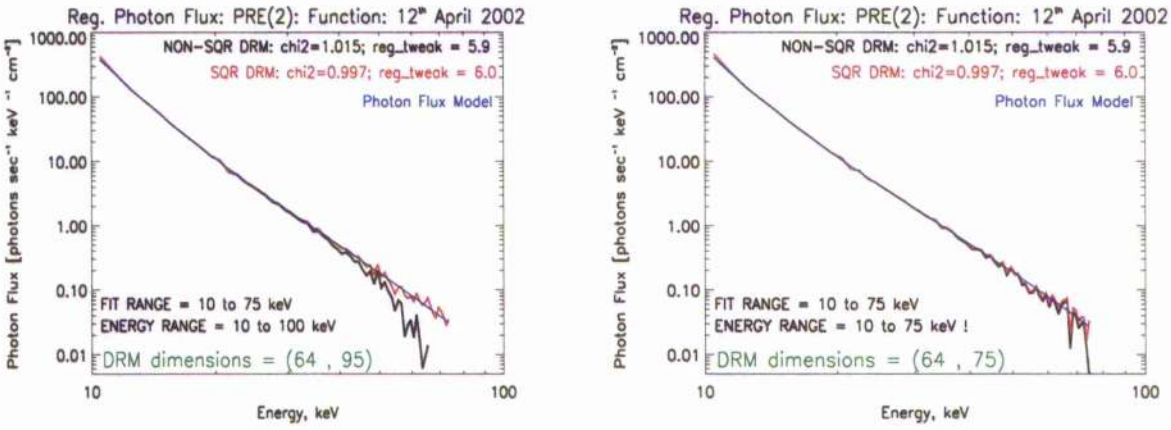

Figure 4.9: Regularized photon flux for 1keV binning in the 12^{th} April 2002 event. *Left* plot shows the solutions with an input DRM array with a large number of M dimensions with respect to the N dimensions. *Right* plot shows the same solutions with input DRM array with the number of M elements closer to that of N, i.e. reducing the size of truncation region elements which contain the response to photon energies outside of the fitted energy range of the photon flux model.

Figure 4.9 (*Left*) presents the full DRM effect on the regularized solution with pre(2) (black) which is equivalent to the top right plot in figure 4.8. The red line show the regularized

solution with the same precondition but for a square DRM, with no influence of the truncated region elements. Figure 4.9 (*Right*) presents the same scenario again, however the black line (full DRM) solution matches the red (square DRM) solution and the problem is fixed. The reason for this is due to reducing the size of the DRM array energy interval elements bringing it closer to the number of energy intervals in the fitted region. This results in a smaller contribution from the truncated region elements of the DRM in the convolution which minimizes the regularized solution. Likewise, for 17^{th} Sept. 2002 flare event, the effect of the truncated region elements contained in the DRM, on the regularized solution is equally apparent. The 17^{th} Sept. 2002 precondition result is presented in figure 4.10.

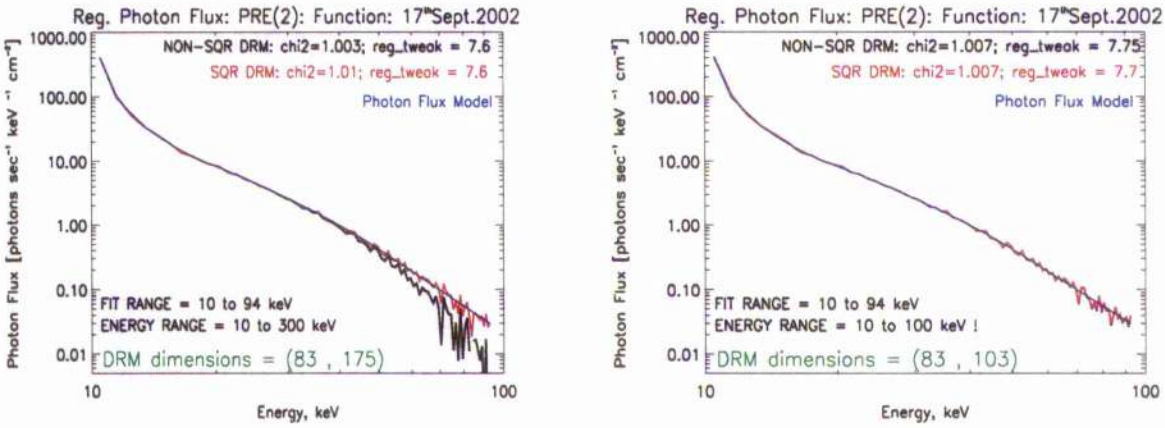

Figure 4.10: The regularization solution, for 1keV binning in the 17^{th} Sept.2002 event, of the HXR spectrum is notably different when we apply square and non-square DRM arrays.

To validate this result we can confidently test whether or not the size of values in the truncated region elements of the DRM array have any real influence on the convolution of the regularized solution. Consider the observation with energy range 10-300 keV. The DRM (83,175) means that there are 83 count energy distributions in the DRM array and 175 photon energy distributions. As discussed before, these distributions represent counts per photon conversion probabilities for each photon energy in the energy range 10-300 keV, with selectable energy bin size. Hence, the 83 count energy bins represent the fit energy range and the distributions from 83 to 175 are truncation region elements of the DRM array i.e. outside of the fit range. Consider the 17^{th} Sept. 2002 event, and allocate zero for all truncated region elements, hence leaving only square DRM elements. This newly formed full

DRM array can be input into the procedure to determine the regularized solution. With a full DRM array we get distortion in the regularized solution as seen in the previous figures. Now by setting zero in the truncation region elements we can confirm whether or not the size of the truncation region elements had created this distortion. The results are shown in figure 4.11.

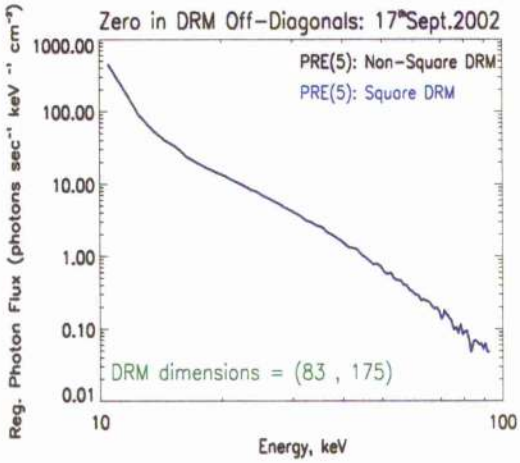

Figure 4.11: The regularized solutions for 17^{th} Sept. 2002 event (1keV energy binning) are identical for both square and full DRM's with photon flux model precondition index of 5.

In conclusion, we can confidently state that the problem regarding distortion of the regularized photon flux spectrum at certain preconditions is due to the presence of truncated region elements of the DRM array. The effect of this distortion is significantly reduced, for any power spectrum, when the sizes of the truncated region elements are reduced to a minimum, or when the energy range of the observation is approximately that of the fitted energy range, thus reducing the number of truncation region elements.

4.4 Photons to Electrons

The Volterra type equation representing the linear integral problem relating the HXR photon flux spectrum $I(\varepsilon)$ to the density and volume weighted mean electron distribution spectrum $\bar{F}(E)$, was derived through thin target X-ray emission in chapter 2 and presented in equation 1.9. The integral can be solved using discretized matrices with the bremsstrahlung cross-section as was done with count to photon calculations using the DRM matrix. The

matrix representation for electrons to photons was also given in chapter 2, equation 1.21. The derivation of the kernel function $Q_b(\varepsilon, E')$ which is the bremsstrahlung cross-section differential in photon energy, represents an ill-posed direct inversion problem, as before. We can rewrite equation 1.21 in discretized matrix form, using a regularization approach

$$\mathbf{I} = \mathbf{S}\bar{\mathbf{F}}. \tag{4.27}$$

$\mathbf{S} = Q_b(\varepsilon, E)$. In this case the source function represents the mean electron distribution spectrum and the HXR spectrum, derived from the measured count flux spectrum is now treated as the data function. We introduce these functions into the derived generalized regularized minimization problem, as done previously for the regularization of photons from counts. Through adaptation of the inversion software relating counts to electrons (discussed later in this chapter), I created an inversion procedure which solves for electrons with the use of the evaluated photon flux as an input. The adaptation of the inversion software to relate photons to electrons allows us to insert photon flux data for each of the events here, in order to determine the mean electron distribution through regularization. The quality and fidelity of the mean electron distribution spectra will tell us whether or not regularization is an improvement on forward fitting in determining the true spectrum. The corrected calculation of the error in the regularized solution will also be incorporated into the procedure. The new minimization problem for calculating electrons from photons is given as

$$|| \mathbf{S}\bar{\mathbf{F}} - \mathbf{I} ||^2 + \lambda || \mathbf{L}(\bar{\mathbf{F}} - \bar{\mathbf{F}}_\mathbf{0}) ||^2 = \texttt{Minimum}. \tag{4.28}$$

$\bar{\mathbf{F}}_0$ is the mean electron flux model derived through forward fitting. Similarly, the code finds the regularization parameter using the discrepancy principle, now defined as

$$|| \mathbf{S}\bar{\mathbf{F}}_\lambda - \mathbf{I} || = \texttt{reg\_tweak} ||\Delta\mathbf{I}||. \tag{4.29}$$

where $\Delta\mathbf{I} = 1\sigma$ uncertainty on the photon flux. Note that this includes a systematic uncertainty for the 17^{th} Sept. 2002 and 31^{st} Oct. 2003 events, which was added in quadrature in the error calculations of the photon flux in the OSPEX software. This systematic uncer-

tainty increases the overall uncertainty in the photon energy bins, and hence will induce a certain amount of additional smoothing upon the regularized solution of the mean electron distributions, for the events stated. The results for the regularized mean electron distribution spectra, for each event under analysis, smoothed to no low energy cutoff electron flux models, are presented on figure 4.12. The results for the regularized mean electron distribution spectra, for each event, smoothed to an electron flux model with a low energy cutoff, are presented in figure 4.13. Figure 4.13 presents the regularized solutions for the mean electron flux distribution for the events which featured a low energy cutoff in the electron model from the forward fit. Instantly we observe features in the distribution which appear to be real after careful analysis of the errors and residuals. The flux for non-thermal electrons appears to peak at a higher value, at the low energy cutoff, in both 17/09/02 and 31/10/03 events, compared with the electron model from forward fitting. The electron flux then declines over a short energy range between 20-25 keV for both 17/09/02 and 31/10/03. This feature distributes Poisson errors which lie outside of the model solution, hence potentially real. There also appears be a dip feature in the 31/10/03 event between 26-29 keV. There may also be a possible feature in the spectra between 35-40 keV for 17/09/02, however it may also be unphysical due to the errors. Such bumps and dip features are evident when the solution is regularized to a no low energy cutoff model, as presented in figure 4.12. The possible feature between 35-40 keV for 17/09/02 is more clearly evident in this case. This may mean the fits to the photon model from the count flux spectrum are better with the no low energy cutoff scenario and we observe reduced noise in the errors about this energy, thus revealing more detail in this bump feature. The measured χ^2 values for all regularized inversions is $\approx$1 in all solutions presented, allowing comparisons to be made between the no and low energy cutoff scenarios. Clearly, the low energy cutoff feature in the regularized solution in the no low energy cutoff scenario for the 17/09/02 event is distinct and evident at about the same energy range as was found in the low energy cutoff model. This point proves that the regularized solution is model independent all the while revealing important features in the source function, which forward fitting failed to show.

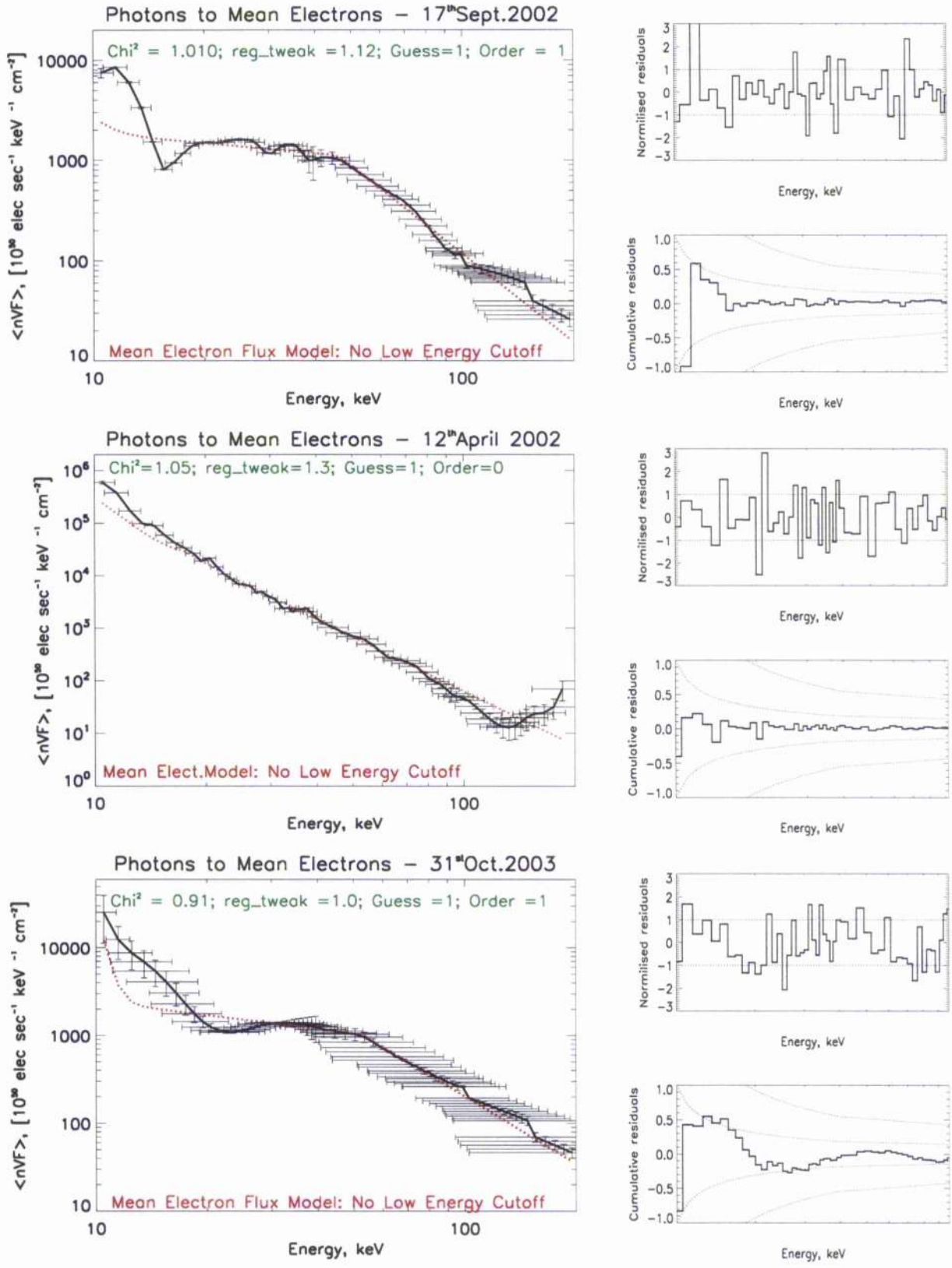

Figure 4.12: Regularized mean electron distributions from regularized photons, smoothed to a no low energy cutoff mean electron flux model for 17^{th} Sept.2002 (*top*), 12^{th} April 2002 (*Middle*) and 31^{st} Oct.2003 (*bottom*) events.

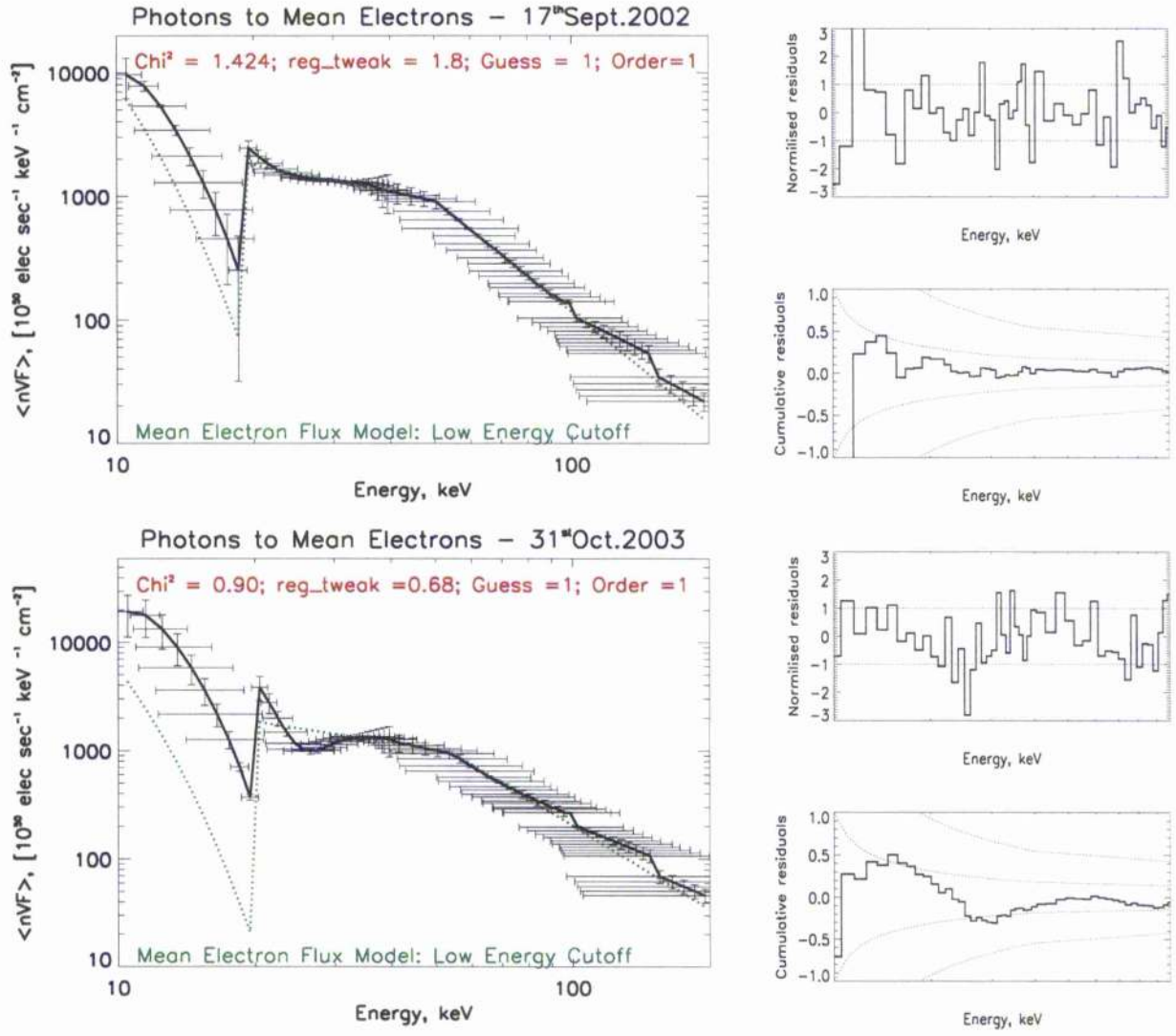

Figure 4.13: Regularized mean electron distributions from regularized photons, smoothed to a mean electron flux model with low energy cutoff feauture for 17^{th} Sept.2002 (*top*) and 31^{st} Oct.2003 (*bottom*).

The low energy cutoff feature is less evident in the no low energy cutoff scenario for the 31/09/02 event, possibly signifying that a no low energy cutoff in the electron distribution is present for this event. The decline in the number of thermal electrons, until the low energy cutoff is not as great as was predicted by forward fitting for 31/10/03 when we look at figure 4.13. The minimum flux at the low energy cut-off, at ≈18keV is ≈20 electrons sec^{-1} keV^{-1} cm^{-2}, whereas regularization predicts a higher flux of ≈300 at this energy. This is also the case when we look at the no low energy cutoff scenario which does not predict any significant low energy cutoff in the solution. The results for 31/10/03 in figure 4.12 also show a steep

decline in the electron flux (thermal electrons) until ≈20-25 keV. This steep decline is also evident in the no low energy cutoff scenario. Its existence in both scenarios may lead us to conclude that this feature is real. The results for 12/04/02 show that there is no low energy cutoff present at all due to a large thermal electron population that must be present in the flare. This is possible since the electron flux at ≈ 10 keV in the 12^{th} April 2002 event is almost 2 orders of magnitude greater than the flux at ≈10 keV in the other two events. The size of the electron flux for low energy electrons in the solution reveals that it is potentially greater than what was revealed by forward fitting, since the slope of the solution from 10-25 keV is raised slightly above that of the model. It is not certain whether or not this result is real or the slightly reduced flux in the model is due to thin shutter attenuators in position. However, the regularized solution does recover a possible feature from 40-50 keV with slight bumps and dips, revealed with the reduced errors. There may also be evidence here of a high energy cutoff within the energy range of 120-200 keV. In this regularization I used zero order in the constraint. To recover a higher degree of accuracy in the regularization solution I should also consider first order and possibly second order regularization to fully analyze this high energy cutoff feature. Second order regularization (Kontar et al.,2004) was found to be better at preserving information on these global properties of the solution rather than small scale properties such as bumps and dips. The results for first and second order regularization on 12/04/02 are presented in figure 4.14.

In figure 4.14 (*Left*) we can see that when using first order regularization this high energy cutoff becomes more distinct. The plot on the *Left* shows that the high energy cutoff feature and the bump feature from 30-40 keV become more prominent with increasing the order of regularization from 0-2. The errors on the second order regularization solution can be compared with the electron flux model solution and confirm that such features may be real. The statistical analysis for such fits with the mean electron flux model is satisfactory with χ^2 ≈1 and, acceptable normalized and cumulative residual analysis within the limits of the uncertainties for all regularized solutions presented in the figures of this section. With a simpler and new approach, through inferring the mean electron flux directly from count flux data, I will establish equally acceptable fits to the electron models with χ^2 testing

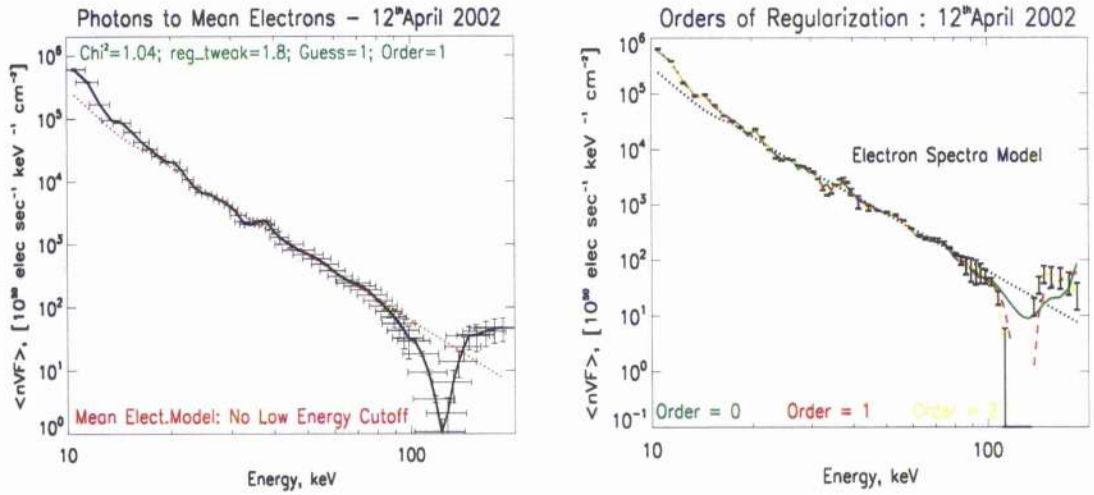

Figure 4.14: Regularized electrons with order 1 for 12^{th} April 2002 event *Left*.Comparing all orders of regularization for the mean electron distribution from photons, with low energy cutoff, for the 12^{th} April 2002 event *Right*.

and residual analysis, in order to conclude on these features found in the mean electron distribution solutions from the HXR spectra.

4.5 Counts to Electrons

We now present a new and faster approach to inferring mean electron distribution spectra. To date, the linear integral relates the photon flux spectra to mean electron distribution spectra, using the bremsstrahlung cross section, through (Brown 1971) thin target considerations of the density weighted source volume of the flare. It appears that accurate construction of the HXR photon flux spectrum is a prerequisite when one wants to construct faithfully the mean electron flux spectrum. As we have seen, measurement of such HXR photon flux incident on satellite detectors presents a further Volterra type integral equation relation through the detectors response matrix. Thus, solving for electrons has required a double analysis of such linear integral equations which in itself synergistically effects noise amplification through the inversions. It is also important to note that a double regularization from counts to photons then photons to electrons may present an overly smoothed mean electron distribution with statistically acceptable fits to the model, thus hiding real features.

Ideally, a one step regularized inversion rather than a two steps would present a more attractive and more efficient procedure with possible benefits encapsulating non-distinct features of the regularized mean electron distribution spectrum, with a single regularization. Derivation of a one step procedure relating directly between the count flux spectrum and mean electron distribution spectrum is relatively simple and sidesteps analysis of the HXR spectrum. Comparison between all methods discussed so far, in constructing mean electron distribution spectra, will fundamentally allow us to determine the best approach to this inversion problem, and help us understand electron propagation in much more detail. The photon flux spectrum at Earth is given in matrix form as shown in equation 4.27. The corresponding count flux spectrum in the X-ray detectors has also been given in matrix form in equation 1.22. As a result we are presented with two matrix equations for the photon flux spectrum $\mathbf{I}(\varepsilon)$, which can be equated giving

$$(\mathbf{DRM})^{-1}\mathbf{C} = \mathbf{S}\bar{\mathbf{F}} \tag{4.30}$$

Multiplying through both sides by $\mathbf{DRM}$ gives:

$$\mathbf{C} = \mathbf{DRM}\,\mathbf{S}\,\bar{\mathbf{F}} \;\Rightarrow\; \mathbf{C} = \mathbf{B}\,\bar{\mathbf{F}}. \tag{4.31}$$

$\mathbf{DRMS}$ can be written as a single function denoted here as $\mathbf{B}$. Hence, we get a matrix directly relating the count flux spectrum to the mean electron distribution spectrum provided we know both the $\mathbf{DRM}$ and the bremsstrahlung cross-section $\mathbf{S}$. This is a Volterra type equation, hence ill-conditioned, and regularization should be applied in order to solve for the mean electron distribution spectrum. Both photon to electron and count to electron inversions extract the electron flux model $\bar{\mathbf{F}}_0$ from OSPEX due to forward fitting, as well as the detector response matrix and the bremsstrahlung cross section (Haug, 1997) for calculating $\mathbf{B}$. Ultimately, the code then finds the solution for the new minimization problem as before, given by

$$||\,\mathbf{B}\cdot\bar{\mathbf{F}} - \mathbf{C}\,||^2 + \lambda||\,L\cdot(\bar{\mathbf{F}} - \bar{\mathbf{F}}_0)\,||^2 = \texttt{Minimum}. \tag{4.32}$$

The code finds the regularization parameter again using the discrepancy principle. The results for the regularized solution of the mean electron distribution spectrum due only to regularized inversion with the measured count flux spectrum for each event, regularized with a no low energy cutoff electron model, can be viewed in figure 4.15. A low energy cutoff model scenario in the electron distributions from counts can be viewed in figure 4.16. Figure 4.16 presents the regularized electron distributions from counts with a low energy cutoff electron model in the 17/09/02 and 31/10/03 events. From first impressions it is clear that both solutions have very acceptable fits to the model in the normalized residuals and reduced χ^2 values. For 17/09/02 the regularized solution is clearly an improvement upon the solution found with photons to electrons. The features within the energy range from 25-40 keV are indeed much more evident than was found with photons to electrons for a low energy cutoff scenario. In fact, these features correspond with those found in the photons to electrons no low energy cutoff scenario, from figure 4.12. Likewise the solution for counts to electrons in the no low energy cutoff scenario in figure 4.15 shows a much more definite low energy cutoff feature than the photon to electrons solution, with highly comparable fits to the no low energy cutoff electron model.

In general, the counts to electrons approach appears to display features in the solution spectrum in more detail with reduced errors and improved energy resolution, compared with photons to electrons in both no and low energy cutoff scenarios, for 17/09/02 and 12/04/02 but not for 31/10/03. It must be emphasized that the solutions in photons to electron regularized inversions are, in a sense, double regularization with twice the smoothing effect on the solutions than those found through counts to electrons. In that case we cannot compare the χ^2 tests on the solutions with the models by these approaches.

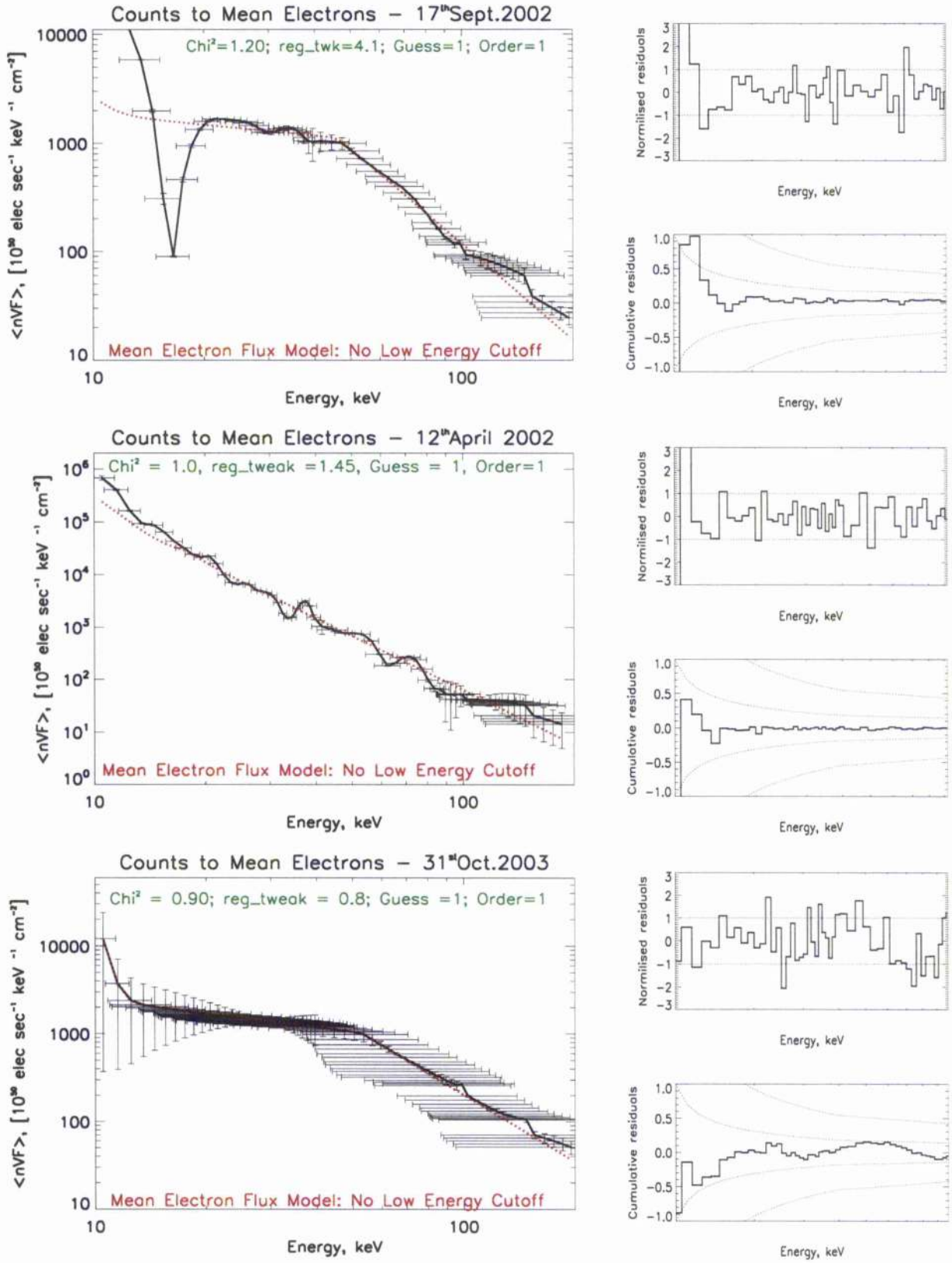

Figure 4.15: Regularized mean electron distributions from count flux spectra, with no low energy cutoff in the electron model, for 17^{th} Sept.2002 (*Top*), 12^{th} April 2002 (*Middle*) and 31^{st} Oct.2003 (*Bottom*).

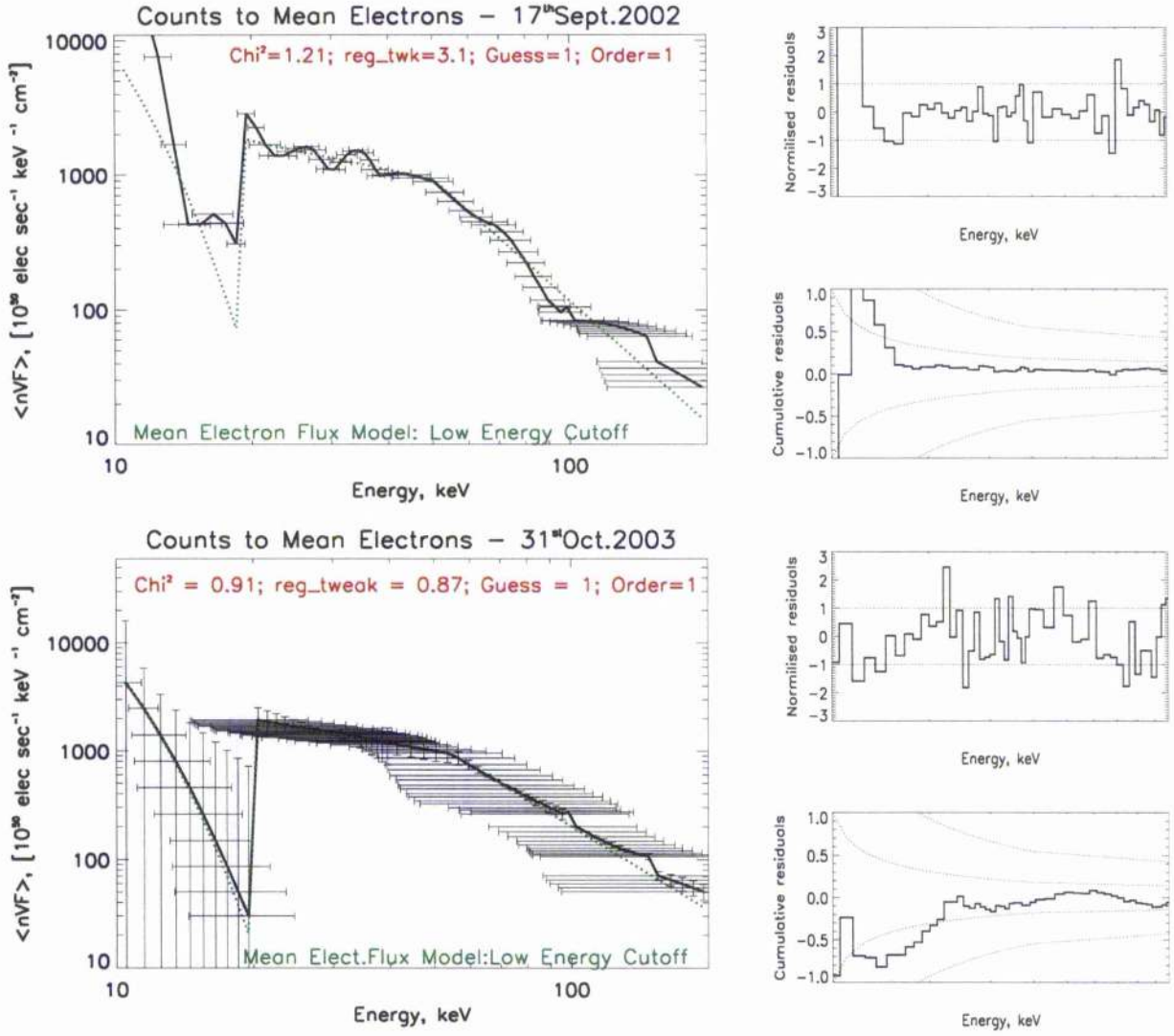

Figure 4.16: Regularized mean electron distributions from count flux spectra, with low energy cutoff in the electron model, for 17^{th} Sept.2002 (*Top*) and 31^{st} Oct.2003 (*Bottom*).

Nevertheless, I will explain how it is possible to justify a comparison between the methods for regularizing mean electron distributions and draw conclusions on certain features in the selected events. The χ^2 test indirectly indicates the degree of smoothing in the solution as it naturally increases with `reg_tweak`. In other words, the photons to electrons solution may be just as accurate as counts to electrons here, only it has been over smoothed, resulting in a larger χ^2 value. In theory then, a lower χ^2 term in the photons to electrons solutions would allow for a more ideal comparison with respect to the χ^2 for the counts to electrons solutions. The problem is how to adapt the inversion software to reliably compare χ^2 for these methods and furthermore faithfully draw conclusions on the results. To solve this problem the errors

in the counts, for counts to electrons, were increased by the equivalent systematic uncertainty as was done for photons (from counts) in photons to electrons. This compensates, in terms of χ^2 in counts to electrons, for the smoothing effect on the electron solution by the photons to electrons algorithm. This uncertainty was taken from the fits used to determine the true photon flux within OSPEX software, for each event. In turn, the value of χ^2 in the regularized solution for counts to electrons is systematically lower for each solution. This has the same effect as decreasing the χ^2 term in photons to electrons for better comparisons, discussed previously. Hence, when χ^2 in counts to electrons solutions is equivalent to χ^2 of the photons to electrons solutions, the comparison is much fairer. Otherwise, the solutions for counts to electrons appears under-regularized and the bumps and dips in the solutions are more greatly emphasized.

Consider the 31/10/03 event with counts to electrons in figure 4.16 and 4.15. Very large errors occur, both vertical and horizontal, around the low energy cutoff with solutions very much smoothed to the model, in both figures, rendering them almost entirely featureless. However, the residuals appear to be acceptable and $\chi^2 \sim 1$ indicating a good fit to the model. One possibility is that the large errors could be due to the inaccuracies of the DRM due to thick shutter attenuators creating much instability at low count energies, which was otherwise corrected with counts to photons inversions and so not evident in the photons to mean electrons solutions. This error amplification may have resulted from the product of the bremsstrahlung cross-section and unstable A3 state DRM matrices. In conclusion, the photons to electrons method has proved more effective in constructing mean electron distribution spectra in this event with more detail particularly in the low energy cutoff scenario presented in figure 4.13.

Finally, consider the 12/04/02 event for counts to electrons from figure 4.15 and as before compare with the solution found with photons to electrons in figure 4.12. Again, acceptable fits (χ^2 almost exactly 1.00) to the models, with normalized residuals, Picard condition and discrepancy principle have prevailed in both approaches making their solutions highly com-

parable. Let us also consider figure 4.14 which displays the photon to electron solution for higher orders of regularization. In all, it is clear that the features present in the solution spectrum in the energy range 30-40 keV are physical and more distinct with a counts to electrons approach. The solution in figure 4.15 also reveals possibly a new dip and bump feature in the 55-75 keV energy range, which was otherwise not revealed in the photons to electrons solution which is generally over-smoothed due to the double regularization, as was the case with 17/09/02 event. The question regarding the possible high energy cutoff feature between 100-200 keV is not evident in the counts to electrons approach for any order of regularization, and it is most likely unphysical. Its presence in the photons to electrons solutions may be explained as a result of insufficient background subtraction from the count flux data at the fit energy range boundary (~100 keV) for this event.
Yet, the minor bumps and dips in the solution spectra found by the counts to electrons approach, for 17/09/02 and 12/04/02, in the energy range 30-50 keV, cannot be deemed as physically real until we consider the possibility of contamination in the source spectrum which may have brought about these instabilities, otherwise termed as the albedo effect.

The Albedo effect :

As summarized by Alexander & Brown (2002), deka-keV photons emitted downwards in the optically thin solar atmosphere undergo Compton backscatter in the low atmosphere and add to the total observed photon fluxes. Photons of energy ~100 keV penetrate the dense photospheric layers so deeply that they are lost to the observer, while below ~10 keV they are photoelectrically absorbed by their first scattering. Hence, spectral reflectivity has a broad bump in the range 10-100 keV with a maximum around 30-40 keV (Kontar et al., 2006). Backscattered photons make a significant contribution to the observed HXR spectral fluxes over the RHESSI energy range, and likewise, greatly effect the mean electron distribution spectrum. This downward backscatter of the primary emission can be significant in distorting or hiding the true features of the primary source spectrum. This is particularly relevant to the 17/09/02 and 12/04/02 events where there are bumps and dips in the mean electron

spectrum by counts to electrons lie in this critical energy range i.e. 30-40 keV. Kontar et al. (2006) for the first time use a Green's function approach to the backscatter deconvolution problem, constructing a Greens Matrix to include photoelectric absorption. To apply the albedo correction to this analysis we re-configure the DRM array using Green functions which can be enabled within the OSPEX software (optional before forward fitting of the fit functions). Kontar et al. (2006) showed that a clear low energy cutoff required to fit a photon flux model without albedo correction (forward fitting), essentially disappears, when the fit is to an albedo corrected photon flux model. The position of the flare, and its Heliocentric angle relative to the detectors from the solar surface, is important in this functional transform. Due to the significant low energy cutoff present in the solution for 17/09/02, and the dips and bumps featured at ~30 keV in this event, and at ~40 keV in 12/04/02, it is necessary to consider albedo contamination of the source function as a explanation for their existence. In figure 4.17 I present the albedo corrected regularized solutions of the mean electron distributions, minimized to a low energy cutoff electron model in 17/09/02 (*top*) and no low energy cutoff electron model in 12/04/02 (*bottom*). They are over-plotted onto the solutions found previously, which are without albedo correction, for comparative purposes. Clearly, the there is significant flattening of the low energy cutoff dip in the regularized solution for 17/09/02 with the albedo correction (black line) when comparing with no albedo correction (red line). This flattening is apparent in the forward fitted electron model also, when the correction is applied (yellow line). Considering 12/04/02, we see that the solution with albedo correction and no albedo correction is the same at thermal electron energies (<20 keV) as would be expected. However, there is a significant dip in the regularized solutions with albedo correction compared with no albedo correction for >20 keV until $\approx$ 140 keV, when the solutions meet again. The bumps and dips at ~40 keV also appear to have been smoothed to a certain extent as a result of the albedo correction on the regularized solution. This smoothing of the minor bumps in the 17/09/02 event at ~30 keV also occurs with albedo correction. Hence, contamination due to the albedo effect is potentially real in this regard, and such minor bumps and dips are physically impossible and represent instability in solution of these events.

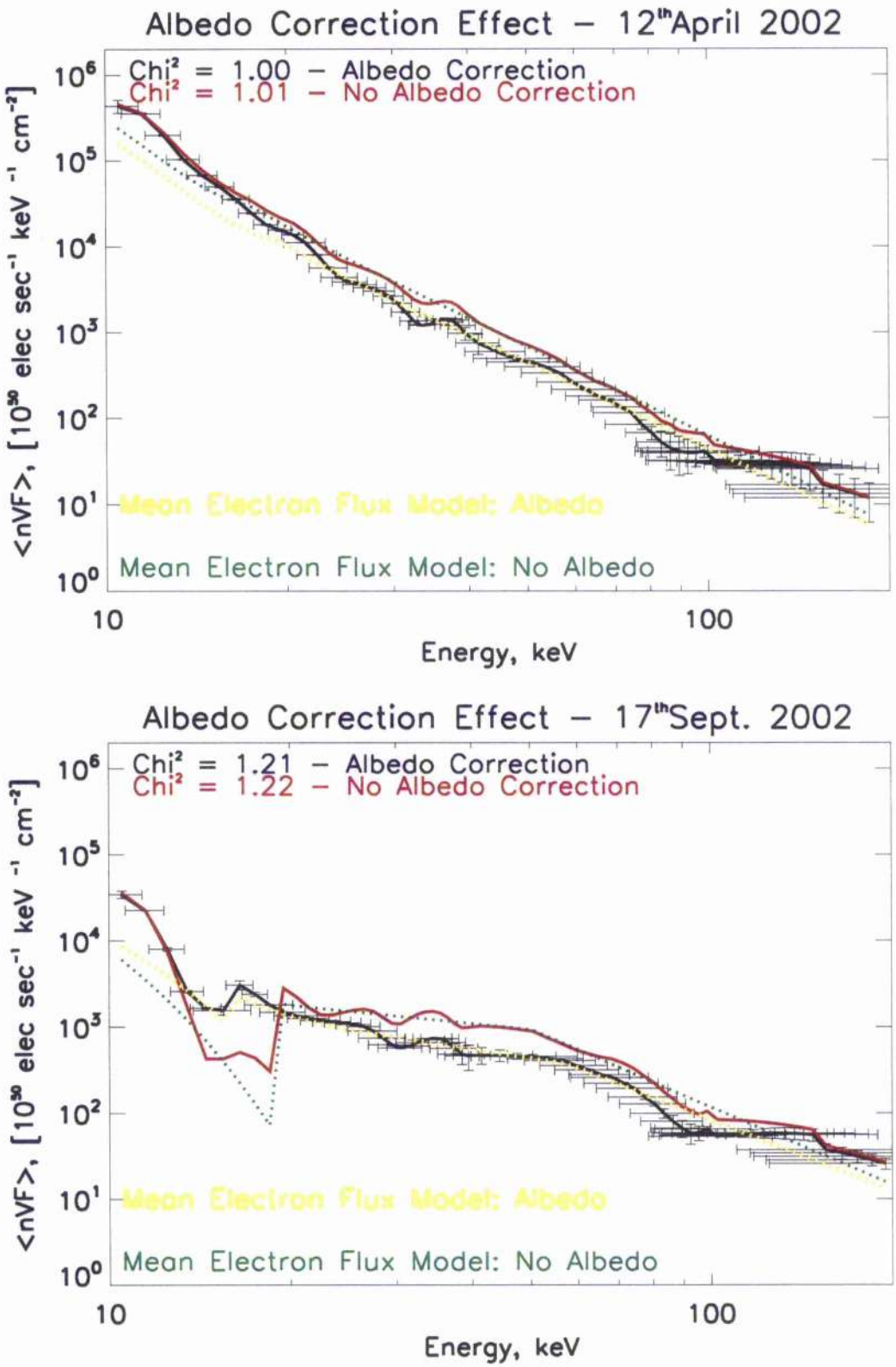

Figure 4.17: Comparing regularization solutions for mean electrons from count flux with and without albedo correction, for 17^{th} Sept.2002 (*bottom*) and 12^{th} April. 2002 (*top*).

Chapter 5

Conclusions

In this thesis I examined three HXR solar flare events observed by RHESSI, which occurred on 17^{th} Sept. 2002, 12^{th} April 2002 and 31^{st} Oct. 2003, respectively. Through such hard X-ray detection and spectrometry of flares we can interpret accelerated electron dynamics in the entire source source volume of the flare. The RHESSI detectors receive incoming photons from flares which are measured/recorded in count rate spectra. There are a number of methods which have been incorporated in this thesis for determining true photon flux spectra from counts, namely forward fitting, direct inversion and regularized inversion. Furthermore, we discussed how the cross-section for the interaction between the electron and proton (bremsstrahlung cross-section) allows us to relate the HXR photon flux to the electron flux using a linear integral relations (Brown, 1971), with respect to thin and thick target scenarios. It has been established that there are two steps to the problem of inferring electron distributions in the flares source volume, i.e. a counts to photons procedure followed by photons to mean electrons.

To determine the mean electron spectrum denoted as $(\bar{F}(E))$ for the selected events, we applied the forward fitting technique firstly, and then considered inversion approaches of the linear integrals. Through the forward fitting technique I used parametric electron flux models, provided by OSPEX, in each event with careful energy binning selection and background removal. The flares selected had characteristic attenuator states present during their

impulsive phase with unique DRM's. With a parametric form of $\bar{F}(E)$ the corresponding form of the HXR photon model is produced using the bremsstrahlung cross-section. Finally, through parameter adjustment and re-fitting the best form of $\bar{F}(E)$ is assumed (composed of adjustable thermal and thin-target bremsstrahlung components) with statistically acceptable fits, via χ^2 ($\approx$1) testing with normalized and cumulative residuals (within 2σ random walks in their noise distribution), of the model to the count flux data. The repercussion of this is unreliability in the returned photon flux spectra due to approximations as a result of using the conversion factors, for each event. The conversion factor for determining photons from counts in the photon energy range is fundamentally an approximation of the semi-calibrated DRM and is found to be severely reduced in the presence of thin, and moreso thick shutter, attenuators (see figure 2.6). Forward fitting presents a model dependent photon flux spectrum as opposed to a true interpretation of the photons. Despite this, the corresponding best fit electron distribution can still recover certain characteristic features such as the low energy cutoff. Yet, it has been shown that equally acceptable fits can be achieved with exclusion of the low energy cutoff, as was found for the 17^{th} Sept. 2002 and 31^{st} Oct. 2003 events (see fig. 2.14). This result made it challenging to distinguish which fit for the mean electron flux distribution is correct. The acceptability in the fits was also aided by the fact that the forward fit functions were limited to 9 free parameters. Such limitations due to forward fitting makes it virtually impossible to recover detail in the mean electron flux models. Next we considered direct inversion of the integral relation for count to photon conversions. Direct inversion in principle presents model independent calculations, rather than approximations of the HXR spectra from the count flux spectrum, which is a more ideal and logical approach to solving this problem.

Direct inversion proved to be ill-conditioned and highly problematic in recovering HXR spectra. The notable instability due to the non-diagonal DRM presents great error (noise) amplification and instability in the inverted truncated DRM, especially in 31^{st} Oct. 2003 flare with its thick shutter attenuator state. As well as this, truncation of the full DRM making it a square matrix, severely limits our analysis at the edges of photon energy inter-

vals. Our ability to correctly interpret the spectra is also greatly hindered with negativity (noise) in the photon flux at low photon energies in a thick shutter attenuator state. This negativity was evident also at very hard X-ray energies in 12/04/02. Hence, negativity in the HXR spectrum found by direct inversions appears to coincide with the presence of any attenuation. The attenuators substantially diminish the photon flux for lower energies so the HXR spectrum, especially in the 31^{st} Oct. 2003 event, is not well established at these energies (see fig. 3.3. The results for direct inversion agree with the literature (Craig & Brown, 1986) and are unacceptable when wanting to infer photons from counts. Such problems which create a lack of smoothness and reliability in the HXR spectrum have, to a large degree, been overcome with a regularized inversion approach.

To solve ill-posed inverse problems numerically one must introduce some additional information about the minimization solution, relating the discretized source function to the data function, such as an assumption on the smoothness. This is the method of regularized inversion. Generalized regularization has proved most effective in obtaining this information on both electron dynamics in the duration of the flare and analysis of hard X-ray spectra (Kontar et al., 2004,2005). By making a prior assumption of smoothness, to stabilize the solution, inversion of the data set spectrum with a generalized regularization algorithm, proposed by E.P.Kontar et al., 2004, which incorporates the Haug (1997) bremsstrahlung cross-section through generalized singular value decomposition of the kernel function. The decomposition creates singular vectors and eigenvalues, allowing us to form a generalized solution to the source functions. This technique can be used to infer more real features in the source spectra i.e. photon and mean electron flux spectra. This procedure assumes preconditions along with a photon flux model assumed by forward fitting, for each event. The negativity in the solution for photons found with direct inversion, along with noise amplification do not feature with generalized regularized inversion as seen in chapter 4. Instead with first order regularized, for identifying distinct local features in the spectra, we recovered a very smooth solution with very acceptable fits ($\chi^2 \approx 1$ in all events) to the photon flux model and reduced normalized and cumulative residuals, but with significantly more detail

in the solutions, compared with forward fitting results (see fig. 4.5). The accuracy in the regularized solution through analysis of error ratios matched those found with forward fitting justifying such a comparison to be made. In conclusion, the regularized solution presents the truest interpretation of the HXR spectrum. Calculation of the regularized errors through relating the discretized regularized solution and errors in the data function with a regularized operator $\mathbf{R}^{-1} \approx \mathbf{A}^{-1}$, has presented reduced errors and proved more effective than confidence interval estimation in the recovery of both photon and electron errors (see fig.4.7. Next, we considered the regularized photon solution structure without prior assumption of the photon model precondition. Convolution in the regularized solution when the spectral index of the power spectrum, representing the photon model for the minimization, does not match that of the true photon model, is evident through distortion in the solution away from the model at harder photon energies (see fig. 4.8). As we saw, the regularized solution function became increasingly distorted from the true solution, found with the true photon model. However, this problem becomes solvable when configuration of the DRM is controlled such that the truncation region elements of the array are reduced significantly. This is done through careful selection of the energy range of the observation with respect to the energy range of the fit. Following a very acceptable evaluation of the HXR spectrum we proceeded to recover the mean electron distribution from photons. The algorithm for solving photons from electrons required adaptation of the counts to electrons inversion software by replacing the counts and, errors in the counts, with photons and, errors in the photons. The solution for the mean electrons with the new approach to error analysis presented highly featured solutions in all events for both no and low energy cutoff scenarios. However, the problem of constructing mean electron distributions is greatly simplified with the introduction of a new approach, without losing any fidelity in the regularized solution. This approach combines both steps, from counts to photons then photons to electrons, into one step from counts to electrons through multiplication of the DRM array and bremsstrahlung cross section which presents a new kernel function in the single regularized inversion procedure. Hence, mean electrons can be successfully and accurately inferred without evaluation of the photon flux spectrum. As discussed this approach is more efficient, more attractive, and statistically

more desirable for recovering detail in the regularized solution.

Application of the inversion to both scenarios (mean electrons from photons and mean electrons from counts) not only provided a strong foundation for comparing between solutions in deducing physically real features but determining the best approach to constructing mean electron distributions. Indeed, the regularized solutions of all events potentially revealed many interesting bump and dip features, which appeared to show significant deviation from the forward fitted electron models. Examples of this are in the 25-40 keV range in 17^{th} Sept. 2002 event in fig. 4.16 with low energy cutoff in the electron model and likewise in the no low energy cutoff model minimization in fig. 4.15. Also in the energy range 30-45 keV there are obvious bump and dip features for the 12^{th} Sept. 2002 event as seen in fig. 4.15, which is also present in fig. 4.12 for the photons to mean electrons solution. Most notably, a low energy cutoff feature exists in 17^{th} Sept. 2002 and less so in the 31^{st} Oct. 2003 events, when the solution was fitted with a no low energy cutoff electron model. This is evident from figure 4.12 when inferring mean electrons from photons and is more prominent in figure 4.15 when inferring mean electrons from counts. The presence of such a feature in both evaluations of the mean electron distribution and in both scenarios with no and low energy cutoffs, all with very acceptable fits ($\chi^2 \approx 1$) and normalized and cumulative residuals, gives great confidence in the existence of such a physical feature for the 17^{th} Sept. 2002 event. The low energy cutoff in solutions with no low energy cutoff electron model conclusively shows evidence of model independence with regularized inversion, and in the limits of the errors. Consider the 12^{th} April 2002 event in fig. 4.12, of regularized mean electrons from photons with zero order regularization and also fig. 4.14 comparing first and second order regularization. Here we thought that we saw a significant high energy dip feature present in the energy range 100-150 keV. With higher order of regularization this feature became more distinct, however strongly compensated with increasing errors. The high energy cutoff should not be evident in the relatively low energy range of 100-150 keV, rather at greater than $\sim$300 keV. It can be concluded that this feature is most likely the result of incorrect background estimation through the OSPEX software, at the upper boundary of the fit en-

ergy range (~100 keV). The maximum electron flux occurs at 10 keV in both the models and regularized solutions and without any indication of a low energy cutoff for 12/04/02, as found with all approaches. This is an undeniable conclusion for 12/04/02. However the magnitude of the electron flux is 5×10^5 (elect. sec^{-1} cm^{-2} keV^{-1})in forward fitted model, whereas in the regularized solution for the mean electrons from both photons and counts the magnitude is $\approx 8\times10^5$(elect. sec^{-1} cm^{-2} keV^{-1}). This greater magnitude is conclusive for this event, since the fits for the regularized solutions are very acceptable with matching χ^2 values, and so generalized regularization can determine a more accurate total number of electrons present in the flare.

Careful consideration was also placed on the counts to electrons algorithm to allow for a fair comparison with the photons to electrons solution through applying systematic uncertainty on the count flux errors. The effect of this was a decrease in χ^2 which allowed for a greater smoothing parameter (reg_tweak). This means that when χ^2 for solutions in counts to electrons and photons to electrons are equal a fair comparison can be made since the degree of smoothing in the regularization is matched. For example, with the 17^{th} Sept. event the systematic uncertainty on the forward fit is 0.01%. Hence the error in the counts input into the counts to electrons inversion procedure, called from OSPEX, is increased by 0.01% of the count flux value for each energy bin. This increase in the errors reduces the χ^2 value of the fit of the solution to the electron model to which it has been minimized. Hence, for an acceptable fit with $\chi^2 \approx 1$, we have a relatively large reg_tweak value (3.1 in low energy cutoff model fit; 4.1 in the no low energy cutoff model fit) compared with the reg_tweak value for an acceptable fit ($\chi^2 \approx 1$) to the regularized mean electrons from photons (1.8 in low energy cutoff model fit; 1.12 in the no low energy cutoff model fit). It is important that the χ^2 values are comparable and acceptable, so that the regularized solutions are comparable as is the case for all the results respective of each event. Otherwise physical features which exist in the mean electron distributions cannot be verified.

To clarify the existence of the bumps and dips in the 17/09/02 and 12/04/02 events I

introduced the albedo correction into the DRM configuration using Green functions. The dips and bumps found in the regularized solution for mean electrons from counts, in the energy range from $\sim$ 30 - 50 keV of both 17/09/02 and 12/04/02, cannot be physically real since they would be too unstable. The results for the albedo corrected mean electron distribution solutions for 17/09/02 and 12/04/02, compared with the solution with no albedo correction, are shown in figure 4.17. The result is conclusive since the bump and dips are smoother in the 30-40 keV energy range for 12/04/02 with albedo correction. The overall effect of the albedo is clear in the critical energy range (10-100 keV) when the backscatter is removed, for the solution of this event. The albedo effect is equally apparent in the 17/09/02 event with considerable smoothing of the low energy cutoff. Likewise, the bump and dips at $\sim$30 keV are smoother with albedo correction. Hence, these minor bump and dip features are most likely the result of inverting photon data uncorrected for albedo, which results in contamination of the source spectrum.

In summary, the results for regularized inversion from counts to electrons, as presented in the inversion software, showed a distinct improvement upon the original solution for mean electrons found from photons. The fundamental point here is that the solution found from photons is over-smoothed, hence certain bump and dip features in the electron energy range along with the more important global features such as low energy cutoffs, are less distinct. The solution in the no low energy cutoff electron model regularization for 17^{th} Sept. 2002 event in fig 4.15 shows an obvious low energy cutoff with a flux magnitude ($\sim$100 elect. sec^{-1} cm^{-2} keV^{-1}) at the cutoff energy ($\sim$18 keV) comparable with the low energy cutoff model from the forward fit, whereas the flux magnitude in the solution with no low energy cutoff from photons was not so great: a further indication of a more smoothed solution of mean electrons from photons. The 31^{st} Oct. 2003 event however, showed a very smoothed solution in counts to electrons, i.e. featureless, and with large errors in solution. This is comparable with what was found with photons to electrons, and again with no significant low energy cutoff feature in the no low energy cutoff model minimization. This result is most likely due to the severe instability of the solution due to the thick shutter attenuators. This impact may be evident in the low energy cutoff scenario for this event in the energy range 10-30

keV, where the vertical errors are particularly large (see fig. 4.16). All fits proved acceptable ($\chi^2 \approx 1$) with respect to their normalized and cumulative residuals and the Picard condition was satisfied, hence allowing fair and reliable comparisons to be made.

As a final conclusion, generalized regularization has proved most worthy as a model independent alternative to forward fitting, complimented by stability and effective suppression of noise induced un-physical behaviour. Unlike the direct inversion approach which provided very unstable solutions with noise amplification, particularly in A3 state events. The regularized inversion algorithm presents many distinct features in the solution for the mean electron distribution which forward fitting had failed to show, and in some cases misled us. For example, I presented acceptable mean electron distributions with both no or low energy cutoffs in both the 17^{th} Sept. 2002 and 31^{st} Oct. 2003 events. The low energy cutoff feature, strongly evident in the regularized solution for 17^{th} Sept. 2002 event with minimization to a no low energy cutoff model, must indicate an energy characterizing the physics of the acceleration process (i.e. presence of a lower limit to the accelerated electron spectrum) or electron energy losses. The shallowing of the slopes in the solution of $\bar{F}(E)$ for all events via counts to electrons, between 10-30 keV, is due to the presence of thermal plasma from a source with a broad temperature distribution (Brown, 1974 and Brown & Emslie, 1988). If the acceleration were purely stochastic in character we would expect a pure power law acceleration spectrum in the mean electron distributions, which is not the case in any of the events analyzed. We have shown that a simpler and faster approach to inferring the mean electron distributions directly from count flux space is more effective than a counts to photons to electrons approach in revealing a truer nature of source spectrum. This new approach presents a more accurate diagnostic for the acceleration and propagation of high energy electrons and their energy budget.

5.0.1 Future Work

In the future, I intend to investigate many more large flare events, in the presence of each of the attenuator states, to further analyze the effect of the attenuators on the DRM con-

figuration and its impact within count to electron regularized inversions. One such event I will consider is the 23^{rd} of July 2002 event which was closely analyzed by Piana et al., 2003 and Kontar et al., 2005, but without application of a counts to electrons regularized inversion. It would be interesting to see if the features they found (dip at $\sim$ 55 keV) are evident, or more prominent, in a counts to electrons solution, and if there are any other features to be recovered. I would be interested in considering the spectral indices of the regularized solutions by counts to electrons inversion for the events investigated in this thesis. It may be possible to use the spectral indices of the mean electron distribution function to discover possible inconsistencies with the thick target model, which has a condition whereby the spectral index at any mean electron energy cannot be less than -1. In evaluating the count flux data we must use the RHESSI software to determine the correct energy binning, time resolution, and correct background spectrum. When the flare is short ($\sim$ tens of minutes), this can be done relatively easily by selecting data intervals before and after the flare event. For long lasting flares, this can be inaccurate however as the background can vary significantly over tens of minutes making it difficult to accurately determine the correct count flux spectrum. This becomes important at higher energies where flare count rates are close to non-flare rates, and may have resulted in the unphysical dip in the mean electron distribution for the 12^{th} April 2002 event, by photon to mean electron regularized inversion. Working to improve the accuracy in the background spectrum could remove such unwanted noise amplifications. Also obtaining spectra of high accuracy also depends on knowledge of several other instrument-related factors, e.g. pulse pileup (Smith et al., 2002). I intend to examine such problems in future analysis of RHESSI spectra.

References

Alexander, R.C., & Brown, J.C.: 2002, Ed. A. Wilson., Noordwijk: ESA Publications Division, v. 1, p. 271.

Arnoldy, R. L., Kane, S. R., Winckler, J. R.: 1967, Solar Physics, v. **2**, p. 171.

Benz, A.O.: 1993, Astrophysics and Space Science Library, , Dordrecht: Kluwer, v. **184**.

Bertero, M., Boccacci, P.: 2000, Astronomy and Astrophysics Supplement, v. **147**, p. 323.

Bertero, M., De Mol, C., & Pike, E.R.: 1985, Inverse Problems, v. **1**, p. 301.

Bertero, M., De Mol, C., & Pike, E.R.: 1988, Inverse Problems, v. **4**, p. 573.

Brown, J.C.: 1971, Solar Physics, v. **18**, p. 489.

Brown, J.C.: 1973, Solar Physics, v. **31**, p. 143.

Brown, J.C.: 1974, Edited by Gordon Allen Newkirk. I.A.U. Symp. no. 57, Dordrecht; Boston: Reidel, p. 395.

Brown, J.C., Spicer, D.S., Melrose, D.B.: 1979, Astrophysical Journal, v. **228**, p. 592.

Brown, J.C., and Emslie, A.C.: 1988, The Astrophysical Journal, v. **331**

Brown, J.C.,*et al.*:2003, The Astrophysical Journal, v. **595**, p. L115

Brown, J.C.: 2005, Astronomy and Astrophysics Space Science Library, v. **320**, p. 87.

Brown, J.C.,*et al.*: 2006, The Astrophysical Journal, v. **643**, p. 523.

Carmichael, M.: 1964, NASA, Science and Technical Information Division, p. **451**.

Craig, I.J.D., & Brown, J.C.: 1986, Inverse Problems in Astrophysics, Bristol, England and Boston, MA, Adam Hilger, Ltd.

de Jager, C.: 1963, Bulletin of Astronomical Institutes of the Netherlands, v. **17**, p. 209.

Dennis, B.R., *et al.*: 2004, 35th COSPAR Scientific Assembly, Paris, France., p. 1284

Wentzel,D.G.: 1989, 'The Restless Sun', Smithsonian Library of the Solar System.

Elwert, G.: 1939, Ann. Physik, v. **34**, p. 178.

Emslie, A.G., *et al.*: 2003, The Astrophysical Journal, v. **595**, p. L107.

Groetsch, C.W.: 1984, The Theory of Tikhonov Regularization for Fredholm Equations of the First Kind (Pitman:Boston).

Hansen, P.C.: 1992, Inverse Problems, v. **8**, p. 849.

Haug, E.: 1997, Astronomy and Astrophysics, v. **326**, p. 417.

Heitler, W.: 1954, International Series of Monographs on Physics, Oxford, 3rd ed.

Holman, G.D., *et al.*: 2003, The Astrophysical Journal, v. **595**, p. L97.

Hirayama, T.: 1974, Solar Physics, v. **34**, p. 323.

Hudson, H.S.: 1972, Solar Physics, v. **24**, p. 414.

Jackson, J.D.: 1962, Classical Electrodynamics, New York; Wiley.

Johns, C., and Lin, R.P.: 1992, Solar Physics, v. **137**, p. 121.

Koch, H.W., and Motz, J.W.: 1959, Physics Review, v. **31**, p. 920.

Kontar, E.P., *et al.*: 2003, The Astrophysical Journal, v. **595**, p. L123.

Kontar, E.P., *et al.*: 2004, Solar Physics, v. **225**, p. 293.

Kontar, E.P., *et al.*: 2005, Solar Physics, v. **226**, p. 317.

Kontar, E.P., *et al.*: 2005, Solar Physics, v. **227**, p. 299.

Kontar, E.P., *et al.*: 2006, Astronomy and Astrophysics, v. **446**, p. 1157.

Korchak, A.A.: 1967, Soviet Astronomy, v. 11, p. 258.

Korchak, A.A.: 1971; Solar Physics, v. **18**, p. 284.

Kopp, R.A., & Pneuman,G.R.: 1976, Solar Physics, v. **50**, p. 85.

Kundu, M.R.: 1963, Space Science Reviews, v. **2**, p. 438.

Lin, R.P., & Hudson, H.S.: 1971, Solar Physics, v. **17**, p. 412.

Lin, R.P., & Hudson, H.S.: 1976, Solar Physics, v. **50**, p. 153.

Lin, R.P., *et al.*: 2002, Solar Physics, v. **210**, p. 3.

Prato,M., *et al.*: 2006, Solar Physics, v. **237**, p. 61.

Massone,A.M., *et al.*: 2003, Astronomy and Astrophysics, v. **405**, p. 325.

Masuda, S., *et al.*: 1995, Publication Astronomy Society Japan, v. **47**, p. 677.

Morozov, V.A.: 1966, Soviet Math. Dokl., v. **7**, p. 414.

McKenzie, D.E.: 2002, Elsevier Science on behalf of COSPAR in COSPAR Colloquia Series, p. 155.

Ogawara, Y., *et al.*: 1991, Solar Physics, v. **136**, p. 1.

Peterson, L.E., & Winckler, J.R.: 1959, Journal of Geophysical Research, v. **64**, p. 697.

Philips, K.J.H., *et al.*: 2006, The Astrophysical Journal, v. **638**, p. 1154.

Phillips, K.J.H., Chifor, C., Dennis, B.R.: 2006, The Astrophysical Journal, v. **647**, p. 1480.

Piana, M., *et al.*: 1994, Astronomy and Astrophysics, v. **288**, p. 949.

Piana, M., & Brown,J.C.: 1998, Astronomy and Astrophysics, v. **132**, p. 291.

Piana, M., *et al.*: 2003, The Astrophysical Journal, v. **595**, p. L127.

Priest, E.R., Forbes,T.G.: 2002, Astronomy and Astrophysics Review, v. **10**, p. 313.

Share, G.H., *et al.*: 2003, The Astrophysical Journal, v. **595**, p. L89.

Shibata, K., *et al.*: 1995, Astrophysical Journal Letters v. **451**, p. L83.

Shimojo, M., & Shibata,K.: 2000, Advances in Space Research, v. **26**, p. 449.

Smith, D.M., *et al.*: 2002, Solar Physics, v. **210**, p. 33.

Smith, D.M., *et al.*: 2003, The Astrophysical Journal, v. **595**, p. L81.

Somov, B.V.: 1992,"Physical Processes in Solar Flares",Space Library, v. **172**.

Tanaka, Y.: 1987, Dordrecht, D. Reidel Publishing Co., v. **172**, p. 171.

Tandberg-Hanssen, E., & Emslie, A.G.: 1988, 'The Physics of Solar Flares',Cambridge University Press, v. **286**, p.

Tikhonov, A.N.: 1963, Soviet Math. Dokl., v. **4**, p. 1035.

Tikhonov, A.N., *et al.*: 1995, Numerical methods for the solution of ill-posed problems, Kluwer; Dordrecht.

Thompson, A.M., *et al.*: 1992, Astronomy and Astrophysics, v. **265**, p. 278.

Tsuneta, S., *et al.*: 1992, Astronomical Society of Japan, v. **44**, p. L63.

van Loan, C.F.: 1976, SIAM J., Num. Anal., v. **76**, p. 13.

Zirin, H.: 1988, Book-Review - 'Astrophysics of the Sun Science', v. **242**, p. 1586.